Quaternary Evolution of the Upper Equatorial Indian Ocean: Insights from the Paleothermocline Reconstructions using Planktonic Foraminiferal Mg/Ca and Isotopic Records

A thesis submitted in partial fulfilment of
the requirements for the degree of

Doctor of Philosophy

by

Sanjit Kumar Jena

(Roll No. 18330020)

With the guidance of

Prof. Ravi Bhushan

Geosciences Division

Physical Research Laboratory, Ahmedabad, India

Discipline of Earth Science

Indian Institute of Technology Gandhinagar, India

2023

Dedicated To
The
Eternal Mother

DECLARATION

I declare here that this thesis report represents my own ideas in my own words and I have included others' ideas with appropriate citations from original sources. I also declare that I have followed all principles of academic honesty and integrity and have not misrepresented or fabricated or falsified any idea/fact/source/data in my submission. I understand that any violation of the above can cause disciplinary action by the Institute and can also evoke penal action from the sources which have thus not been properly cited or from whom proper permission has not been taken when needed.

Date:

Signature: Sanjit Kumar Jena
(Roll No.: 18330020)

Department of Earth Science

Indian Institute of Technology, Gandhinagar

Gujarat-382355

CERTIFICATE

It is certified that the work contained in the thesis titled **"Quaternary Evolution of the Upper Equatorial Indian Ocean: Insights from the Paleothermocline Reconstructions using Planktonic Foraminiferal Mg/Ca and Isotopic Records"** by **Mr. Sanjit Kumar Jena** (Roll no: 18330020) has been carried out under my supervision and that this work has not been submitted elsewhere for a degree. In my opinion the work is fully adequate in scope and quality for the degree of Doctor of Philosophy.

Prof. Ravi Bhushan

(Thesis Supervisor) Professor,

Geosciences Division,

Physical Research Laboratory,

Ahmedabad, India Date:

ACKNOWLEDGEMENTS

The five-year doctoral journey at PRL has been a period of tremendous learning and incredible experiences. As I approach towards the successful completion of this remarkable phase of life, I express my utmost gratitude to each and every individual who has left a lasting impact through all their invaluable contributions in turning the challenging paths into a success.

First and foremost, I express my deepest gratitude and heartfelt regards to my esteemed mentor Prof. Ravi Bhushan for his unwavering faith and support. His profound generosity and positive outlooks have played a pivotal role in fostering optimism during the challenging times. His freedom and nurtured support have always provided the essential ambience to flourish the innermost potentials and aspire for the larger goals.

I express earnest reverence to all my DSC members, Prof. S. Ramachandran, Dr. A. K. Sudheer and Dr. Vineet Goswami for their valued experiences and shared scientific insights. Prof. Ramachandran has been instrumental as a sincere advisor and critical evaluator, constantly helping elevate the quality of my research work. Dr. Sudheer has provided a principal support in instrumentation and essential scientific feedbacks. I am extremely thankful to Dr. Vineet Goswami for his constant motivation and friendly support towards the technical and scientific advancement my doctoral research.

I acknowledge the significant contributions of the academic committee members and the Geosciences faculties for their critical examinations and scientific evaluations during the academic reviews and the division seminars. I express my sincere gratitude to Prof. R. D. Deshpande, Dr. Neeraj Rastogi, Dr. Sanjeev Kumar, Prof. M. G. Yadava and Dr. Anil D. Shukla for their profound insights and scientific supports. I am indebted to the senior elites, Prof. J. S. Roy and Prof. M. M. Sarin for their prolific suggestions and priceless inputs. Special thanks to the Director, PRL and IIT, Gandhinagar, for their salient contributions in improving the quality of the academics and allied facilities.

I am greatly indebted to my senior lab mates for their extensive support and care throughout the journey of my doctoral research. Working with a cordial and experienced lab has always been an outstanding privilege. I am extremely thankful to two of my senior colleagues, Nisha

Didi and Partha for their constant help and persistent guidance. I am truly thankful to Ankur Bhai and Shivam for their expert assistance in learning the criticalities of AMS. I am also thankful to all our veteran lab mates Upasana Didi, Chandana Didi, Harsh Bhai, Murugan Bhai, Romi and Chinmay Bhai for their helping hands and supportive concerns towards the successful progress of my PhD research.

I express heartfelt thanks to all my batchmates and PRL colleagues for their active support and friendly endeavours. Special mentions to the geosciences colleagues, Siddhartha and Deva, and friends Yash, Namita, Arijit, Monika, Yogesh, Dayanand, Binal, Vikash, Akanksha, Naval, Pranav, Supriya, Sunil, Deepak, Meghna, Anupam, Sandeep, Deepak and Anju, and others for the cheerful memories and friendly vibes. I am also thankful to Swagatika, Anil Bhai, Abhay Bhai, Ankit Bhai, Alka Didi, Neeraj Didi, Satyajeet Bhai, Ashish, Atif Bhai, Milan Bhai, Deepika Didi and Amit Pandey for the helping and cordial times.

It has been a great privileged to share some outfield memories in the PRL sports activities in cricket and football thanks to Manan Bhai, Bhala Sir, Piyush, Ram Lakhan, Ranjan, Rohit, Akash, Deepak, Dipendra and all other active members. I also express my gratefulness to Sachi Sir, Nistha Ma'am and Bhushit Sir for their timely supports and necessary helps.

I truly acknowledge the management support provided by Jaldhi, and the contributions of all the PRL staffs in library, computer centre, administration, account section, workshop, CMG, purchase and store section towards running and maintaining a constantly healthy research environment.

Special thanks to the non-PRL colleagues and academicians including Prof. Kaustubh Thirumalai, Dr. Mahesh, Prof. Luke Skinner, Prof. Claire Waelbroeck, and Prof. Thomas Marchitto, and my fellow colleagues Tejeswar and Nirmalya for their additional supports and essential scientific inputs. My obligations to Dr. Prashanta Sanyal, Santrupta Samantaray and fellow lab members at IISER, Kolkata for their outstanding cooperation and assistance in stable isotopic analyses using KIEL Carbonate Device.

Lastly, I take this unique opportunity to express the highest gratitude towards my grandparents and my family for their unparalleled support and utmost sacrifices towards raising me with integral values and priceless commitments. I am truly obliged to the supreme lord and the eternal mother for nurturing me with the ultimate purpose of life.

ABSTRACT

The Equatorial Indian Ocean (EIO) thermocline plays a significant role in modulating the regional and global climate dynamics providing strong feedback mechanisms to the atmospheric overturning circulations and the atmospheric hydrologic cycles through changes in its mean thermal state. However, substantial gap exists in the understanding of the millennial scale evolution of the EIO paleothermocline and its global paleoclimatic interlinkage due to the lack of adequate paleothermocline reconstruction studies. High resolution studies are subjected to the major challenges associated with extremely low sedimentation rates, limited sample availabilities, and the intrinsic technicalities in the geochemical processing and analytical methodologies. Planktonic foraminifers are a group of calcareous micro-organisms that survive under specific oceanic depths extending from the surface to the deep oceanic region. The fossil foraminifers help provide critical clues about the past water mass conditions through the major proxy recorders incorporated into their shells during the timing of calcifications. However, finding an abundant number of individual planktonic foraminifer species is always a challenge for paleo reconstruction studies, specifically for a low-productive EIO region. A limited number of efforts that have been carried out so far from the eastern and the western Indian Ocean boundaries have used a single planktonic foraminiferal representative for the paleo-thermocline reconstruction, which significantly underestimates the paleoclimatic significances of the intra-thermocline variabilities.

The present study is a maiden attempt from the Indian Ocean (IO) to obtain a quantitative reconstruction of a complete thermocline profile from the upper EIO using depth-specific planktonic foraminifers from the surface and the intra-thermocline oceanic depths, using a sediment core SK-312/12 situated over the western central EIO at 0°N, 65°E. Three major proxies have been investigated, which include the Mg/Ca, the radiocarbon and the stable oxygen isotopic records of the planktonic foraminifers. The chronology of the sediment core obtained from the radiocarbon dating extends up to last 44 ka.

The results obtained from the study show evidence of a hydrothermally influenced extremely depleted radiocarbon interval from the thermocline during 25-34 ka, which has been named

as the MIS3-MIS2 transition ‘Mystery Interval’. The deglacial thermocline radiocarbon depletions are primarily attributed to the aged supersaturated deep oceanic southern source ventilation through the Sub-Antarctic Mode Water-Antarctic Intermediate Water (SAMW-AAIW). High-latitude climatic tele-connections are evident from the paleotemperature reconstruction records from the SK-312/12 thermocline along with the increased influence of Indonesian Through Flow (ITF) into the lower thermocline during the Holocene. Paleosalinity records indicate a strong control of enhanced equatorial precipitation over the surface salinity during the colder climatic periods. The Arabian Sea High Salinity Water (ASHSW) influx has varied over millennial warm-cold periods with enhanced equatorial spread during the cold climates through reduced south-west monsoonal precipitation and increased surface oceanic salinity over the northern Arabian Sea. The surface salinity variations during the Holocene indicate a strong inter-basinal Indo-Pacific climatic connection through IOD and ENSO variabilities.

To summarise, the present study is a unique attempt to carry out a quantitative reconstruction of the EIO paleothermocline using three major planktonic foraminiferal proxy records. The scientific outcomes obtained from this study provide critical information to the understandings and development of the EIO paleothermocline and its significant implications towards the regional and global paleoclimatologies during the millennial scale time periods.

CONTENTS

List of Figures

List of Tables

Abbreviations

AAIW	Antarctic Intermediate Water
ACD	Apparent Calcification Depth
ACR	Antarctic Cold Reversal
AGE	Automated Graphitization Equipment
AML	Average Mixed Layer
AMOC	Atlantic Meridional Overturning Circulation
AMS	Accelerator Mass Spectrometer
AS	Arabian Sea
ASHSW	Arabian Sea High Salinity Water
AURiS	Accelerator Unit for Radioisotope Studies
BA	Bølling Allerød
BI	Bouncer-Injector
BoB	Bay of Bengal
CCD	Calcite Compensation Depth
CEC	Cross Equatorial Cell
CHS	Carbonate Handling System
CID	Charge Injection Device
CIME	Carbon Isotope Minimum Event
cIO	central Indian Ocean
CIR	Central Indian Ridge
CLR	Chagos-Laccadive Ridge
CR	Carlsberg Ridge
D/O	Dansgaard-Oeschger
DCM	Dissolved Chlorophyll Maximum
DIC	Dissolved Inorganic Carbon
EA	Elemental Analyser
EACC	East African Coastal Current
EEIO	Eastern Equatorial Indian Ocean
EEP	Eastern Equatorial Pacific
eIO	eastern Indian Ocean

EIO	Equatorial Indian Ocean
EIR	East Indian Ridge
ENSO	El-Nino Southern Oscillation
E-P	Evaporation-Precipitation
ESA	Electrostatic Analyser
FIRI	Fourth International Radiocarbon Intercomparison
GIC	Gas Ionisation Chamber
GIV	Global Ice Volume
H	Heinrich
H1	Heinrich Stadial 1
H2	Heinrich Stadial 2
H3	Heinrich Stadial 3
HE	High Energy
HVEE	High Voltage Engineering Europa
IAEA	International Atomic Energy Agency
ICP-OES	Inductively Coupled Plasma Optical Emission Spectrometer
IO	Indian Ocean
IOD	Indian Ocean Dipole
IRMS	Isotope Ratio Mass Spectrometer
ITCZ	Inter-Tropical Convergence Zone
ITF	Indonesian Through Flow
ka	kilo annum
kyr	kilo years
LE	Low Energy
LGM	Last Glacial Maximum
lThm	lower Thermocline
MIS	Marine Isotopic Stages
ML	Mixed Layer
MLD	Mixed Layer Depth
MOR	Mid Oceanic Ridge
MQ	Milli-Q
NADW	North Atlantic Deep Water

NBS	National Beauro of Standards
NEM	North-East Monsoon
OX	Oxalic acid standard
PDB	Pee Dee Belemnite
PRL	Physical Research Laboratory
PSU	Practical Salinity Unit
PVC	Poly Vinyl Chloride
R	Global mean reservoir age
RF	Radio Frequency
RI	Rare Isotope
RSPGIW	Red Sea Persian Gulf Intermediate Water
RSW	Red Sea Water
RTJ	Rodriguez Triple Junction
SAMW	Sub-Antarctic Mode Water
SC	Somali Current
SEC	South Equatorial Current
SEIR	South East Indian Ridge
sIO	southern Indian Ocean
SST	Sea Surface Temperature
S_{SW}	Sea water salinity
STF	Sub Tropical Front
SWIR	South West Indian Ridge
SWM	South-West Monsoon
T	Temperature
TE	Trace Elemental
THC	Thermohaline Circulation
TSI	Total Solar Insolation
uThm	upper Thermocline
VPDB	Vienna Pee Dee Belemnite
VSMOW	Vienna Standard Mean Ocean Water
WEIO	Western Equatorial Indian Ocean
wIO	western Indian Ocean
WJ	Wyrtki Jet

WOA	World Ocean Atlas
WOCE	World Ocean Circulation Experiment
YD	Younger Dryas
$\Delta^{14}C$	Radiocarbon
$\delta^{18}O$	Oxygen isotopic ratio

Chapter 1

Introduction

1.1 Introduction

The oceans comprise around 71% of the earth's total surface containing a gigantic volume of nearly 1.37 billion km^3 (American Meteorological Society., 2018) of water distributed through five major oceanic reservoirs i.e. the Pacific, the Atlantic, the Indian, the Arctic and the Southern Ocean. The Pacific, the Atlantic and the Indian Ocean constitute the tropical to sub-tropical oceans, whereas the Arctic and the southern ocean encompass the polar to sub-polar latitudes in the northern and the southern hemispheres respectively. The oceans undergo various temporal and spatial scale circulations in the form of surface currents, oceanic gyres, diffusive and advective transfers and the deep-oceanic thermohaline circulations. They impart significant contributions to the global climatic variability through constant atmospheric interaction and climatic feedback mechanism.

The incoming solar radiation provides the primary source of physical, chemical and biological processes operating over the earth. The ocean has immense control on the planetary heat and energy distribution through its extensive global surface cover and latent heat capacity. On an annual global average, the ocean transfers nearly around ten times higher heat into the atmosphere. Out of the total incoming solar radiation into the earth's atmosphere, around 7% is lost through scattering into the space, 23% is absorbed by the atmosphere and 23% is reflected by the clouds and the earth's continental surfaces and glaciers. Out of which, around ~20% is received by the land and a large fraction of ~80% is received by the global ocean (American Meteorological Society., 2018) (Fig. 1).

1.2 The Indian Ocean

The Indian Ocean has a unique hydrography compared to its tropical counterparts of the Pacific and the Atlantic, associated with the northward closure provided by the presence of the Indian subcontinent. The limits of northward tropical extension of the Indian Ocean results in the absence of a distinct northern sub-tropical gyre through pre-domination of regional and local water mass circulations. The geographical distribution of the Indian subcontinent adds to the characteristic development of world's strongest seasonal wind reversal called the Indian Monsoon System (Schott et al., 2009). The Indian Ocean remained the least known to the global oceanographic community until its first extensive exploration carried out during the International Indian Ocean Expedition between 1962 to 1965 (Wyrtki, 1971). Further explorations were carried out between

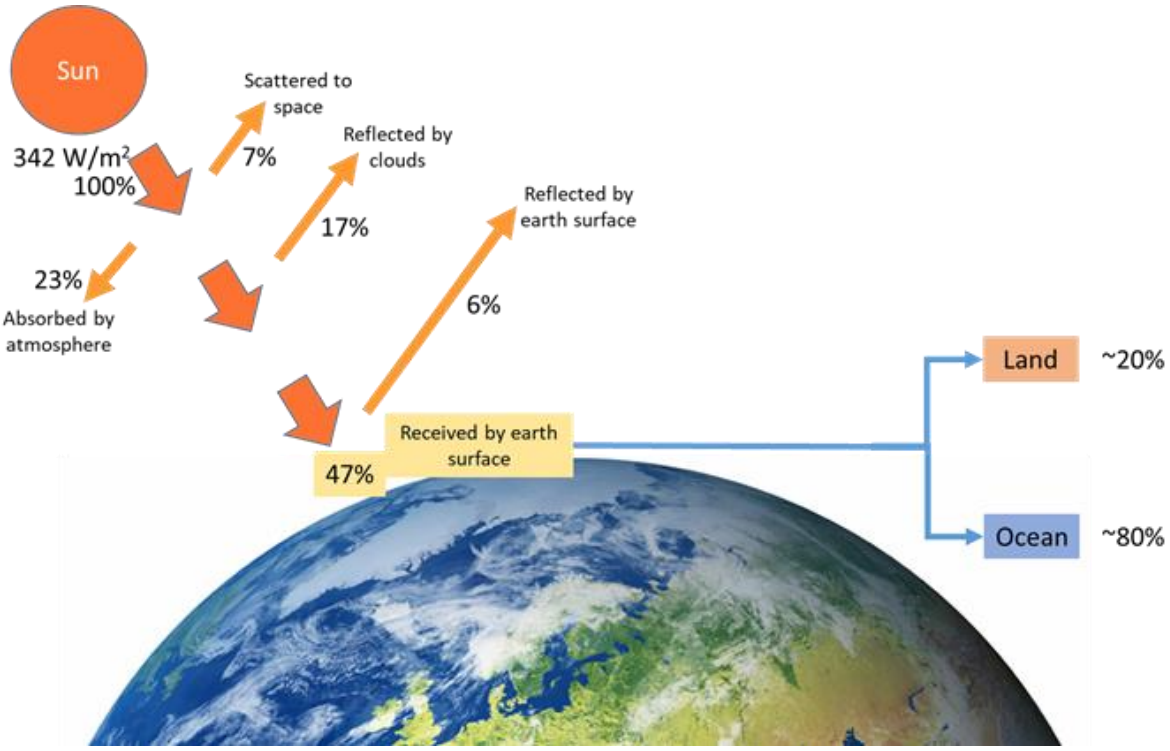

Source (Image of Earth): CodeAcademy. Data source: (American Meteorological Society., 2018).

Figure 1.1: Variability in average solar radiation reaching the earth's surface.

the 1980s and 1990s as a part of the World Ocean Circulation Experiment (WOCE) that added further information regarding the sub basinal variabilities of the Arabian Sea, the Red Sea, the Indonesian Throughflow, the Leeuwin Current, and the Agulhas Current/Retroflection (Weiss, 1983); Wyrtki, 1973). With increase in the availability of information, the primary significance of the Indian Ocean and its essential contributions to the global scale oceanic and climatic evolutions were soon realized by the global scientific communities.

The Indian Ocean (IO) comprises a number of sub-basins, the Bay of Bengal (BoB) in the eastern part and the Arabian Sea (AS) in the western part of the northern IO. The tropical IO basin constitutes the central Indian Ocean (cIO), the eastern Indian Ocean (eIO) and the western Indian Ocean (wIO). The Southern Indian Ocean (sIO) extends to the northern margins of the Southern Ocean up to 40-50°S Sub Tropical Front (STF). The IO observes inter-basinal connections with the Pacific through the Indonesian archipelago and a low-latitudinal connection with the Atlantic through the Agulhas current (Talley, 2013). The Antarctic Intermediate Waters produced at the southern sub-polar to sub-tropical fronts intrude into the Indian Ocean intermediate waters through the process of ocean-tunnelling (Liu and Yang, 2003). The high density Red Sea Water and the

Persian Gulf Water contribute to the thermocline and Intermediate depths of the Arabian Sea with extensions up to the Equatorial Indian Ocean (EIO). The BoB receives substantial fresh water influx from the Himalayan rivers draining into the eastern coast of the Indian subcontinent.

1.3 The Upper Equatorial Indian Ocean

The Equatorial Indian Ocean (EIO) is the second largest tropical oceanic belt in the world next to the tropical Pacific (Thandlam et al., 2020b). It extends from 40°E to 100°E longitudes and 10°S to 10°N latitudes across the equator. The EIO acts as a common bridge in exchanging water masses between the southern and the northern parts of the Indian Ocean (IO) basin including the southern sub-tropical gyre, the Arabian Sea (AS) and the Bay of Bengal (BoB), thus providing strong contribution to the regional hydrologic and oceanographic variabilities. It is also significantly associated with the inter-basinal and inter-hemispheric climatic transactions through the surface and subsurface ocean-atmospheric processes (Thandlam et al., 2020a).

The upper EIO refers to the combined section of the upper oceanic water column that includes the surface mixed layer (ML) and the subsurface thermocline region. This characteristic water mass region shows exclusive implication towards the regional and global climatic variabilities by providing primary control into the atmospheric and hydrologic cycles through coupled upper ocean-atmospheric feedback mechanisms and changes in the mean thermal gradients across it (Held and Soden, 2006; Saji and Yamagata, 2003; Vecchi and Soden, 2007). The average depth of the upper EIO ranges up to ~150m (Stainbank et al., 2019; Yadav et al., 2021). Variations in the upper EIO hydrology can be caused by the different surface and subsurface ocean-atmospheric processes operating over the EIO, brief descriptions of which have been provided below.

1.3.1 Ocean-Atmospheric Processes

Indian Monsoon System: Monsoon is the seasonal reversal of winds that carry strong lower atmospheric winds towards the low pressure Inter-Tropical Convergence Zone (ITCZ) which results in abundant rainfall by the rising arm of the Hadley cell through condensation of the wind driven moistures collected en-route. The Indian Monsoon System driven by the Asian continents forms the strongest monsoon system on Earth (Schott et al., 2009). During boreal summer, the south-west monsoonal winds flow towards north-east due to the northward shifting of ITCZ over the Indian subcontinent, resulting in high monsoonal precipitations over the Indian subcontinent and the Bay of Bengal (BOB). The north-east monsoon flows to the south-west during the boreal

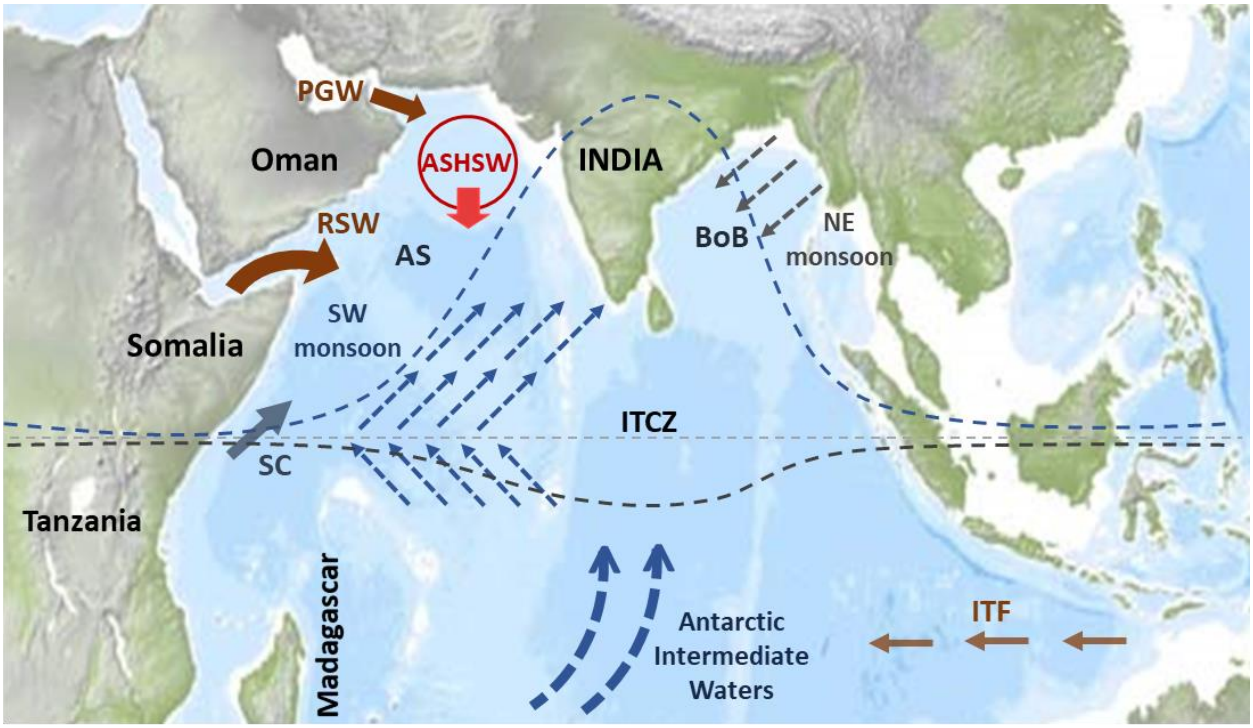

Figure 1.2: Schematic of major surface and sub-surface processes operating over the Equatorial Indian Ocean.

winter due to southward shifting of the low pressure ITCZ, resulting in precipitation over the BoB and the southern ends of the Indian sub-continent (Wang, 2006). During the summer monsoon, the South Equatorial Current (SEC) and East African Coastal Current (EACC) carry the surface waters from the south to supply the northward Somali Current (SC). Upwelling takes place at the Somali region due to wind-driven coastal upwelling adding cold subsurface waters to the surface current. A part of the Somali Current turns offshore and recirculates across the equator as the ‘‘Southern Gyre”. During the north-east monsoon, surface currents flow across the IO basin carrying fresh Bay of Bengal (BoB) waters into the Arabian Sea (AS), the western EIO (Schott et al., 2009), and the eastern BoB (Han and McCreary, 2001; Jensen, 2003) (Fig. 2).

Wyrtki Jets (WJ): Strong eastward surface jets occur across the EIO during the inter-monsoon period, which are referred to as Wyrtki Jets (WJs) after their first discovery by Wyrtki in 1973. The EIO lacks steady equatorial easterlies because of the impedance of the rising branch of the Hadley cell caused by the Indian subcontinent. As a result, no climatic upwelling usually takes place in the eastern EIO (EEIO). However, coastal upwelling takes place along the eastern coasts of north-west Africa and the Arabian peninsula in the northern hemisphere driven by the rising branch of the Hadley cell and the south-west monsoonal currents during the summer. The process

results in a colder surface water conditions over the western EIO (WEIO) and a relatively warmer EEIO with relatively warm fresh water supplies from the BoB. The conditions favour the development of a net eastward flowing high pressure surface winds towards the relatively low pressure EEIO, identified as the WJs. The WJs prevail strongly during the inter-monsoons as the semi-annual westerly equatorial winds. They carry the warm WEIO surface waters eastwards thus decreasing the sea level in the west and increasing in the east. The WJs increase their spatial extent by reflecting from the eastern coastal boundaries as packets of Kelvin and Rossby waves. The WJs thus affect the upwelling regimes off Sumatra and help in the Indian Ocean Dipole (IOD) preconditioning (Schott et al., 2009).

IOD: The Indian Ocean Dipole (IOD) refers to the development of strong thermal dipole condition across the EIO due to the development of contrasting thermal conditions over the surface ocean. The mean thermal state of EIO is called the Indian Ocean Basin Mode (Yang et al., 2007). However, enhanced cold water upwelling along the western IO boundaries facilitates a negative IOD condition by developing strong cold water conditions over the surface waters of the WEIO. During negative IOD, warm surface currents flow from the WEIO to the east results in enhancement of moisture collection and increased precipitation over the EEIO. The coupled ocean-atmospheric circulation results in upwelling and shallowing of thermocline over the WEIO and a downwelling condition with deepening of thermocline over the EEIO. The positive IOD represents a cold surface water condition over the EEIO and a warm surface oceanic condition over the WEIO. The ocean-atmospheric convection and equatorial precipitation pattern is just opposite to that of the negative IOD condition (Saji et al., 1999; Webster et al., 1999) (Fig. 3). The positive IOD can be triggered by the El-Nino and the negative IOD by the La-Nina conditions as a result of cross basinal influence of El-Nino Southern Oscillation (ENSO) cycle operating over the equatorial Pacific region. However, in the absence of ENSO, the IOD can also occur independently by eastern tropical preconditioning and changes in the Walker circulation during global warming over the EIO (Vecchi et al., 2006); (Schott et al., 2009).

Cross-Equatorial Cell (CEC): The lack of continued equatorial easterlies and enhanced upwelling along the western EIO boundaries drive the IO's shallow overturning circulation, called as the Cross Equatorial Cell (CEC). This is unique to the IO than the other global oceans and is responsible for carrying most of the cross-equatorial heat transport. The CEC connects the South

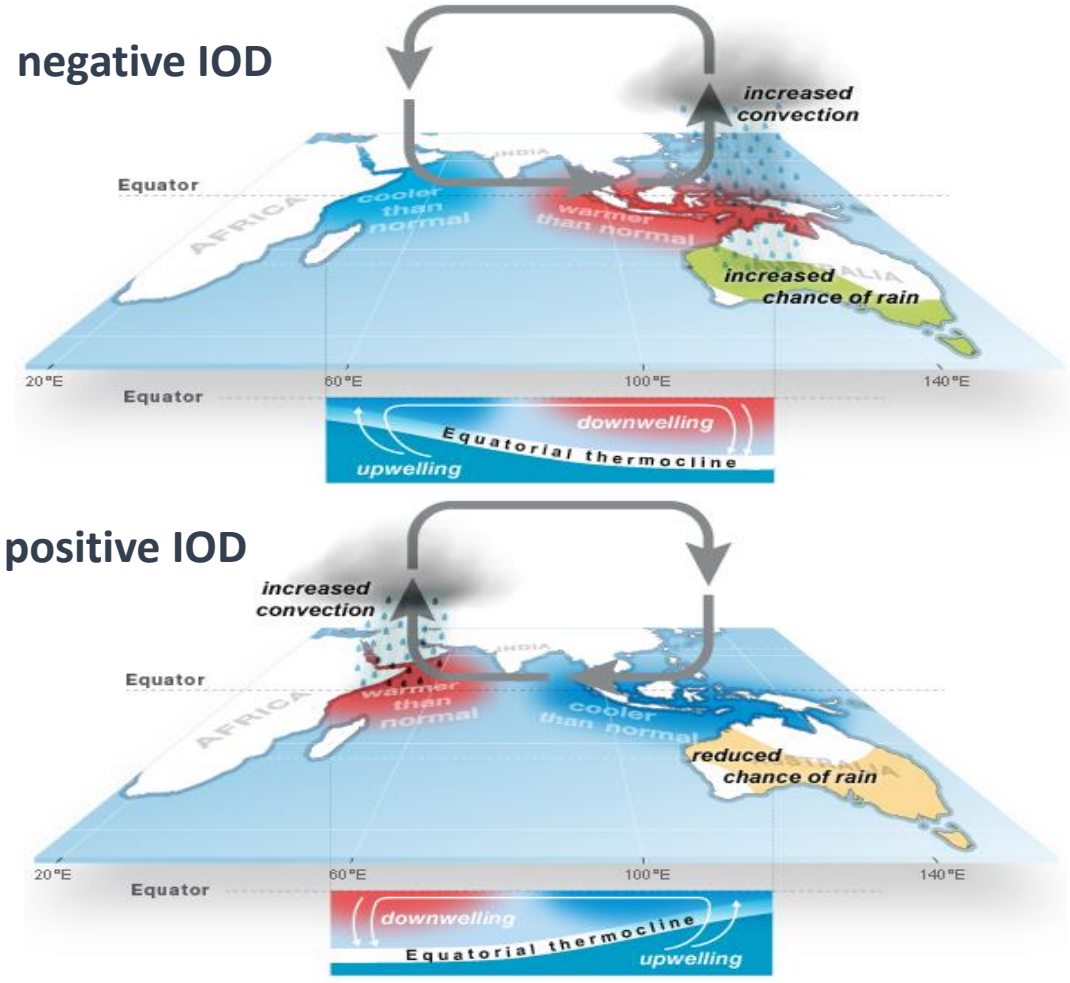

Image source: Australian Bureau of Meteorology

Figure 1.3: Schematic diagram of negative and positive phases of the Indian Ocean Dipole (IOD) phenomenon.

Equatorial Current (SEC) at the thermocline level with the northern upwelling sites present along the western boundary through the subsurface northward moving flow of the Somali Current. CEC derives its water source from three major regions in the Southern Hemisphere, i.e. from the recirculation of the subtropical gyre, from the subduction regions present across the southeastern subtropics, and from the Indonesian Through Flow (ITF) (Schott et al., 2009).

Equatorial Precipitation: The Sea Surface Temperature (SST) remains perennially high over the EIO belt due to high solar influx and the specific heat capacity of the ocean. The EIO thus remains under constant precipitation due to increased moisture collection and lower atmospheric condensation. The equatorial precipitation is enhanced during the off monsoonal periods when the ITCZ remains close to the geographic equator. Whereas, increased monsoon will drive a

substantial amount of moisture to be precipitated away from the equatorial belt (Bonnefille and Chalie, 2000)

1.3.2 Thermocline Water Mass Processes

Antarctic Intermediate Water: The Antarctic Intermediate water originates between the subtropical to sub-polar front in the southern hemisphere due to the convective upwelling of the modified Antarctic Deep Waters. Two distinct water masses are generated, i.e. the shallower Sub-Antarctic Mode Water (SAMW) and the relatively deeper Antarctic Intermediate Water (AAIW), which together penetrate into the lower latitudes to contribute to the EIO thermocline (Sverdrup et al., 1942)(You, 1998) (Spero and Lea, 2002) via ocean-tunneling ((Liu and Yang, 2003) (Fig. 2). The SAMW-AAIW contributes around 90% of the intermediate water source into the present EIO thermocline with a minimal contribution from the Indonesian Through Flow (ITF) (You, 1998). However, variation in the relative contributions are possible over the different paleoclimatic periods (Kuhnt et al., 2004).

Indonesian Through Flow (ITF): The Indonesian Through Flow (ITF) moves within the top 400m depth carrying upper oceanic waters from the equatorial Pacific into the EIO (Fig. 2). The water carried by ITF derives its origin from the North Pacific Mindanao Current (Gordon, 2005). It also has a subsurface core at intermediate depths which mostly derives water from the south Pacific (Gordon, 2005; McCreary et al., 2007). Variations in the ITF contributions can be associated with the ENSO (van Sebille et al., 2014) and IOD cycles operating over tropical Indo-Pacific region.

Red Sea Persian Gulf Intermediate Water (RSPGIW): High-salinity water mass Red Sea and Persian Gulf are combinedly addressed as the Red Sea Persian Gulf Intermediate Water (RSPGIW). The Persian Gulf Water has a relatively reduced southward extent compared to the Red Sea Water. The RSPGIW penetrates into the intermediate waters of the northwestern Indian Ocean up to the oceanic depths of ~1000–1200 m (TOMCZAK and GODFREY, 1994); (Kawagata et al., 2006) and extends further into the EIO (Fig. 2). Temporal variations in the equatorward contributions of the RSPGIW have been advocated with changes in the global mean sea levels over the glacial-interglacial periods through modelled estimations and paleoclimatic reconstruction studies (Kuhnt et al., 2004; Rippert et al., 2015).

Arabian Sea High Salinity Water (ASHSW): The ASHSW water forms in the upper northern AS due to reduced regional precipitation and increased surface cooling associated with cold North-East Monsoonal surface currents that result in significant increase in the salinity. Increased salinity increases the density of the water mass allowing it to sink and spread at subsurface depths contributing fluxes into the EIO and the BoB water masses (Sanchez-Franks et al., 2019); (Kumar and Prasad, 1999) (Fig. 2). Variations in the contributions of ASHSW into the EIO thermocline is strongly possible through changes in the production rates of ASHSW during the glacial-interglacial periods due to the Indian Monsoonal strength variabilities.

1.4 The Quaternary Glacial-Interglacial Periods

The Quaternary is the most recent geologic period in the history of the earth's evolution that initiated before 2.6Ma from the present. It has remained as the period of major environmental changes over the last 60 million years' record. Paleoclimatic reconstructions extending back to much earlier time periods could use the proxies that provide extensively long-term millennial records, yet extremely limited with the temporal resolutions along with the added problems of dating, sample preservation, data reproducibility and interpretations (Bender, 2013; Bradley, 2015). The study of the evolution of the Quaternary paleoceanography and paleoclimatology has thus acquired a primary scientific attention in order to understand the present-day trajectories and provide accurate estimations for the upcoming future for timely assessments and necessary preventions.

The Quaternary period has undergone a number of long and short term climatic cyclicities associated with the incoming cosmic flux variabilities. The variations in the cosmic influxes are primarily attributed to the different orders of earth's orbital cycles resulting in periodic changes in the incoming solar fluxes into the earth's atmosphere. These orbital cycles are designated as the Milankovitch cycles i.e. (i) Eccentricity (~100,00 yrs), the changes in the ellipticity of the earth's orbit around the sun, (ii) Obliquity (41,000 yrs), the changes in the tilt of the earth's rotational axis and (iii) Precession (23,000 yrs), the changes in the wobbling of the earth's rotational axis (Imbrie et al., 1992). The combined interferences of the Milankovitch cycles and the complex feedback mechanisms arising from the mutual interactions through the earth's climatic system have resulted in the development of composite patterns in the earth's climatic cyclicities. The continental ice sheets have responded finely to the immediate variations in the incoming solar fluxes through

constant variations in the magnitude of total ice sheets formed over the earth's polar to sub-polar regions (Gornitz, 2009). The cold periods with extensive ice-sheet formations are called the 'Glacials', whereas the warm periods associated with reduced ice-sheet formations are called the 'Interglacials'. The most recent glacial period occurred around ~120 ka to 11.5 ka, after which the earth has undergone the last interglacial period called the Holocene. In addition to the long-term divisions based on ice sheet volumes, the Quaternary is also divided into a number of Marine Isotopic Stages (MIS) based on the isotopic ratios obtained from the globally distributed benthic foraminiferal oxygen-isotopic ratios ($\delta^{18}O$). The MIS with relatively lower $\delta^{18}O$ records represent the warmer climatic stages and are assigned the odd numbers' series (e.g. MIS 1, MIS 3 etc), whereas those with relatively higher $\delta^{18}O$ records represent the cooler climatic stages and are assigned the even numbers' series (e.g. MIS 2, MIS 4 etc) (Lisiecki and Raymo, 2005). Around 100 MIS have been reported over the last 2.6 million yr Quaternary period, out of which the last 3 MIS come under the radiocarbon age detection limit (Groeneveld et al., 2014). The Quaternary period also observes small scaled sub-Millankovitch cycles identified by massive iceberg discharges in the polar regions that were initiated from the short-term abrupt warming followed by relatively slow and persistent cooling. The 1-2kyr North Atlantic iceberg discharge events are identified as the Heinrich events (H-events). The Heinrich events take place within the coldest phases of the long-term cooling cycles during which the largest ice shelves might have grown or the highest calving rates in climatically sensitive ice might have occurred (Broecker et al., 1992)(Bond et al., 1993). Relatively shorter centennial warm events have been identified as the Dansgaard-Oeschger (D/O) events (Benson et al., 1996). The D/O cycles result from rapid shifts in temperature from the cold glacial climate to the warm glacial climate during the Wisconsinan Glaciation (~115-19 ka: (Gornitz, 2009), which has been observed from the $\delta^{18}O$ records from the North Atlantic sediment cores. The other Quaternary events with primal climatic significance include the Last Glacial Maximum (LGM), the Bølling Allerød Warming (BA), the Antarctic Cold Reversal (ACR), the Younger Dryas (YD) and the 8.2 ka cold event during the early Holocene. The LGM was the period of maximum global ice-sheet extension (Mix, 2001). Different paleoclimatic studies have reported an average occurrence timing of LGM between 18-25 ka. However, attributing an exact global timing for LGM remains debatable which can be regionally variable (Clark et al., 2009; Gornitz, 2009). The BA Warming was the warm phase of the Weichselian last glacial-interglacial termination, which occurred around ~12.7 -15 ka. The YD

was the North Atlantic cold event that took place around ~11.5-12.7 ka. possibly caused by the reduction in the Atlantic Meridional Overturning Cycle (AMOC) resulting from the increased meltwater contributions from the northern ice sheets. The Holocene is the last Epoch of the Quaternary climate that has remained as an interglacial since around 10-11 ka (Gornitz, 2009).

1.5 Development of Oceanic Thermocline and its Climatic Significances

1.5.1 The Oceanic Thermocline

The oceanic thermocline represents the shallow intermediate water mass region in the subsurface ocean where the temperature profile observes a rapid decrease in its value with increasing depth. The sharp temperature gradient is developed due to the differential distribution of oceanic heat in the vertical water column (Boccaletti et al., 2004). Out of the total influx incident over the oceanic surface, around 50% gets reflected back into the atmosphere. Around 90% of the total radiation transmitted into the ocean, gets absorbed within the upper 50-100m sunlit zone. The depth of the sunlight zone can be shallow over high saline water mass regions. Below ~200m, the amount of light is insufficient to facilitate photosynthesis. Absolutely no light enters below ~800-1000m and the region is rather isothermally stable. The surface ocean remains heated due to constant solar insolation (American Meteorological Society., 2018). The surface wind and wave actions result in a warm Mixed Layer (ML) present as the top most layer of the ocean. The bottom and deep ocean remain at cold temperatures around ~0-4°C due to the constant ventilation by the global Thermohaline Circulation (THC) produced at the high polar to sub-polar latitudes (Luyten et al., 1983). A strong temperature gradient is thus developed in the shallow intermediate oceanic depth due to the downward heat loss caused by thermal conduction, convection, dispersion and diffusion. The process of heat loss is usually non-linear which is primarily attributed to the process of thermal conduction, which reduces with reducing thermal gradient between the confining layers, as well as the regional subsurface water mass circulations taking place at the thermocline depth (Boccaletti et al., 2004).

1.5.2 Development of Thermocline Structure

The oceanic temperature remains more or less constant within the ML. The thermocline originates below the ML with a gradual increase in the slope (dT/dD, T: Temperature, D: Water Depth). The slope of the thermocline increases rapidly at the shallow depth to reach its maximum after which it undergoes gradual reduction to become more or less constant into the sub-thermocline and deep

ocean. The general pattern of thermocline shows a more or less exponential-fit curve with a relatively sharp concave-up structure in the upper segment and a relatively gentle convex-up structure in the lower segment (Fig. 4). General considerations have been undertaken to define the thermocline parameters for regional and global scale comparisons and assessments (Kessler, 1990; Kessler et al., 1995; Meyers, G., 1987). The individual structure of oceanic temperature profiles around the global oceanic regions are however distinctly variable subjecting to the regional and local variations in net solar insolation, surface wind and current patterns, terrestrial and riverine water mass influxes and the subsurface advective watermass transfers (upwelling, downwelling, advective and diffusive mixing) (Boccaletti, 2005).

Objective approaches have also proved a distinct mismatch between the empirical values and the objectively defined methods through the modelled analyses (Fiedler, 2010). Hence, characterizing the structural parameters of a thermocline based on the nature of the thermocline slope variability is a better approach to describe the individual thermoclines (Pizarro, 2004); (Chu and Fan, 2019). The following is a description of different objective parameters associated with the general structure of an oceanic thermocline (Fig. 4).

The Main Thermocline: The main thermocline represents the subsurface oceanic region that observes distinct changes in the oceanic temperature. The main thermocline extends from the top of thermocline to the base of thermocline.

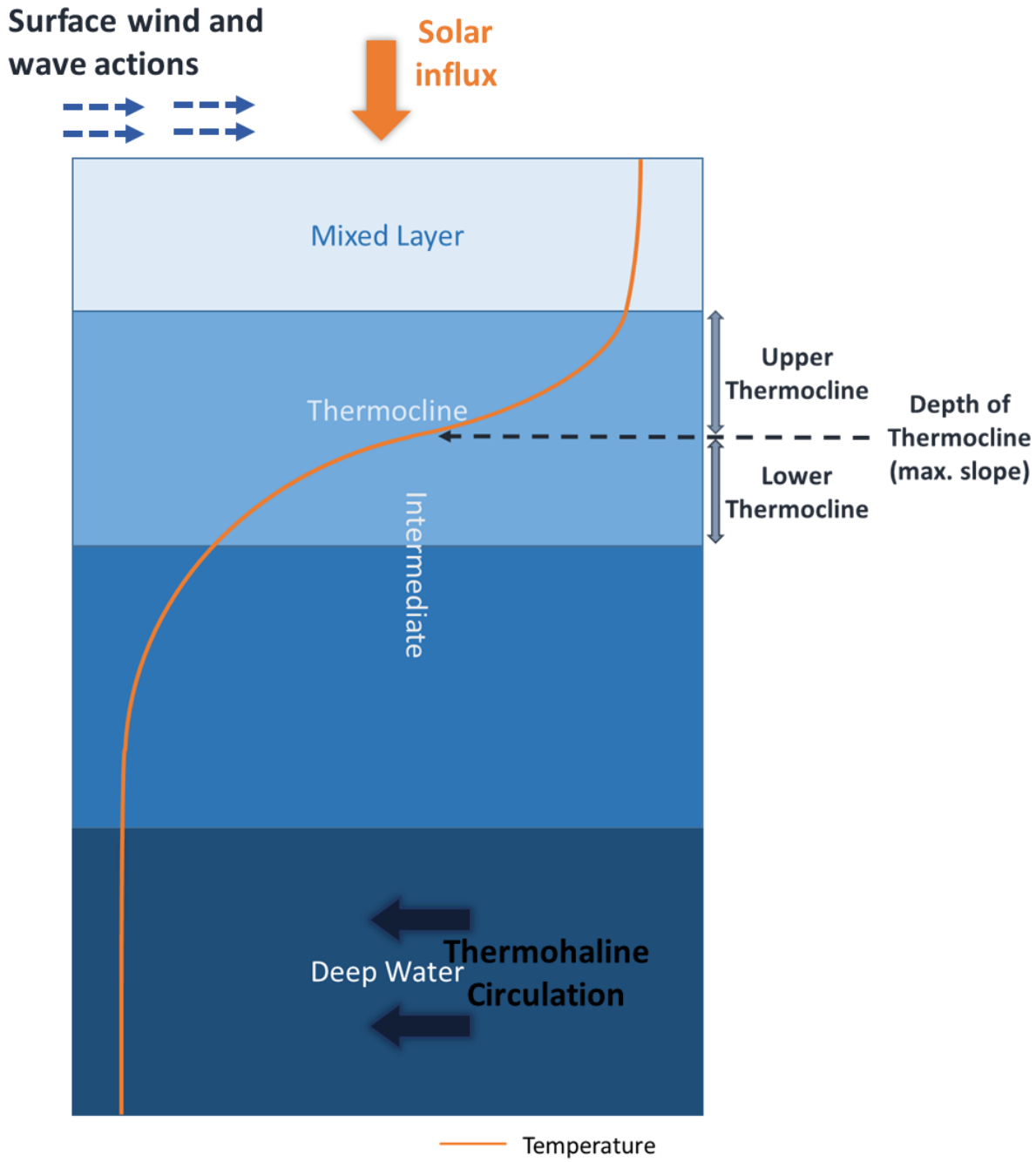

Figure 1.4: Schematic showing the general structure of a tropical oceanic thermocline (Modified after (Chu and Fan, 2019)).

The Top of Thermocline: The top of thermocline marks the beginning of the increase in the slope of thermocline. For practical purposes, the top of thermocline coincides with the base of the ML i.e. the Mixed Layer Depth (MLD). Different conventions have been followed by global research communities to attribute a general quantitative description to the identification of MLD. A ΔT_d ($T_{surface\ ocean(SST)} - T_{at\ subsurface\ depth\ 'd'}$) of 0.5°C *(Monterey, Grigory Isayev, 1954-1999 ; Levitus, 1997)* or 0.8°C *(Kara et al., 2000)* has been considered by several research studies to undertake the subsurface depth 'd' as the regional oceanic MLD. A $\Delta T_d = 0.8$°C is commonly accepted for a general global scale representation by the World Ocean Atlas (WOA) community at present. However, for practical scientific studies the MLD can vary from locally to regionally throughout the globe due to various regional and local surface and subsurface ocean-atmospheric variabilities. In order to determine the MLD i.e. the top of thermocline, for individual oceanic temperature profiles, the fundamental approach of 'Inflection Point' method (Thomson and Fine, 2003) is appropriate. Using this method, the MLD or top of thermocline can be identified as the depth of the first thermal slope optimum obtained from the second order derivative of the oceanic temperature profile from the surface ocean.

Strength of Thermocline: The strength of thermocline is the measure of the maximum slope attained within the thermocline.

Depth of thermocline: The depth of thermocline is the measure of the depth of the maximum slope of thermocline (strength of thermocline) from the surface ocean.

Base of Thermocline: The base of thermocline represents the lower limit of the main thermocline. For an individual oceanic temperature profile, the base of thermocline can be identified following the inflection point method (Thomson and Fine, 2003) i.e. the depth of the second thermal slope optimum obtained from the second order derivative of the oceanic temperature profile. Studies have also used specific isotherm depths as the representatives of the base of the regional thermoclines for the sake of operational simplicity in understanding the regional thermocline variabilities as well (Meyers, G., 1987; Kessler, 1990; Kessler et al., 1995).

The upper thermocline: The upper thermocline extends from the top of thermocline to the depth of thermocline.

The lower thermocline: The lower thermocline extends from the depth of thermocline to the base of thermocline.

1.5.3 Climatic Significances of the Oceanic Thermocline

The thermocline acts as a layer of stratification providing a stable ecological platform for the microbial survival and growth. The oceanic thermocline witnesses major transitions in the characteristic physical and chemical oceanic parameters such as the sea water density, salinity, oxygen and carbon ion concentrations and the primary productivity, which are strongly governed by the processes directly or indirectly linked with the oceanic temperature (Longhurst et al., 1995; Schmitz, 2018; Shapiro, 2009). It also plays a significant role in the oceanic-atmospheric heat and gaseous transactions, providing long term climatic stability by transferring the surface climatic anomalies into the subsurface and deep ocean (Schott et al., 2009) (Pagani et al., 2010). The understandings of the characteristics and dynamics of the oceanic thermocline is thus critical for the oceanographic, climate and the marine ecosystem studies.

1.6 Implication of Paleothermocline Reconstructions

The thermocline represents a unique division of oceanographic studies that combinedly interconnects the peripheral domains of surface, subsurface and deep oceans as well as the governing atmospheric and climatic variabilities. The thermocline acts as a bridge between the distinct domains of oceanography such as the surface, the subsurface and the deep oceans. It also interconnects the atmosphere through the active inter-dependent climatic processes. Variations in any of the ocean-atmospheric phenomenon can thus result in a significant change in the characteristic parameters of the oceanic thermocline such as its strength, depth and thickness within the water column. Study of the paleothermocline reconstruction thus helps in providing critical information about the temporal evolutions of the past oceanic and atmospheric systems and their dynamic implications towards the regional and global paleoclimatic variabilities.

Obtaining direct observations about the past oceanic water mass conditions is however clearly not possible. Indirect recorders of past climatic signatures, called the proxies are thus essential to reconstruct and understand the past climatic variations. The paleothermocline reconstruction necessitates finding typical proxies that can effectively preserve the past oceanic signatures from characteristic depths in the oceanic water column. Additionally, the proxies should also be able to remain well preserved under the diverse past climatic conditions over long time periods and should

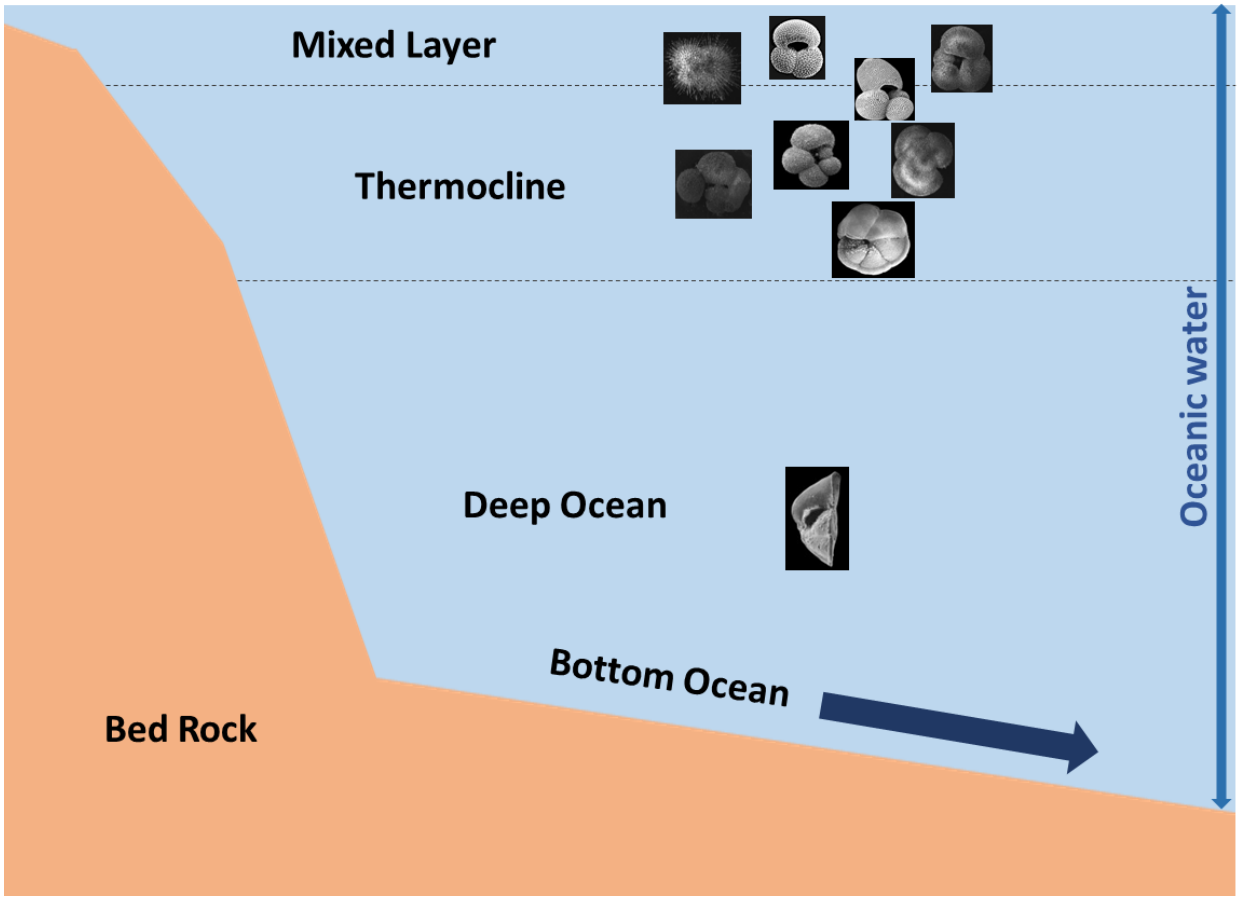

Credits (SEM images of planktonic foraminifers): M. Murugunantham and microtax.org

Figure 1.5: A schematic of vertical oceanic distributions of depth specific planktonic foraminifers.

be retrieved and reproducible under the laboratory conditions to obtain appropriate information about the past oceanic and climatic conditions.

1.7 Planktonic Foraminifera as Proxy

The planktonic foraminifers are a group of calcareous micro-organisms that represent wide distributions in the global ocean at different water depths extending from the surface into the deep ocean (Berger, 1969) (Fig. 5). The planktonic foraminifers are characterized by their floating nature of survival within the water column. They are single celled protists with one or more chambers imbibed into the cells. The average length of the cell varies from ~100 μm to 1 mm (Schiebel and Hemleben, 2017).

Planktonic foraminifers first appeared in the world ocean around ~200 Ma since then they have undergone a rapid history of evolution which makes them an ideal proxy for the paleo bio-stratigraphic studies. Their sensitivity to different physical, chemical and biological changes in the

co-existing environment has made them a classic tool for the paleo-oceanographic, paleoclimatic and paleo-ecological reconstruction studies (Table 1.1). The individual planktonic foraminifers can incorporate characteristic geochemical elements from the sea water during the shell calcifications that can provide critical information about the existing oceanographic and climatic conditions. The fossilized planktonic foraminifers have thus played an instrumental role in the reconstruction of paleocaonographic and paleoclimatic records owing to their prolific productions and excellent preservation potentials across the global oceans (Crosta and Koç, 2007) and are considered to form the backbone of Cenozoic biostratigraphy (Berggren, Kent, Swisher, & Aubry, 1995).

1.7.1 Description of Planktonic Foraminifers

The following is a description of the selected planktonic foraminifer species used in this study for the reconstruction of the EIO paleothermocline from characteristic oceanic water depths. ***Globigerinoides ruber (s.s.)*****:** *Globigerinoides ruber (s.s.) (sensu-stricto) (G. ruber (s.s.))* is a shallow ML dweller with a ruber type wall structure. The structure of the shell is medium trochospiral with three symmetrical and spherical chambers present per each whorl. Bi-lateral symmetry and two smaller secondary apertures on the spiral side are characteristics of the ideal form (Wang, 2000). An interiomarginal primary aperture with two wide high arched supplementary sutures also comprise the distinct shell features (Hemleben et al., 1989). *G. ruber (s.l.) (sensu-lato)* is the morphological symbiont of *G. ruber (s.s.)* and is distinguished by its compact tests with non-spherical and slightly compressed chambers. *G. ruber (s.s.)* is the most frequently available species in tropical and subtropical oceans (Be, 1977) and has been extensively used for the paleo oceanographic and paleoclimatic reconstructions of the surface oceanic studies (Divakar Naidu and Malmgren, 1999; Liu et al., 2021; Saraswat et al., 2023; Schmitt et al., 2019; Spero et al., 2003).

Table 1.1: Planktonic foraminifers as the paleoclimatic reconstructors.

Climatic parameters	Tracer	Planktonic Species	References
Chronology of marine sediment core and sea water radiocarbon reconstructions	$\Delta^{14}C$	*G. ruber* and *T. sacculifer* for ML and *G. menardii* for Thermocline	(Broecker et al., 1999; Stuiver et al., 1998) (Hughen, 2007)(Adkins and Boyle, 1997a)
Paleo sea water temperature reconstructions	Mg/Ca	*G. ruber*, *T. sacculifer*, *G. siphonifera* and *G. menardii*	(Hollstein et al., 2017; Sagawa et al., 2012)
Paleo sea water salinity reconstructions	Mg/Ca and $\delta^{18}O$	*G. ruber*, *T. sacculifer*, *G. siphonifera* and *G. menardii*	(Mahesh and Banakar, 2014) (Weldeab et al., 2006) (Srivastava et al., 2007) (Erez and Luz, 1983)
Paleo-monsoonal strength variability	Mg/Ca and $\delta^{18}O$	*G. ruber*	(Banakar et al., 2010a)
Past variability in the Arabian Sea High Salinity Water (ASHSW)	Mg/Ca and $\delta^{18}O$	*T. sacculifer*	(Mahesh and Banakar, 2014)

***Trilobatus sacculifer*:** *Trilobatus sacculifer (T. sacculifer)* is an abundant tropical to subtropical mixed layer species (e.g., Bé 1977; Schmuker and Schiebel 2002) and probably second to *G. ruber* in its abundant use in the paleooceanographic reconstructions of the surface mixed layer. T. sacculifer resides at relatively higher depths than *G. ruber* within the ML (Mohtadi et al., 2009); (Zhang et al., 2019). The general structure of the shell comprises of 3-4 spherical chambers with a distinctly elongated and sac-like final chamber, named as *T. sacculifier* with sac (w/s). The shell shows a narrow umbilicus with an interiomarginal primary aperture showing a distinct arc bordered by a rim. *T. sacculifer* observes three additional morpotypes with primary differences in the shapes of the final chamber identified as *Trilobatus quadrilobatus* (d'Orbigny 1846), *Trilobatus trilobus* (Reuss 1850) and *Trilobatus immaturus* (Leroy 1939). *T. sacculifer* is frequently present in the oligotrophic water mass conditions (Naidu and Malmgren, 1996); (Schiebel et al., 2004) such as the EIO. The *T. sacculifer (w/s)* usually represents an adult stage

with a preferentially MLD habitat in order to fulfil the food requirements from the Dissolved Chlorophyll Maximum (DCM) during their reproductive cycles (Schiebel and Hemleben, 2017).

***Globigerinella siphonifera*:** *Globigerinella siphonifera* (*G. siphonifera*) is the most frequently occurring planktonic foraminiferal species in the tropical to subtropical oceans (AD, 1839). The characteristic structure of the shell exhibits a low trochospiral to irregular planispiral structure with round to triradiate spines and ovate chambers during the late ontogenic period. Around 4.5–5 chambers are present in the last whorl of early adult phases and 5–6 chambers in the late ontogenetic stages.

Two structural morphotypes of *G. siphonifera* are observed. The Type I is the common structure with relatively large and evolute chambers with larger pores along with a higher spine density. The Type II represents a relatively slender and involute chambers with smaller pores and a lower spine density than the Type I. The common structure with relatively large and evolute form of chambers with larger pores along with a higher spine density. Type I specimens are characterized by a larger pore size and more open coiling than Type II specimens (Bijma et al., 1998). The Type 1 has been considered for the present study approach.

Globorotalia menardii: *Globorotalia menardii* (*G. menardii*) is a frequent cosmopolitan species observed in the tropical and subtropical oceans under less productive water mass conditions Kroon and Ganssen 1989; Ufkes et al. 1998; Conan and Brummer 2000; Schmuker and Schiebel 2002; Schiebel et al. 2004. The characteristic shell structure shows a low trochospiral and large discoidal test with around 5-5.5 chambers in the last whorl. A thick well developed keel is prominent around the aperture. The sutures are usually curved on the spiral side but straight on the apertural side (Parker et al., 1865)(Hemleben et al., 1977). *G. menardii* has been largely used as a thermocline species in paleoceanographic reconstruction studies (Fairbanks et al., 1982); (Mohtadi et al., 2009; Stainbank et al., 2019).

1.7.2 Elemental and Isotopic Proxies for Paleoclimatic Reconstructions

Three major planktonic foraminiferal proxies have been used in the present study for the paleoclimatic reconstructions from the upper EIO paleothermocline that include (i) the radiocarbon ($\Delta^{14}C$), (ii) the Mg/Ca and (iii) the stable oxygen isotopic record ($\delta^{18}O$). A brief description of the individual proxy parameters and their utility in paleoceanographic and paleoclimatic reconstructions are described below.

1.7.2.1 Mg/Ca

The Mg/Ca ratio of planktonic foraminifer is a direct proxy indicator of the sea water temperature condition under which the foraminifers calcified. Both Magnesium (Mg) and Calcium (Ca) are conservative elements with average residence times of ~13My and ~1My respectively (Lebrato et al., 2020). Hence, can be suitably used for paleotemperature reconstructions of ocean over glacial-interglacial time scales. The sea water Mg replaces into the crystal structures of calcitic foraminifers through ionic substitutions due to comparable ionic size and charge with respect to the Ca (Fig. 6). The replacement is temperature dependent and the Mg/Ca shows an empirically exponential relationship with the sea water temperature (Nürnberg et al., 1996) (Anand et al., 2003) which is given as:

$$Mg/Ca = B \exp (AT)$$

Where Mg/Ca is expressed in mmol/mol. 'A' and 'B' are exponential and pre-exponential constants respectively. Mg/Ca is the average shell ratio of analyzed 'n' number of samples and T (°C) is the corresponding sea water temperature of planktonic foraminiferal calcification.

The magnitudes of 'A' and 'B' are region specific, species-specific and foraminiferal size specific. Various sets of calibration equations have been developed through extensive calibration studies using cultured experiments, plankton-tow, sediment trap and core-top sample analyses throughout different global oceanic regions, considering the choice of individual species and the specific size fractions of foraminifers (Anand et al., 2003; Dekens et al., 2002; Gray et al., 2018; Holland et al., 2020; Regenberg et al., 2009). However, in case of lack of adequate samples multi-proxy calibrations have been obtained and size restrictions are also compromised to the best possible extents (Elderfield and Ganssen, 2000a; Sagawa et al., 2012).

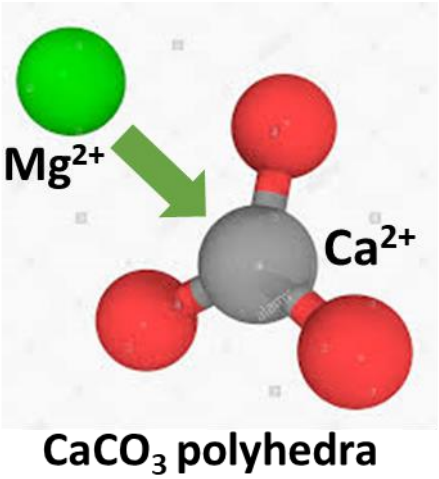

Figure 1.6: Replacement of Magnesium into Calcite polyhedra.

Edited image from © Science Photo Library Limited 2023

1.7.2.2 Radiocarbon ($\Delta^{14}C$)

Radiocarbon is the radiogenic form of the naturally occurring carbon in the earth's atmosphere. It is produced in the upper atmospheric region through the interactions of cosmogenically produced thermal neutrons with the atmospheric nitrogen atom. The production reaction can be represented as:

$$^{14}N + n \longrightarrow {}^{14}C + p$$

where, n is neutron and p is proton. Mean production rate of radiocarbon in atmosphere is around 1.7 atoms $cm^{-2}.s^{-1}$ (Roth and Joos, 2013). The Radiocarbon atom decays by emitting β-particles at energy of 156 keV. This decay converts the radiocarbon into a stable nitrogen atom given as:

$$^{14}C \longrightarrow {}^{14}N + \beta^- + \nu_e^- + Q$$

where, ν_e^- is antineutrino and Q is the energy of beta decay.

After production, the cosmogenic radiocarbon gets readily oxidized forming the atmospheric carbon dioxide and gets dispersed into different global carbonate reservoirs (Fig.7). The oceans incorporate the atmospheric carbon dioxide into dissolved water form through the constant processes of ocean-atmospheric equilibrium transactions integrating it as a part of the total Dissolved Inorganic Carbon (DIC). The planktonic foraminifers incorporate the sea water radiocarbon signatures from the surrounding water mass during the process of shell calcification. Thus, obtaining the radiocarbon records from the individual planktonic foraminifers can provide clear information about the past sea water radiocarbon concentrations of the coexisting water mass and its variability in order to estimate the age, the water mass ventilations and the radiocarbon transactions between different carbonate reservoirs (Broecker et al., 1990, 1988; Shackleton et al., 1988) over the past climatic periods.

The carbonate shells of the planktonic foraminifers can be extracted from the sediment cores spanning over past millennial scales and dated using Accelerator Mass Spectrometer (AMS) in order to obtain the radiocarbon ages of the foraminiferal carbonates (Crosta and Koç, 2007; Lynch-Stieglitz and Marchitto, 2013). The principle of radiocarbon dating is based upon the fundamental law of radioactivity that requires an initial and final concentrations of the target element and the half-life of the decay process. The radiocarbon has a half-life of 5730±40 yrs that makes it an appropriate proxy for the paleo age reconstructions up to the last ~55,000 yrs. The radiocarbon age

reconstruction method considers the atmospheric ^{14}C records of 1950 (the pre-bomb era) as the standard initial atmospheric concentration. However, the atmospheric radiocarbon production rate has varied with time (Köhler et al., 2006), which requires an appropriate calibration in order to obtain the true age of the fossil samples. In addition, a difference between the calculated ages of the surface ML and the atmosphere is observed due to an offset in the equilibrium transaction of radiocarbon between the ocean and atmosphere, and due to the global thermohaline circulations. This offset is called the global mean reservoir age (R). Temporal variations in R, are restricted to the globally averaged ML reservoir age, which have been incorporated into the Marine20 calibration curve (Heaton et al., 2020). Local disequilibrium effects resulted from local water mass advections and surface/subsurface currents also produce further variations in the actual age calculations, which has been termed as local reservoir age. The global radiocarbon community (INTCAL group) has efficiently worked out to produce well refined atmospheric radiocarbon calibration curves using the known age samples of tree rings, corals, varved sediments and speleothems combined with modelled simulations based on cosmic rays, solar influx and variations in earth's magnetic fields. The INTCAL group also provides estimations for region specific local reservoir age corrections (ΔR) along with the global mean reservoir age (R). Temporal variations in ΔR, are believed to be insignificant with respect to the corresponding values of R, and hence assumed to be constant over time (Heaton et al., 2020). The radiocarbon ages of the surface oceanic planktonic foraminifers are calibrated for both the global and local reservoir age effects (R and ΔR respectively) (Heaton et al., 2020; Stuiver et al., 2021) in order to obtain the actual age and chronology of the sampled sediment core. The sea water radiocarbon records from specific oceanic depths are obtained using the respective radiocarbon age and the corresponding calendar age (chronological age obtained from surface planktonic foraminifers) in the equation for sea water radiocarbon reconstruction given by (Adkins and Boyle, 1997b). The radiocarbon concentration of a given sample is represented by the 'Δ' notation with a unit of '‰' after normalizing its activity with respect to the oxalic acid standard (OX) that represents the mean atmospheric radiocarbon activity of the 1950's atmosphere.

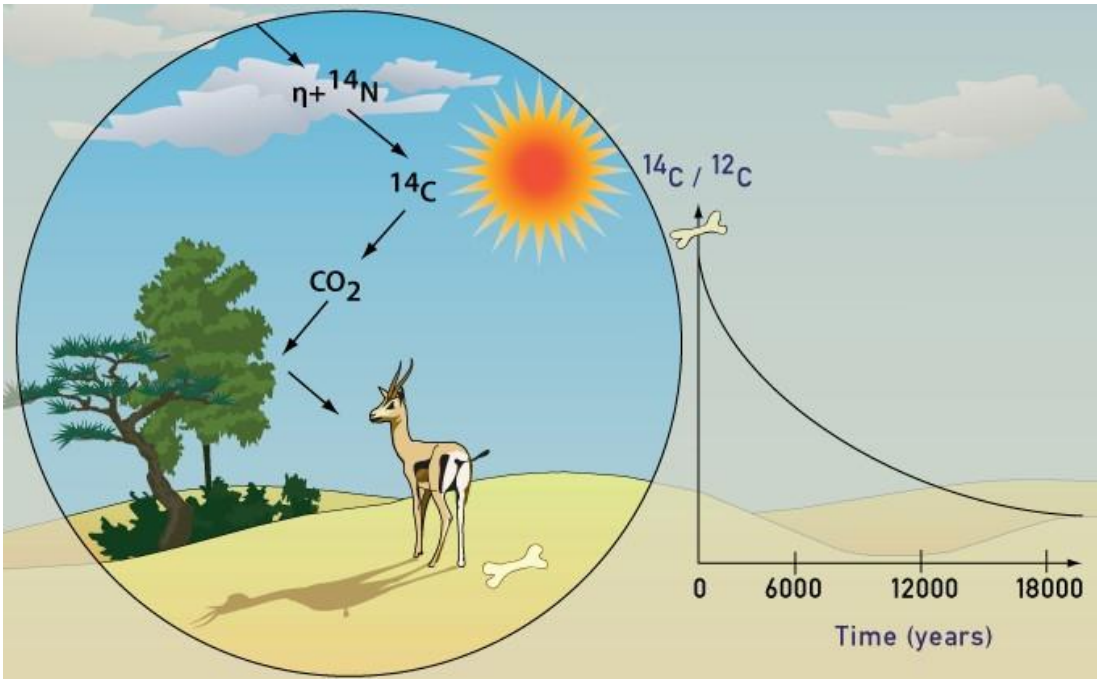

Source: www.naturphilosophie.co.uk

Figure 1.7: Schematic diagram showing basic process of radiocarbon dating technique.

1.7.3 Stable Oxygen Isotopic Ratio ($\delta^{18}O$)

The oxygen isotopic ratio ($\delta^{18}O$) of planktonic foraminifers varies as a function of temperature and oxygen isotopic ratio of the coexisting sea water during the timing of calcification. The near equilibrium calcification of the foraminifers with the sea water oxygen isotopic ratio ($\delta^{18}O_{SW}$) has made foraminifers suitable to be used as a primary proxy in the study of paleoceanographic reconstructions (Shackleton, 1967; Ravelo and Hillaire-Marcel, 2007). The $\delta^{18}O_{SW}$ shows strong empirical relationship with the sea water salinity (S_{SW}) since both of them are governed by the common ocean-atmospheric processes of evaporation, precipitation, advection (upwelling, downwelling and external water mass influx) as well as diffusive water mass transfer processes (Rohling and Bigg, 1998)(Benway and Mix, 2004); (Craig and Gordon, 2013).

Fractionation of oxygen isotope take place during the equilibrium transactions between the foraminiferal shell and the co-existing sea water during the process of calcification. The degree of fraction varies as a function of the existing sea water temperature conditions. A paired Mg/Ca and $\delta^{18}O$ analysis of foraminifers provides a suitable mean to obtain the actual $\delta^{18}O$ records of the existing sea water in order to obtain the actual $\delta^{18}O$ records of the existing sea water mass after

eliminating the sea water temperature factor. The obtained $\delta^{18}O_{SW}$ records can be suitably used to reconstruct the past sea water salinity using appropriate regional $\delta^{18}O_{SW}$ vs Salinity calibration equations (Banakar et al., 2010a; Elderfield and Ganssen, 2000b).

Variations in the sea surface salinity is predominated by the net Evaporation-Precipitation balance, under a given in-situ water mass condition, whereas, advective mass transfers play the primary roles in governing the thermocline and deep oceanic regions. Paleo salinity reconstruction studies have thus been significantly useful in understanding the surface and subsurface oceanographic, atmospheric and coupled climatic variabilities with wider scale global implications over the past millennial climatic periods (Elderfield and Ganssen, 2000b);(Banakar et al., 2010b; Benway et al., 2006)(Banakar et al., 2010a).

The oxygen isotopic ratio is generally represented by the 'δ' notation with the unit of '‰' after normalizing the sample value with respect to the international standard 'Vienna Pee Dee Belemnite (VPDB)' (for carbonates) or 'Vienna Standard Mean Ocean Water (VSMOW)' (for water).

$$\delta^{18}O = [\ (^{18/16}O_{(\text{carbonate or water})} / ^{18/16}O_{(\text{VPDB or VSMOW})}) - 1\ ] * 1000$$

1.8 Review of Paleothermocline Studies over EIO

Paleothermocline reconstruction studies are sparse over the EIO due to the strategic challenges faced in finding abundant number of foraminiferal samples from the productivity limited EIO region. A limited number of attempts have been carried out so far from the eastern and the western boundary regions using a single planktonic foraminiferal proxy representation for the EIO paleothermocline ((Mohtadi et al., 2010a; Kwiatkowski et al., 2015; Pang et al., 2021) and (Rippert et al., 2015) respectively) (Fig.8). A brief discussion of the available studies along with their proxy approach and scientific outcomes is presented below.

Sediment core GeoB 10038-4 (~6°S, 103°E, 1819 m water depth, off SW Sumatra) was studied by Mohtadi et al., 2010a in order to understand the Late Pleistocene surface and thermocline conditions of the eastern tropical Indian Ocean over the last 133 ka using foraminiferal Mg/Ca and $\delta^{18}O$, alkenone based paleothermometry and sediment derived terrigenous fraction records. Planktonic foraminifers *G. ruber* and *N. dutertrei* were used as surface and thermocline (upper thermocline (Mohtadi, 2009)) depth representatives. The study infers that the annual mean temperatures of surface and thermocline water varied independently and differently. The surface

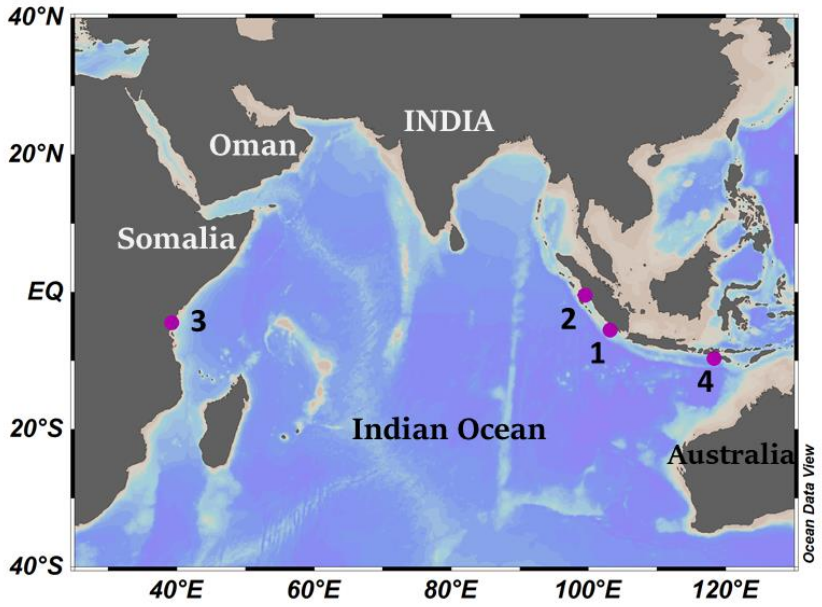

Figure 1.8: Locations of available thermocline studies from the EIO. 1. GeoB 10038-4 (Mohtadi 2010) 2. SO 189-39KL (Kwiatkowski 2015) 3. GeoB12610-2 (Rippert 2015) 4. MD98-2165 (Pang 2021).

temperatures seemed to be controlled by the southern high-latitude climate, whereas the thermocline temperatures were better influenced by the North Indian Ocean thermocline variabilities. Paleosalinity reconstructions indicated that variations in the boreal summer monsoon intensity did not considerably affect the annual mean conditions over the studied region, except for the glacial terminations. Glacial–Interglacial variability pattern is not observed in the thermocline conditions and the response of the tropical Indian Ocean thermocline to the mid and high-latitude climate appeared to be non-linear.

The second attempt of paleothermocline reconstruction was made by Kwiatkowski et al., 2015 from the EEIO, where they studied the sediment core SO 189-39KL (0°47.40S, 99°54.51E, water depth 517m) taken off western Sumatra in order to understand the Holocene variations in the thermocline conditions over the eastern tropical Indian Ocean over last 8 ka. Upper thermocline planktonic foraminifera species *P. obliquiloculata* (Mohtadi et al., 2009) was taken as the thermocline species. The surface temperature records were inferred from Mohtadi et al., 2014 that is based on the choice of *G. ruber* species. The study observes strong climatic interconnections between the Indian monsoon system, the El-Nino Southern Oscillation (ENSO) and the IOD through various climatic feedback mechanisms, and the mutual control of these processes on the

Indian oceanic climate system. The thermocline remained deeper during 8 ka to 3 ka, whereas shoaling of thermocline was observed after 3 ka possibly because of increased upwelling associated with a more positive IOD condition.

Rippert et al., 2015 studied a sediment core GeoB12610-2 (04˚49.000S, 39˚25.420E, 399m water depth) located off Tanzania in order to address the fluctuations in the western tropical Indian Ocean thermocline during the past 35 ka. The study used *G. ruber* and *N. dutertrei* as the surface ocean and the thermocline (upper to mid thermocline) species. The results show around 2.5˚C of surface cooling and around 3.5˚C of cooling in the thermocline observed during the glacial period compared to the present. A shallower thermocline (reduced stratification) was observed during the cold glacial period but a deepening of thermocline (increased stratification) during the warm deglacial and Holocene time periods. The similarity between the glacial temperatures of Antarctic EDML curve and the WEIO thermocline indicated possible contribution of Southern Oceanic Intermediate waters during the glacial period. However, rising sea level during the warmer deglacial period resulted in increased contributions from the Red Sea Water (RSW) and the Indonesia Intermediate Waters and decreasing the contributions from the Southern Oceanic Intermediate waters. The thermocline depth variations showed opposite patterns compared to the eastern Indian Ocean from the last glacial to the present.

Pang et al., 2021 studied the sediment core MD98-2165 (9.65°S, 118.34°E, 2100m water depth) from the south of Lombok Strait in order to understand the ITF variability over the last two glacial-interglacial cycles (up to 270 ka) from the eastern Indian Ocean region. The study uses the upper thermocline species *P. obliquiloculata* (Mohtadi et al., 2009) to infer that the ITF strength was weaker during MIS 6 and MIS 2-4 compared to the late Holocene, and it was enhanced during MIS 8, MIS 7, MIS 5 and the early Holocene. The ITF strength variability showed strong associations with the solar scale precession cycles advocating the importance of southeast monsoonal winds on the ITF strength variability. The study also suggests influence of glacial-strength variability. It also suggests the influences of glacial-interglacial sea level changes on the modification of ITF pathways.

1.9 Research Gap and Motivation

The EIO thermocline plays a significant role in contributing to the regional and global climatic variabilities, providing strong climatic feedbacks to the atmospheric overturning

circulations and (the atmospheric) hydrologic cycles, through changes in its mean thermal state across the tropical IO (Held and Soden, 2006; Saji and Yamagata, 2003; Vecchi and Soden, 2007). However, a substantial gap exists in the understandings of the millennial scale evolution of the Equatorial Indian Ocean paleothermocline and its global paleoclimatic interlinkages (connectivity) due to the major challenges associated with the extremely low sedimentation rates, limited sample availabilities, and intrinsic geochemical methodologies in sample processing. A limited number of paleothermocline reconstruction studies that have been carried out so far (Mohtadi et al., 2010a; Kwiatkowski et al., 2015; Rippert et al., 2015; Pang et al., 2021) where coastal boundary locations have been chosen in order to avoid sample unavailability. The near coastal locations pose a strong possibility of local climatologic perturbances in the global scale paleoclimatic assessments. All the above studies have followed the identical approach of using a single planktonic foraminifera species as the paleothermocline representative which leads to the complete underestimation of the intra-thermocline variabilities. Studies by Mohtadi et al., 2010a and Rippert et al., 2015 have used the planktonic foraminifera species *N. dutertrei* as the thermocline representative, which however, is prone to strong vertical depth migrations in the upper oceanic water column (Naidu and Malmgren, 1996; Schiebel et al., 2004). Contradicting observations regarding the deglacial thermocline temperature variability between Mohtadi et al., 2010a, and Mohtadi et al., 2010b; Rippert et al., 2015 lead to a discrepancies and inconclusive understandings regarding the Antarctic Intermediate Water contributions over the EIO region following the deglacial period. Moreover, Mohtadi et al., 2010a remained uncertain about the exact source and cause of the thermocline variations over the EEIO where the surface variations were in well association with the southern high-latitude climatic variabilities.

The inconsistencies in the earlier observations and scientific interpretations can possibly be the consequences of the unresolved intra-thermocline variabilities along with the presence of local climatic interferences and the choice of migrating planktonic foraminiferal species.

The paleosalinity reconstruction studies from the EIO paleothermocline is almost absent except the one from Mohtadi et al., 2010a, in which the explanations for the paleothermocline variabilities unfortunately remain indecisive. It clearly indicates a strong requirement for the paleosalinity reconstructions from the EIO thermocline in order to bridge the existing gap in the understandings

of the evolutions of the subsurface ocean-atmospheric and coupled climatic phenomena over the millennial time scale records.

1.10 Objectives of the Present Study

The existing limitations in the area of paleothermocline reconstructions from the EIO provided the primary motivation for carrying out a detailed paleoclimatic reconstruction study from an open EIO region using depth specific planktonic foraminifera species from the upper EIO ranging from the surface up to the lower thermocline.

The specific objectives of this study follow as:

i. Reconstruction of past sea water radiocarbon records from the upper EIO. Understanding the glacial-deglacial sea water radiocarbon variabilities. The sources and mechanisms of thermocline radiocarbon supply and the evolution of the upper oceanic paleo water mass ventilations over the EIO.
ii. Quantitative reconstruction of the EIO paleothermocline accounting for the intra-thermocline depth variabilities. Understanding the millennial scale evolution of the upper EIO thermal structure and its regional and global paleoclimatic interlinkages.
iii. Paleosalinity reconstruction from the EIO paleothermocline. Understanding the surface and sub-surface ocean-atmospheric paleo hydro-climatology.

Chapter 2

Methodology

2.1 Introduction

The reconstruction of upper oceanic paleothermocline necessitates the search for a unique proxy recorder that can encapsulate the signatures of past sea water conditions from specific oceanic water depths. Planktonic foraminifers provide the only reliable proxy to achieve this goal through their wide spread distribution with in the global oceanic water column in addition to their excellent preservation potential under diverse oceanic bottom water conditions (section 1.6). The present study utilizes four different depth specific planktonic foraminifers distributed throughout the upper oceanic water column in order to understand the millennial scale evolution of different surface and subsurface ocean-atmospheric and climatic processes through the proxy reconstructions of the EIO paleothermocline. Three major proxies are investigated from the planktonic foraminiferal analyses that include the radiocarbon ($\Delta^{14}C$), the Mg/Ca and the oxygen isotopic record ($\delta^{18}O$) in order to obtain the paleosalinity.

The present chapter discusses the complete methodological aspects undertaken in order to achieve the goal. The choice of an appropriate sediment core, the regional oceanographic setting and the sample techniques are discussed in the preliminary section followed by detailed discussions about the sediment processing and extraction of foraminifers. The subsequent sections discuss the sample treatment procedures, the working principle of the instruments and the analytical approaches followed in order to obtain the quality and high precise datasets.

2.2 Study Location and Oceanographic Settings

The location of this study is situated in the western central EIO within a small basin around 300 km south of the transect zone between the Bao-Chuan fracture zone and the Carlsberg ridge. A westward flowing South Equatorial Current (SEC), an eastward flowing Monsoon Current and a strong western boundary Somali Current (SC) (Divakar Naidu and Malmgren, 1999) predominate during the South-West Monsoon (SWM) season. The North-East Monsoon (NEM) current flows westward across the basin, carrying the fresher Bay of Bengal (BoB) water into the studied region (Schott et al., 2009). The thermocline water in this region is supplied dominantly by SAMW-AAIW (SubAntarctic Mode water-Antarctic Intermediate Water) with a minor contribution from the Indonesian Through Flow (ITF) (You, 1998) (Fig. 2.1). However, the ITF signal gets intensely mixed as it crosses through various sills in the Indonesian Sea before reaching into the present studied region (Winfree et al., 1970).

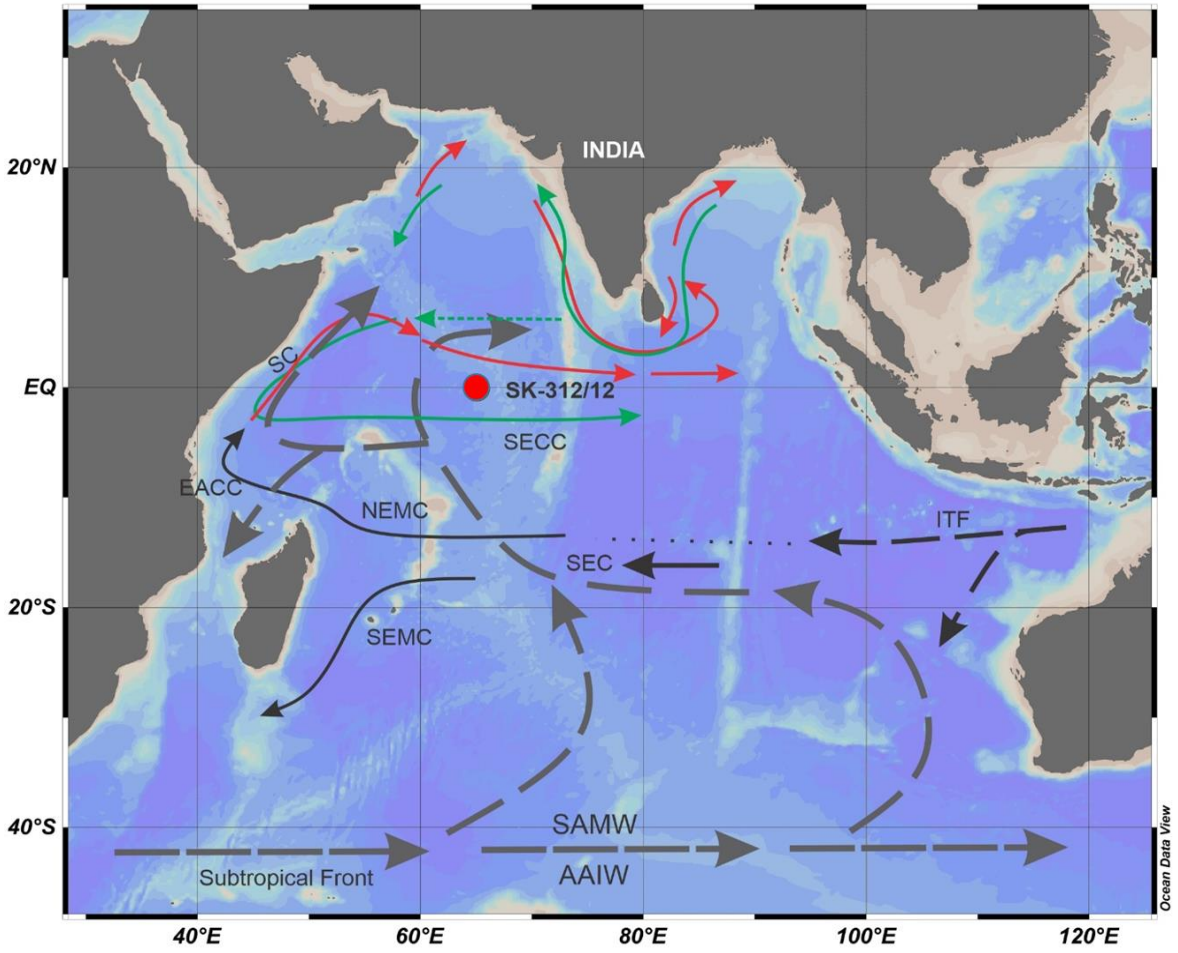

Figure 2.1: Simplified representation of surface (solid lines) and thermocline (dashed lines) water circulations (modified after Schott et al., 2009 and You, 1998 respectively) over EIO at core SK-312/12 (0.0068°N,65.0048°E) (red dot). SC- Somali Current, SECC- South Equatorial Counter Current, EACC- East African Coastal Current, SEC- South Equatorial Current, NEMC- North East Madagascar Current, SEMC- South East Madagascar Current, ITF- Indonesian Through Flow, SAMW- SubAntarctic Mode Water and AAIW- Antarctic Intermediate Water. The red and green solid lines represent the surface ocean circulations during the south-west monsoon and the north-east monsoon periods respectively.

2.3 Sample Collection and Processing

2.3.1 Sample Collection

Sediment core SK-312/12 is located at 0.0068°N and 65.0048°E, at a water depth of 3750m, (Fig. 2.1) which is well above the regional Calcite Compensation Depth (CCD) which lies below ~4700m (Van Andel, 1975). The core was collected during the GEOTRACES cruise ORV Sagar Kanya in May, 2014, using a gravity corer (Fig. 2.2a) with contamination-free PVC pipe. The sediment core was stored at low temperature and brought to the laboratory for further processing. The PVC pipe was cut using a cutter device and cleaned properly through wet tissues to remove the PVC remnants. A thin outer sediment layer was also removed from the sediment core in order to avoid any possible surficial cross sediment contamination. The core was then sub-sampled at 1cm intervals and stored in separate polythene zip-lock bags (Fig. 2.2b).

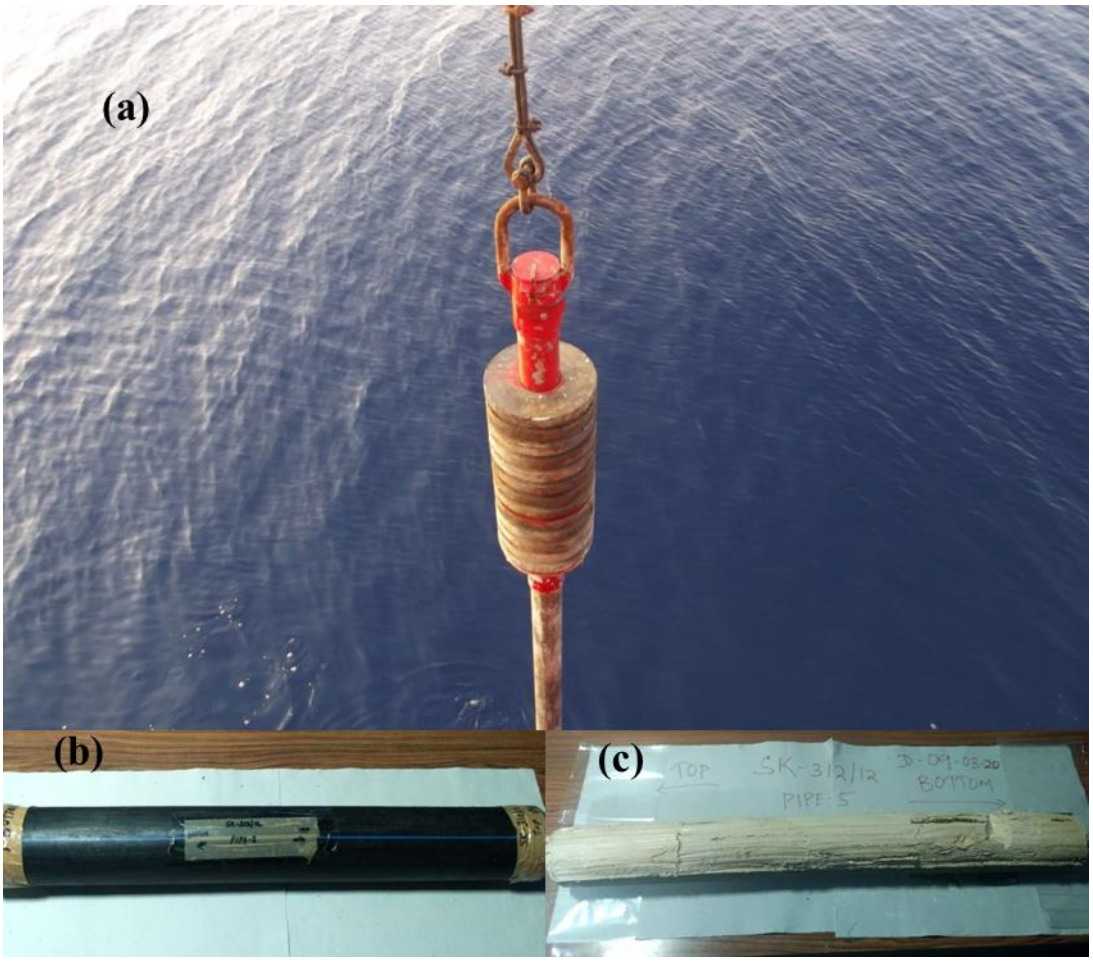

Figure 2.2: (a) Lowering of sediment corer (credit: M. Murugunantham), (b) Sealed core pipes after sub-cutting and (c) Sediment core pre-conditioned for sub-sampling

Kanya in May, 2014, using a gravity corer (Fig. 2.2a) with contamination-free PVC pipe. The sediment core was stored at low temperature and brought to the laboratory for further processing. The PVC pipe was cut using a cutter device and cleaned well through wet tissues to remove the PVC remnants. A thin outer sediment layer is also removed from the sediment core in order to avoid any possible surficial cross sediment contamination. The core was then sub-sampled at 1cm interval and stored in separate polythene zip-lock bags (Fig. 2.2b).

2.3.2 Processing of Sediments

Around 30-40g of bulk sediment from alternate sections were taken in individual cleaned boro-silicate beaker and oven dried at ~45°C until complete drying. The net sample weights before and after drying were noted. It was noticed that the sample weights were reduced to ~20g on average after complete drying. Around 5g of dried sediments were kept for sediment geochemical analysis purposes. The rest of the dried sediments were undertaken for foraminiferal geochemical analyses. The taken sediments were dissolved in a 200ml ultrapure water (Milli-Q (MQ)) solution added with a 10ml of hydrogen peroxide (50%, Emplura, for organic removal) and a 10ml of sodium hexa-metaphosphate (10%, w/V, for clay removal) reagents. The solutions were stirred

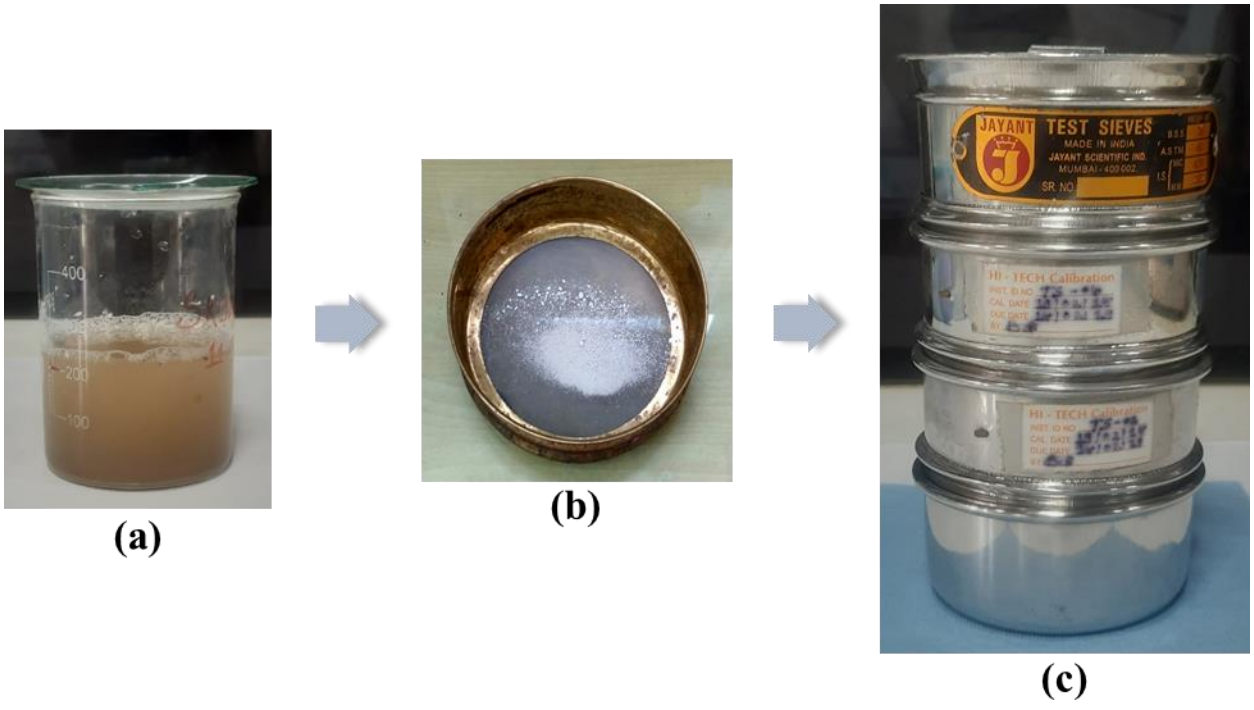

Figure 2.3: (a) Bulk sediment processing, (b) Separation of foraminifers and (c) Sieving through specific size fractions.

intermittently and kept under reaction for 24hrs (Fig. 2.3a). The solutions were further ultra-sonicated and sieved through 63µm sized sieve set. Remaining foraminifers were cleaned using MQ-water (Fig. 2.3b), collected in beakers and kept in oven at ~45°C for complete drying. The dried foraminifers were then sieved through specific size ranges of 150µm, 250µm, 355µm and 425µm (Fig. 2.3c) and finally collected into separate PP vials.

2.4 Identification and Extraction of Species-Specific Planktonic Foraminifers

Four different depth specific planktonic foraminifers with preferable depth habitats extending respectively from the surface ocean up to the lower thermocline were identified under the microscope (Fig. 2.4) based on the individual characteristic morphologies (section 1.5). The individual species chosen are *G. ruber*, *T. sacculifer*, *G. siphonifera* (Type I) and *G. menardii* with characteristic individual depths of surface ocean, lower

Figure 2.4: Identification and shell picking under microscope.

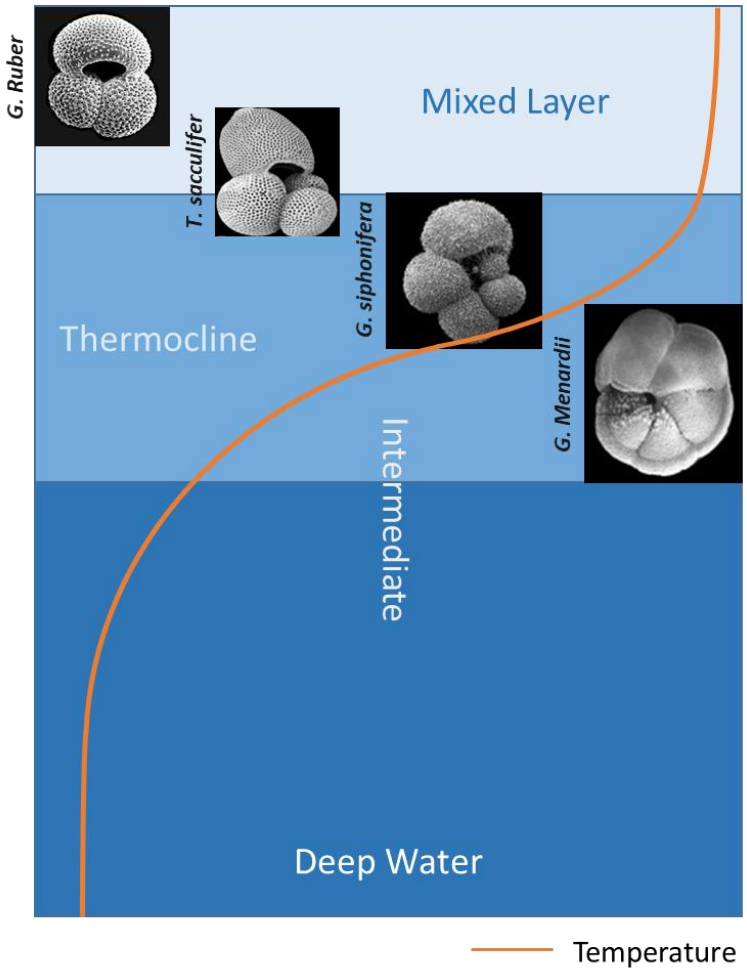

Figure 2.5: Schematic of depth specific distributions of G. ruber (surface ocean), T. sacculifer (lower ML), G. siphonifera (upper thermocline) and G. menardii (lower thermocline).

mixed layer, upper thermocline and lower thermocline respectively (Fig. 2.5). For radiocarbon reconstuctions *G. ruber* and *T. sacculifer* were combinedly chosen as the ML and *G. menardii* was chosen as the thermocline representatives. The size range of shells were kept between 250-425µm for radiocarbon dating. For Mg/Ca and stable isotopic records *G. ruber* (s.s.), *T. saculifer* (w/s), *G. siphonifera* (Type I) were chosen from 250-355µm size fractions whereas *G. menardii* was chosen from 355-425µm size range (Fig. 2.5).

2.5 Radiocarbon Dating

All the samples are graphitised into pure carbon prior to radiocarbon dating using the Accelerator Mass Spectrometer (AMS) facility at Physical Research Laboratory (PRL), Ahmedabad (Fig. 2.7). During the process of graphitization, the CO_2 gas released from organic or inorganic sample gets converted into graphite in the presence of hydrogen and iron (Němec et al., 2010; Wacker et al., 2010).

2.5.1 Graphitisation

Around 10 mg of cleaned and well preserved planktonic foraminifers were picked up from each dating section under microscope from 250-425µm size fraction for graphitization and radiocarbon dating. *G. ruber* (s.s.) and *T. sacculifer* in sub equal amounts, and *G. menardii* were chosen from the mixed layer and thermocline water mass respectively.

The inorganic carbonates (samples and the international intercomparison inorganic carbonate reference standards (with ~1mg carbon)) were graphitised using the Carbonate Handling System (CHS) (Fig. 2.6) coupled with the graphitisation unit. The carbonate samples were placed in 12ml glass tubes in the CHS (Wacker et al., 2013). The vials were closed with screw tight caps containing butyl septums. The overhead atmospheric gas present within the vials was removed by flushing under a constant flow of helium gas for 10 minutes of durations. 0.3ml of phosphoric acid (grade) was added to the samples using a gas-tight syringe, and left under heating at 85°C for one hour of duration to ensure complete decomposition of the carbonates and release of sample CO_2 gas. The gaseous CO_2 released was then transferred into the Automated Graphitization Equipment (AGE) graphitisation unit via helium flow as the carrier. Additional moisture present along with the CO_2 analytes were removed by the phosphorus pentoxide water trap. A similar process was also followed to graphitize the carbonate reference standards too.

International intercomparison organic carbon standards were graphitised using the Elemental Analyser (EA) (Fig. 2.6) unit coupled with the graphitisation system, to be used as reference standards during the radiocarbon measurement in AMS. Adequate sample amounts (with ~1mg of organic carbon) were packed in tin foils and put into an autosampler of Elementar Vario MICRO cube Elemental Analyser (EA). The samples were combusted at 950^{O}C under the presence of oxygen to liberate CO_2 which was further transferred into the AGE graphitization unit through the helium flow acting as the carrier gas. Excess of oxygen was removed in the reduction column filled with copper. The reduction column also converts NO_x to N_2 as well. Additional moisture contents were removed by the phosphorus pentoxide water trap. The individual gases resulting as the product phases of combustion (mostly N_2, CO_2, and minimal H_2O) were separated and further detected under the thermal conductivity detector before they leave the EA. In the end, the sample CO_2 got trapped in the zeolite trap of the AGE unit where CO_2 was absorbed and N_2 and H_2O got removed.

The sample CO_2 produced either from the CHS or EA unit were passed through the Zeolite trap for adsorption. Once the loading of the sample CO_2 was complete, the zeolite trap was heated to

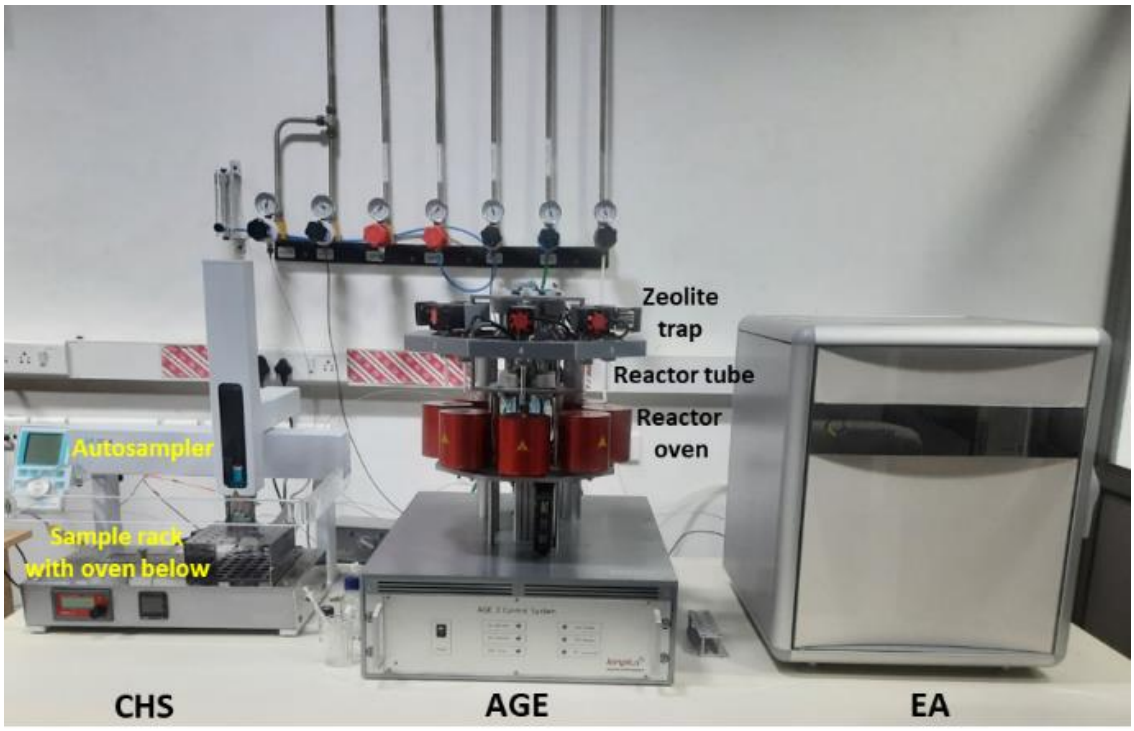

Figure 2.6: Automated Graphitization Equipment (AGE) coupled with Carbonate Handling System (CHS) and Elemental Analyser (EA).

500°C in order to remove the sample CO_2 into the individual quartz reactor tubes in the graphitisation system (AGE 3). The trap was cleaned prior to every sample loading through constant helium flushing. The quartz reactor tubes were mounted vertically to allow fast mixing of the reacting gases. Individual reactor tubes were pre-filled with 5-6mg of iron (Fe) that acted as a catalyst during the process of graphitization. Prior to the sample CO_2 loading, the iron catalyst was pre-conditioned through heating (at 550°C) followed by a subsequent reduction with pure hydrogen in order to remove the possible existences of the carbon contaminant phases. Hydrogen was added into the individual reactor tubes maintaining a H_2/CO_2 ratio of 2.3 which is considered to be the optimal condition for graphitisation under a given temperature of 580°C (Wacker et al., 2010). The reactor tubes were placed above individual electric reactor ovens (Fig. 2.6) that provide the pre-requisite temperature conditions for graphitisation.

The process of graphitization can be represented in a simple manner of a single Bosch reaction as:

$$CO_2 + 2H_2 = C + H_2O$$

The actual process of graphitisation is complex with multiple ongoing reactions going on between the CO_2 gas, iron and hydrogen (Němec et al., 2010). However, the complete process can be briefly summarised as;

The iron reduces the CO_2 resulting in the formation of Fe_3O_4 which is again reduced back to Fe by hydrogen. The reduced Fe acts as a catalyst in the following processes of graphitization. The continuous conversion of CO_2 into graphite results in a constant decrease in pressure inside the reactor tubes. Finally, the iron gets coated with the graphite produced through the graphitisation reactions. The Peltier thermoelectric coolers ensure the freezing and removal of any water/moisture produced through the process of graphitization. The graphitised samples are pressed into aluminium sample holder targets with copper pins and taken for measurement in the AMS facility located at PRL, Ahmedabad (Bhushan et al., 2019b; 2019a).

2.5.2 Radiocarbon Measurement using AMS

Working Principles of AMS: The radiocarbon measurement of graphitised samples were carried out using the 1MeV tandem accelerator mass spectrometer established at Physical Research Laboratory, Ahmedabad. The 1 MV AMS was procured from HVEE (High Voltage Engineering

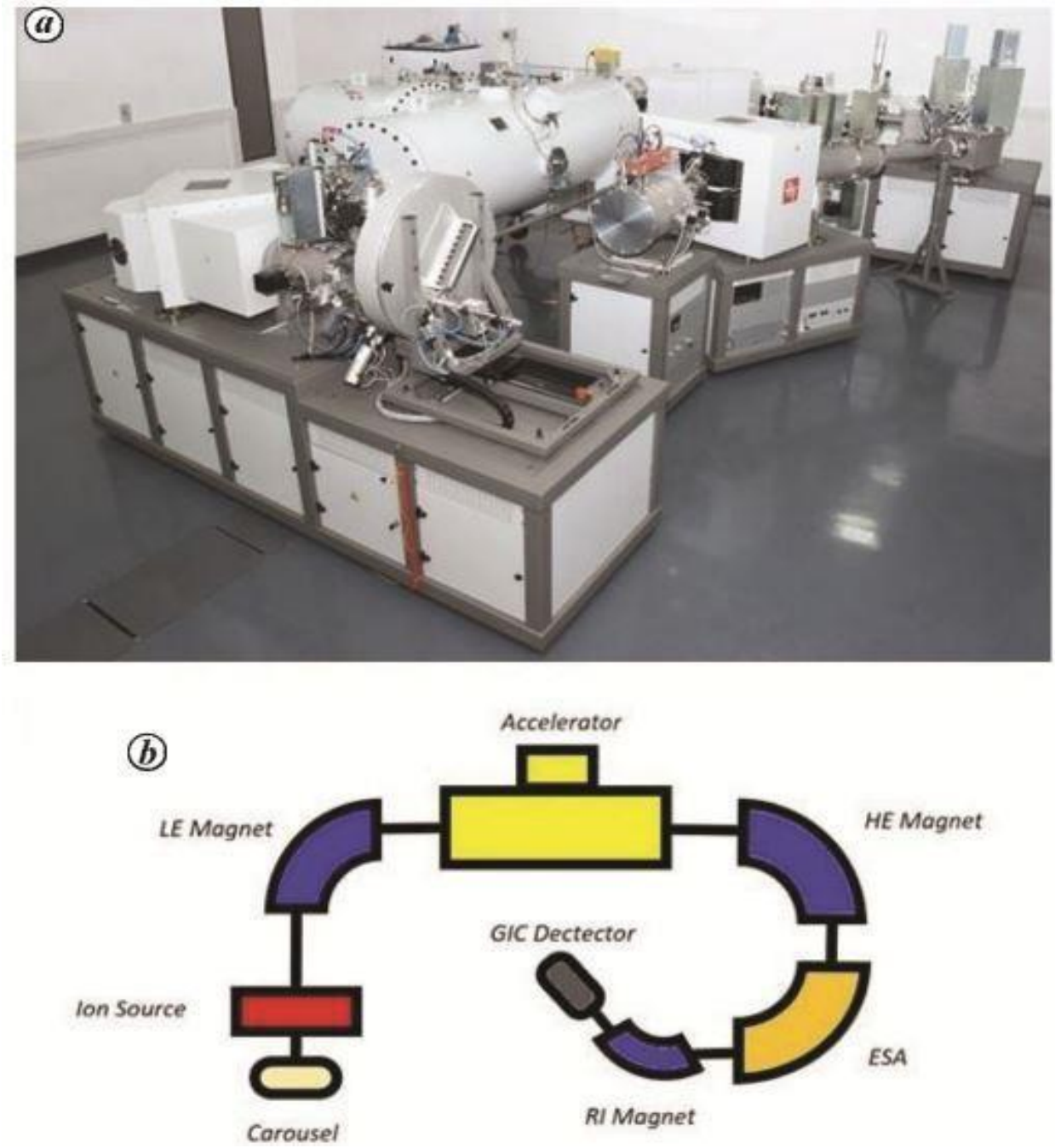

Figure 2.7: (a) Photograph of 1 MV Accelerator Mass Spectrometer (AMS) facility (PRL-AURiS) installed at PRL, Ahmedabad. (b) A schematic of major working units of AMS (Bhushan et al., 2019b).

Europa, BV, Netherlands) (Klein et al., 2006) and has been named as Accelerator Unit for Radio-isotope Studies (AURiS) unit at PRL (PRL-AURiS). The PRL-AURiS comprises of several major constituting parts such as: Negative ion source, low-energy (LE) bouncer-injector magnet, 1MV tandetron accelerator, high-energy (HE) magnet, electrostatic analyser (ESA), rare isotope (RI) magnet, and gas ionisation chamber (GIC) detector (Fig. 2.7).

The ion source (SO-110) can accommodate 50 sample targets in the carousel unit for one single batch of measurements. It uses Cesium (Cs) for sputtering the target material to produce negative ions through a process called sputtering. During this process, Cs stored in the reservoir is heated up to 110°C to produce Cs vapour under an ionisation potential of 7KeV between the target and ionizer. The Cs^+ ions generated get bombarded on to the sample target with high velocity producing –ve sample ions through sputtering. The negative sample ions are accelerated by the target voltage in the direction of the ionizer passing through its central aperture. The ions are further accelerated towards the extraction cone by providing an additional 28KeV of extraction voltage between the cone and the ioniser. The ion beam is then passed through the Bouncer-Injector (BI) magnet that allows the sequential introduction of different isotopes of interest into the 1MV Tandetron accelerator unit. This process is called Bouncing. Suitable DC voltages are applied between the ion source and the 120º BI magnet (radius 455mm), to regulate the energies of incoming individual negative ions into the channelled path within the BI magnet under a constant magnetic field. The DC pulses (at ~100Hz) are associated with blanking unit (fast switching steerer) located between the injector magnet and the accelerator which provides settling time to the bouncing voltages that helps in reducing uncertainty arising from the beam instabilities (Klein et al., 2004). Based on the durations of the bouncer settings of respective pulses, the abundant isotopes are injected for a shorter time compared to the rarer ones. The low-energy magnet thus helps in first phase separation of the targeted rare isotopic mass equivalents from the residual counterparts.

The Tandetron accelerator strongly attracts the –ve ions coming out of the LE magnet towards its centre present at an extremely high positive potential of 1MeV. As the –ve ions approach the high energy positive terminal of the accelerator they collide strongly with Argon, present as the stripper gas inside. The process thus breaks down the molecular bonds resulting in the production of positive elemental ions. The positive elemental ions are strongly repelled by the high energy

positive potential of the accelerator and thus leave at the opposite end into the High Energy Magnetic detector. The emerging positive ionic beams are analysed by a 90º High Energy (HE) magnet (radius 850mm), which directs the abundant stable isotope(s) into the offset Faraday cup(s) that measures the individual ratios through current conversions. The rare isotope beam is streamlined into a 120º ESA (radius 650 mm) for signal filtering after which it enters into a Rare Isotope (RI, radius 850 mm) magnet for removing the unwanted ions and helping reduce the background measurement values. The ions finally enter a detector consisting of a dual anode GIC filled with isobutene gas. Individual ions collide with the iso-butane gas releasing strong energy pulses which are efficiently detected as individual sample counts. The target rare isotopic counts are identified based on its characteristic residual energy (E_{final}) vs. energy loss (ΔE) spectrum.

Radiocarbon Measurement: For radiocarbon measurements, C^- ion is introduced into the LE magnet from the ion source. Individual isotopes of carbon (^{12}C, ^{13}C and ^{14}C) are sequentially injected into the 1 MV accelerator through BI magnet. Various charge states of carbon ions are produced inside the accelerator through stripping. A +2 charge state of ^{14}C ($^{14}C^{2+}$) is chosen since it provided higher stripping efficiency at 1MeV under a 44% transmission (Bhushan et al., 2019b; Raj, 2020). After their passages through the HE magnet, the ^{12}C and ^{13}C were measured in the faraday cups while the ^{14}C beam is carried forward into the ESA and RI magnet to reach the GIC detector. Ions like $^{7}Li^{+}$, with a similar mass/charge ratio as that of $^{14}C^{2+}$ also reach the detector producing possible signal interference. However, these interferences are efficiently removed based on the typical E_{res} and ΔE spectrums of ^{14}C along with an added fine-tuning of the instrument helping reduce the possible interferences significantly. The PRL-AURiS is capable of measuring a $^{14}C/^{12}C$ ratio up to the order of magnitude of 3.9×10^{-16}. Routine measurements have been carried out through simultaneous measurement of multiple international inter-comparison standards and blanks along with the samples. Oxalic Acid-II (Ox-II) has been used as the primary reference standard, and Anthracite as blank. Multiple radiocarbon reference materials (IAEAC1, IAEA-C2, FIRI-E, VIRI-R and VIRI-U) have been routinely measured to check the efficiency of sample graphitisation unit and the isotopic measurement in AMS (Rozanski et al., 1992; Boaretto et al., 2002; Scott et al., 2010) (Fig. 2.8 and Table 2.1) from time to time.

Table 2.1: Measurement results of different radiocarbon reference standards.

Reference Material	Parameter	Consensus Value	Measured Value*	Deviation from the consensus value (%)	Precision (% RSD)
FIRI-E	Libby age (yrs BP)	11780±7	11562±32	1.85	0.27
VIRI-R	pMC	73.34	72.68±0.61	0.9	0.84
VIRI-U	pMC	23.08	23.06±0.34	0.07	1.48
IAEA-C2	pMC	41.14	41.63±0.04	1.19	0.1

*Indicates the mean value of multiple measurements.

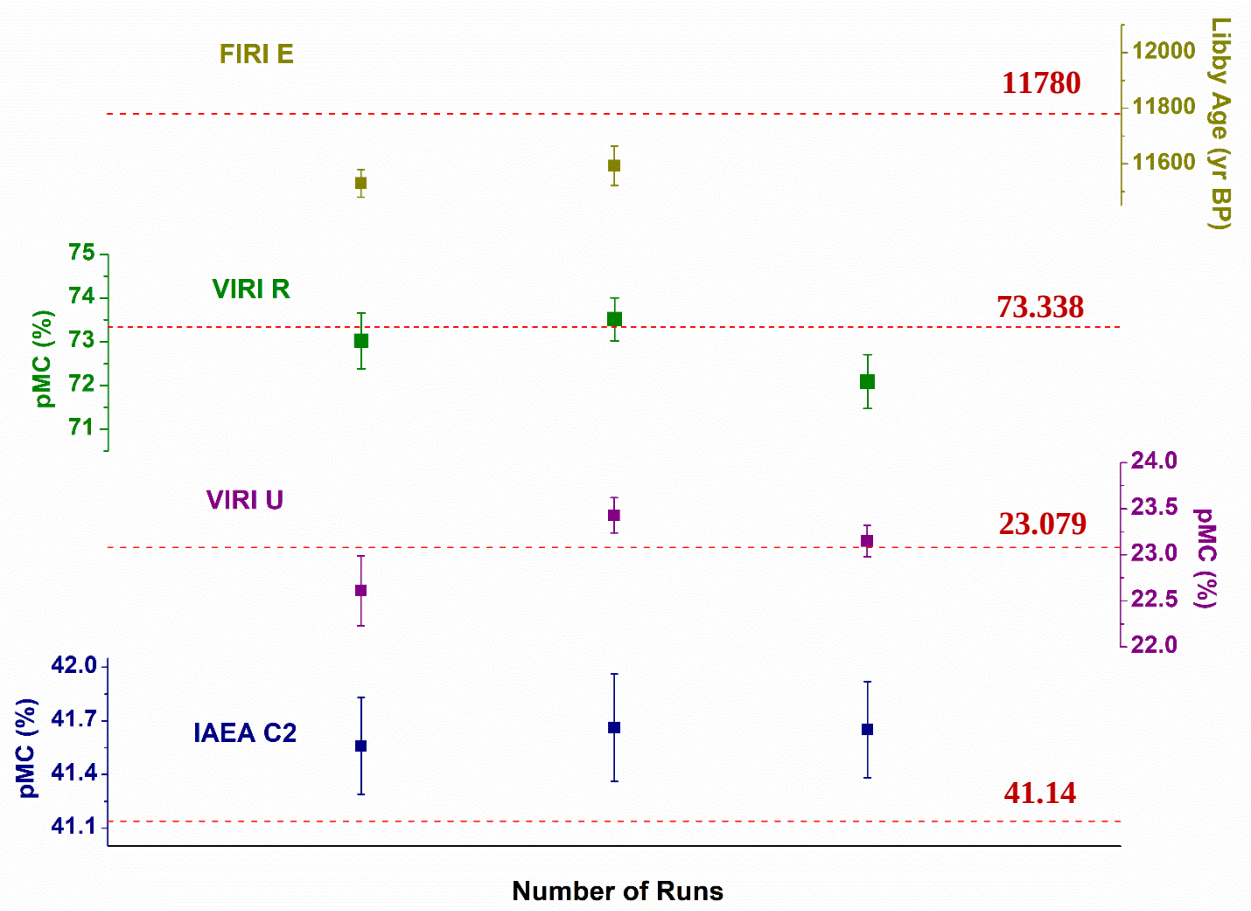

Figure 2.8: Comparison of radiocarbon parameters of reference standards measured by PRL-AURiS with the respective consensus values (red dotted lines and values).

2.5.3 Chronology

Radiocarbon ages of SK-312/12 were obtained for the mixed layer and thermocline, and then normalized and corrected for isotopic fractionation as per standard method (Stuiver and Polach, 1977; Stuiver et al., 1998). The radiocarbon ages of the mixed layer were further calibrated with respect to the MARINE20 Calibration curve (Heaton et al., 2020) with a modern reservoir age (ΔR) of -54 ± 65 yr (Dutta et al., 2001; Southon et al., 2002) under the R package "Bacon" (Blaauw and Christeny, 2011), that uses the CALIB 8.2 method by Stuiver et al., 2021, and the Bayesian calendar age chronology was obtained. The sedimentation rate of this core varies between 1.1–3.5 cm/ka with an average sedimentation rate of ~ 1.9 cm/ka (Fig. 2.9). The sedimentation rates increased during the Heinrich Stadial events (H2 and H3, around ~24 ka and ~31 ka respectively) which could be a result of increased sediment deposition over the EIO associated with the southward shift of ITCZ and strengthening of north-east monsoons (Godad et al., 2022; Haridas et al., 2022) due to increased global climatic cooling.

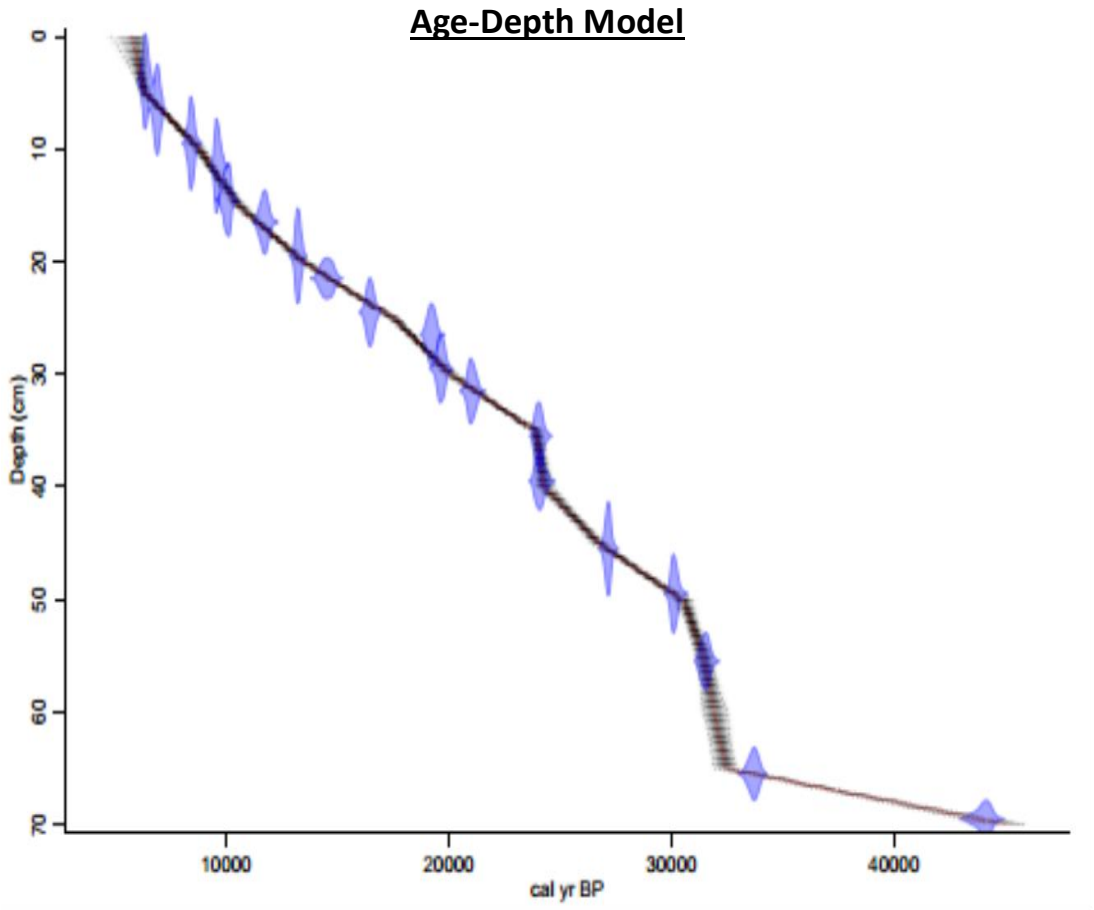

Figure 2.9: Bayesian age-depth model of sediment core SK-312/12.

2.6 Trace Elemental Cleaning and Mg/Ca Analysis

The foraminiferal samples are required to undergo the trace elemental (TE) cleaning procedure prior to the Mg/Ca analysis of the sample carbonates (Barker et al., 2003) in order to remove the associated sediment contaminant phases like clay, organics and the secondary adsorbed particles.

2.6.1 Trace Elemental Cleaning and Preparation of Analytical Solution

Unfragmented shells of all the four planktonic foraminifera species were chosen for trace elemental cleaning prior to the Mg/Ca analysis. A first phase of sample treatment was carried out following the trace elemental cleaning protocol established by Barker et al., 2003 for foraminiferal Mg/Ca analysis. However, after the first phase (Phase I) of sample treatment and analysis, extremely limited concentrations of Mg and Ca were detected for *G. ruber* (s.s.) and *G. siphonifera* with anomalously lower Mg/Ca values caused by possible excessive loss during the weak-acid leach treatment (Detailed descriptions of the associated approach are discussed in the following sections). Retreatment of samples and analyses (Phase II) were thus carried out for *G. ruber* (s.s.) and *G. siphonifera* following necessary modifications in the methodological approach. Around 300-350µg of *G. ruber* (s.s.), *T. sacculifer* (w/s) and *G. siphonifera*, and around 350-400µg of *G. menardii* shells were taken for the first phase of sample treatment and analyses. *G. ruber* (s.s.) and *T. sacculifer* (w/s) were chosen from the 250-355µm shell size fraction whereas, *G. siphonifera* and *G. menardii* were chosen from the 350-425µm size fractions respectively. Following is the general descriptions of the Trace Elemental (TE) cleaning and sample preparation method followed prior to the first phase of Mg/Ca analysis of SK-312/12 planktonic foraminifers (Table 2.2).

Table 2.2: Step Wise Procedures for Trace Elemental Cleaning (Phase I).

Process of Cleaning	**For *G. ruber, T. sacculifer* and *G. siphonifera***	**For *G. menardii***
Clay Removal (with MQ)	500-750µl	500-750µl
Ultrasonication (duration)	90sec	120sec
No. of repeat	4-5	4-5
Clay Removal (with Methanol)	250µl	250µl
Ultrasonication (duration)	90sec	120sec
No. of repeat	2	2
Organic Removal (with 1% Alkali buffered H_2O_2)	250µl	250µl
Duration	10min	10min
No. of repeat	2	2
Weak acid leach (with 0.001M HNO_3)	250µl	250µl
Duration	20-25sec	30sec

2.6.1.1 Breaking and Homogenization of Foraminiferal Shells

The foraminifera samples were placed over a cleaned glass plate using a thin brush. The glass plate was already put over a white butter paper for clear visualization of the sample under the microscope. The lower plate was slightly held up using the left arm. A second cleaned glass plate was pressed gently and dragged a bit to ensure complete breaking open of all the individual chambers of each foraminiferal shell. The purpose is to allow the release of any chamber fill material present inside the shells, during the subsequent cleaning stages. Any possible larger silicate grains or visible dark contaminant phase were removed from the crushed sample fraction using a thin synthetic brush (Fig. 2.10a). The crushed shells were transferred into cleaned micro-centrifuge tubes (1.5ml, PP material) filled with ~0.5ml of MQ-water and gently stirred using a cleaned thin synthetic brush for homogenization (Fig. 2.10b).

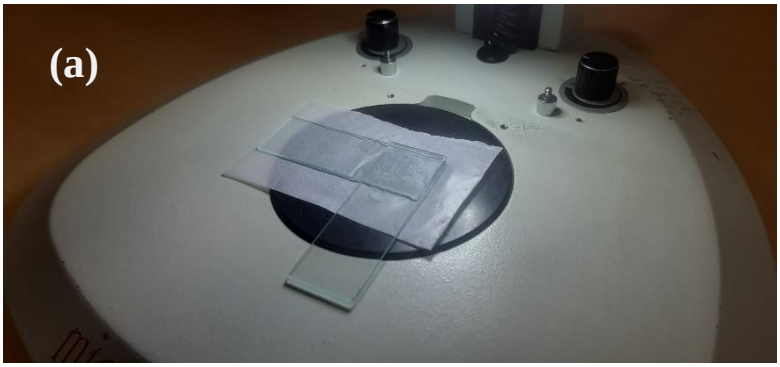

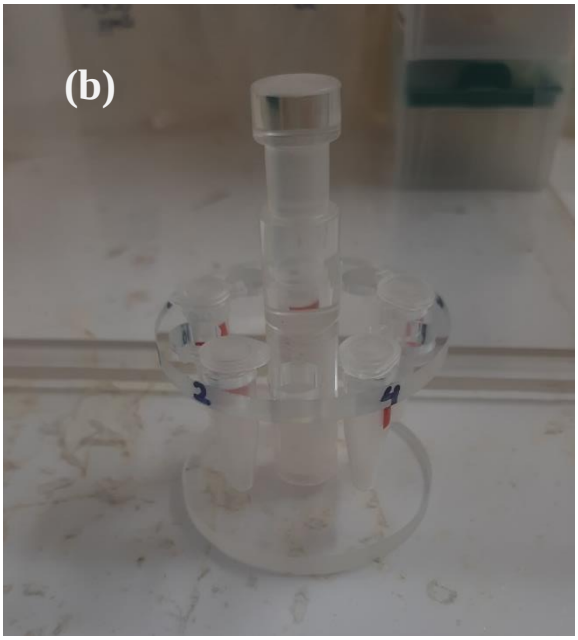

Figure 2.10: (a) Breaking of foraminifera shells under microscope. (b) Homogenised samples within micro-centrifuge tubes.

To avoid any contamination, the glass plates used were thoroughly cleaned by soaking under 1M HNO_3 (EMPARTA, 69%) solution for 24hrs followed by an equivalent period of soaking in MQ-water. The glass plates were then cleaned thoroughly under MQ-water jet and allowed to dry properly. The micro-centrifuge tubes were pre-cleaned by soaking within 1M HNO_3 solution for 24hrs at 75-80°C, followed by an equivalent period of soaking under heat within MQ-water.

Individual centrifuge tubes were then cleaned thoroughly by rinsing thrice under MQ-water jet and allowed to dry completely prior to their use for foraminiferal sample transfer.

5 samples were taken in a sample rack for one batch of TE cleaning. Separate pipette tips were used for individual samples in order to add and remove reagents during subsequent cleaning steps.

2.6.1.2 Clay Removal

The sample solutions were pipetted using individual pipette tips. Overlying supernatant MQ-water solutions were removed from each sample after allowing for complete settling of the carbonate shells.

(i) The samples were ultrasonicated for 1.5-2 minutes (90secs for *G. ruber* (s.s.), *T. sacculifer* (w/s) and *G. siphonifera*, and 120secs for *G. menardii*) (Fig. 2.11) and the rack was taken back. Individual samples were agitated by pipetting in ~500-750µl of MQ-water into each micro-centrifuge tube. The side walls were sprayed a little to bring the possible pipetted out carbonates back into the solution. The agitation helps bring the loose clays into suspension. The samples were allowed to settle under minimal settling technique, where the distinct carbonate grains sufficiently settle down within a few seconds leaving the unwanted silicate particles in suspension with a visibly milky appearance. The overlying solutions were removed from individual sample tubes. Around 15µl of MQ-water solution was always left behind during every step of reagent removal in order to avoid sample loss during successive steps of sample treatments.

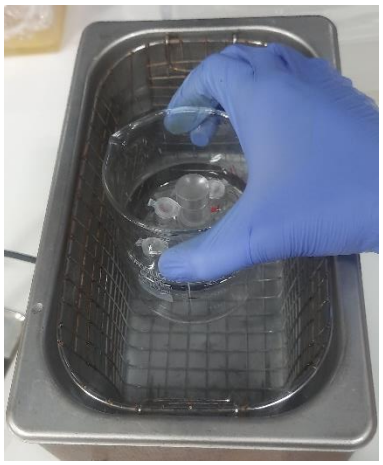

Figure 2.11: Ultrasonication of foraminifera samples during the process of clay removal.

Step (i) was repeated 4-5 times until the solutions appear distinctly clear following ultrasonication and agitation.

(ii) 250µl of Aristar methanol was pipetted into each sample tube, ultrasonicated for durations similar to step (i). The overlying methanol solution was lifted off and pipetted back to agitate the sample solutions bringing the clays into suspension. The carbonate particles were allowed to settle and the overlying methanol was removed (Fig. 2.12).

Step (ii) was repeated.

(iii) 500-750µl of MQ-water was pipetted into each sample tube and removed after allowing the distinct carbonate shells to settle.

This step was carried out in order to remove any remaining methanol from the sample solution.

Figure 2.12: Clay removal using Methanol.

2.6.1.3 Removal of Organic Matter

This step was purposed for removing possible organic content from the carbonate samples. An alkali buffered 1% H_2O_2 (Hydrogen Peroxide) solution was prepared by adding 50µl of H_2O_2 (Aristar grade) to 5ml of 0.1M NaOH (Sodium Hydroxide, Aristar grade) prior to each set of (5 samples in one set) organic removal treatment.

(iii) 250µl of alkali buffered 1% H_2O_2 solution was added to each sample tube and put in the rack. The sample rack was placed inside boiling water condition (at 100°C) for 10 minutes (Fig. 2.13). The samples along with the rack were removed at 2.5 and 7.5 minutes, tapped on the bench top to release possible gaseous build up, and immediately put back into the boiling water. At 5 minutes' duration, the samples were ultrasonicated for a few seconds, tapped on the bench and put back inside the boiling water. The aim of these interim steps was to maintain contact between the reagent and the sample. After completion of 10 minutes, the oxidizing reagents were removed from the individual sample tubes.

The step (iii) was repeated.

(iv) Any remaining oxidizing reagents were removed by filling the tube with MQ-water and removing it after settling of the sample matter.

Step (iv) was also repeated for the second time.

Figure 2.13: Organic removal treatment.

2.6.1.4 Removal of Coarse-Grained Silicates

Removal of coarse grained silicates along and possible dark contaminant phases were already done during the process of sample crushing and homogenization. However, all the samples were rechecked to ensure the removal of any remaining particulate contaminant phase and the possible entrance of any foreign body during the previous cleaning steps.

(v) The samples were transferred into micro-beakers using MQ water and excess overlying solutions were removed. Possible silicate and non-carbonate particles were removed using fine brush. The samples were transferred back into the respective micro-centrifuge tubes using fine brush as outlined in section: 2.6.1.1.

2.6.1.5 Weak Acid Leach

A 0.001M HNO_3 (Suprapur grade) solution was prepared for weak acid leach treatment. This step is performed in order to ensure the removal of any adsorbed contaminants from the carbonate test fragments.

(vi) 250µl of 0.001M HON_3 solution was added to each sample and ultrasonicated. The duration of ultrasonication was kept around 20-25 secs for *G. ruber* (s.s.), *T. sacculifer* (w/s) and *G. siphonifera*, and around 30 secs for *G. menardii* because of its higher durability. The acid solution was immediately removed after the settling of carbonate particles.

(vii) MQ-water was immediately pipetted into each sample tube in order to prevent excess dissolution. The overlying MQ-water was removed using individual pipette tips.

Step (vii) was repeated leaving around 15µl of remaining sample solution.

Remaining solution was almost removed using 10µl pipette with a very careful manner, without disturbing the settled cleaned carbonate samples.

2.6.1.6 Sample Dissolution

Sample dissolution is performed using a 0.075M HNO_3 (Suprapur grade) solution ensuring non incorporation of any possible non-carbonate material that may still be present in the sample.

(viii) 500µl of 0.075M HNO_3 solution was added to each sample and was subjected to ultrasonication. The samples were gently flicked from below intermittently to allow escape of possible CO_2 gas build-up. Ultrasonication was stopped as soon as CO_2 build-up ceased in all the samples. The sample rack was removed out of the ultrasonication bath. Samples were left overnight to ensure complete dissolution of any remaining carbonate phases.

2.6.1.7 Preparation of Final Sample Solution for ICP-OES Measurements

15ml centrifuge tubes were cleaned by soaking overnight with 2M HNO_3 solution followed by a soaking with MQ-water for an equivalent time duration. The tubes were rinsed thrice with MQ-water and allowed to dry completely. The dissolved samples were transferred into individual 15ml centrifuge tubes using the respective pipette tips. A 0.4M HNO_3 (Suprapur grade) solution was prepared and added to each sample making a final volume of 10ml. All the samples were centrifuged for a few minutes and left overnight to ensure complete homogenization prior to analyses (Fig. 2.14).

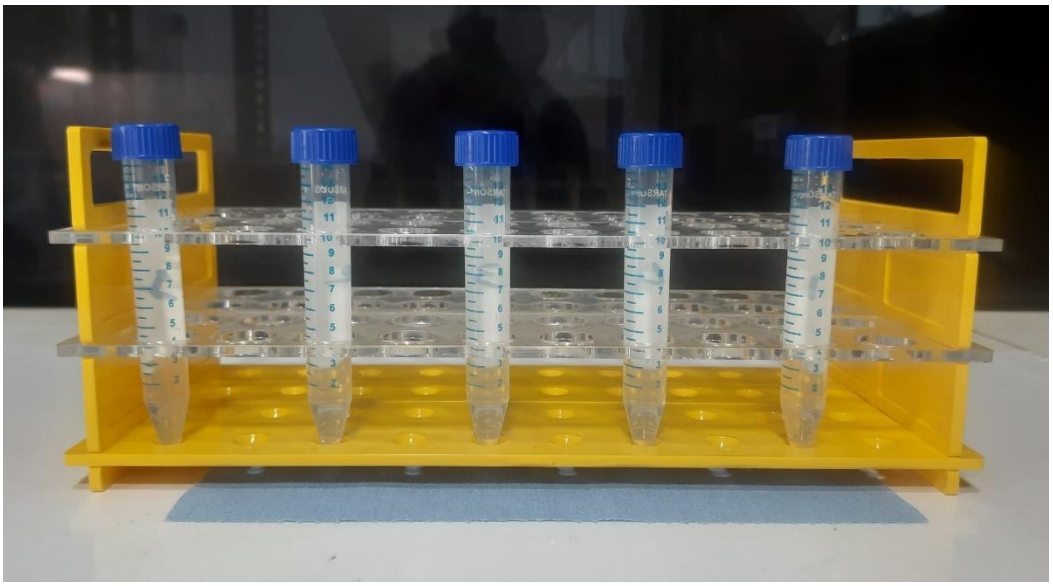

Figure 2.14: Final sample solution after TE cleaning and dissolution for ICP-OES measurements.

2.6.2 Mg/Ca Analysis

The Mg/Ca analyses was done using Thermo Scientific iCAP 7000 Plus series Inductively Coupled Plasma Optical Emission Spectrometer (ICP-OES) facility established at PRL, Ahmedabad (Fig. 2.15).

Figure 2.15: ICP-OES facility at PRL, Ahmedabad.

Working Principle of ICP-OES: The primary components of an ICP-OES consists of a sample injection system, plasma torch, radiofrequency power generator, an echelle optical design, and a charge injection device (CID) solid-state detector. In ICP-OES samples are injected in liquid form through an auto-sampler. One sample is analyzed at a time before proceeding to the next sample injection. After injection, the samples are pumped through a nebulizer that produces a fine spray of the sample. The larger droplets are removed to the drain, and the fine aerosols are passed into the plasma through the torch assembly. The samples are then evaporated, and the residual samples decompose into constituting atoms and ions. In the plasma chamber, the sample is excited to high energy plasma state by the electrical Radio Frequency (RF) generated plasma, the temperature reaches up to 9000 K. The excited atoms/ions pass further and decay to the ground energy states releasing a set of electromagnetic wavelengths that are characteristic of the constituting elements of the particular sample solution. Individual elemental intensities are detected by the solid-state detector. The measured intensities can be converted into respective concentrations using the standard calibrations. The individual elemental concentrations can then be used to obtain the objective elemental ratios. The optic system of the ICP-OES system consists of an echelle grating and a prism. The typical orientation of prism and the echelle grating generates a two dimensional spectrum ("echellegram") consisting of a wavelength and an order separation. The specific ranges of wavelengths that can be measured in the ICP-OES lie between 166 to 847nm.

Mg/Ca Analysis: The final sample solutions prepared through trace elemental cleaning treatment of the individual planktonic foraminifers were measured for the determination of Mg/Ca ratio of the corresponding foraminiferal carbonate shells. Elemental analysis of Sr, Al, Fe and Mn were also carried out along with the Mg and Ca, in order to obtain the respective elemental ratios with respect to Ca. The elemental ratios of Al, Fe and Mn with respect to Ca are also used to substantiate the efficiency of the sample treatment procedure.

Mono-element standards of Calcium, Magnesium, Strontium, Aluminium, Iron and Manganese were used to prepare the necessary calibration standard solutions. A check standard solution of BCS-CRM 393 was also prepared by dissolving the standard powder into the common 0.4M HNO_3 (Suprapur grade) Blank solution (Greaves et al., 2005). An in-lab standard solution comprising of

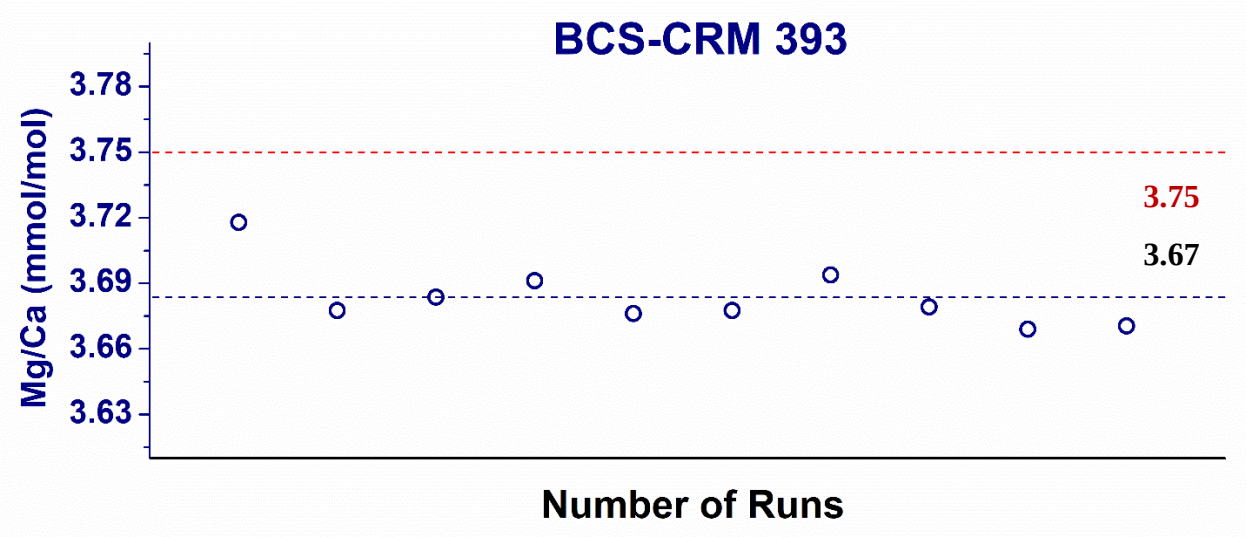

Figure 2.16: Comparison of analytical results of reference standard BCS-CRM 393 (mean of multiple runs; black) with the global consensus value (red).

all the analyte elements was also prepared and run at regular alternate intervals to correct for the instrumental drift during analysis. The analytes Ca, Mg, Sr, Al, Fe and Mn were measured at multiple wavelengths as 315.887nm and 373.69nm for Ca, 279.553nm, 280.27nm and 285.213nm for Mg, 407.771nm and 421.552nm for Sr, 237.312nm and 396.152nm for Al, 238.204nm and 259.373nm for Fe, and 257.61nm and 259.94nm for Mn. Wavelengths with better sample-blank intensity counts and without cross-elemental interferences were preferred for further calculations. The accuracy and precision of the measurement obtained from the multiple regular interval analysis of international reference standard BCS-CRM 393 is 1.77% and 0.37% (RSD) (Fig. 2.16).

Results: The Mg/Ca records obtained after the first phase of analyses were processed for quality check and cleaning efficiency. The Mg/Ca ratios obtained from the *T. sacculifer* (w/s) and *G. menardii* (Table A1) were in acceptable global ranges (Stainbank et al., 2019; Pang et al., 2020). The (Al,Fe,Mn)/Ca ratios were within acceptable ranges of <0.1mmol/mol for most of the samples. No-covariance of trace elemental ratios (Al,Fe,Mn)/Ca were observed with Mg/Ca through cross correlation indicating strong reliability of the analytical dataset. Samples with anomalously higher (Al,Fe,Mn)/Ca ratios were rejected out.

The elemental concentrations obtained from *G. ruber* (s.s.) and *G. siphonifera* however, showed an extreme loss in the final concentration of obtained Ca thus indicating excessive loss of sample carbonates during processing. This led to significantly low concentrations of Mg and Ca.

Anomalous Mg/Ca ratios were obtained in case of sample concentrations reaching up to and below the blank levels (lower than blank concentrations are identified by negative magnitudes) (Table A1) The cause of such abnormality in the elemental concentrations and ratios are primarily attributed to the significant loss of carbonates taking place during the weak acid leach treatment as inferred from visual observations. We observed that excessive loss of carbonates during acid leaching leads to selective removal of Mg over Ca resulting in subsequent reduction in the corresponding Mg/Ca ratios. Higher the degree of sample leaching, higher is the selective loss of Mg and lower is the final Mg/Ca ratio obtained from the remaining sample (Barker et al., 2003). Such abnormal reductions in the Mg/Ca ratios inevitably leads to highly inappropriate and extremely lower paleotemperature reconstruction records upon calibrations (Anand et al., 2003) (Table A2a and Table A2c).

The average core-top paleotemperature records obtained using suitable Mg/Ca vs T calibrations are compared with the present-day values in order to validate the appropriateness of the paleotemperature reconstruction records. However, no possible calibration for *G. ruber* and *G. siphonifera* could produce comparable paleotemperature records from the averaged core-top sections (within the ~±1°C error limit of calibration) due to the significantly reduced Mg/Ca records (Table A2a and Table A2c).

The sample treatment procedure for *G. ruber* (s.s.) and *G. siphonifera* thus required additional efforts for necessary modifications and reductions in the intensity of the sample treatment procedure. A 'Procedural Test' was carried out in order to assess the optimum limit of the intensity of the sample treatment procedure. The general approach for TE cleaning remained the same with necessary modifications applied to the weak acid leach and the durations of ultrasonication periods. Around 125µg of *G. ruber* (s.s.) and *G. siphonifera* were taken this time due to limitations in adequate sample availabilities. Both of the species were chosen from the 250-355µm size fractions due to complete absence of *G. siphonifera* (Type I) in the 355-425µm size fraction, taken in the first phase of analysis. The methodological modifications followed for the procedural test analysis is given in Table 2.3.

Table 2.3: 'Procedural Test' for G. ruber and G. siphonifera.

Process of Cleaning	***G. ruber* (I)**	***G. ruber* (II)**	***G. ruber* (III)**	***G. siphonifera***
Clay Removal (with MQ)	500-750µl	500-750µl	500-750µl	500-750µl
Ultrasonication (duration)	45 sec	45 sec	45 sec	40 sec
No. of repeat	3	3	3	3
Clay Removal (with Methanol)	200µl	200µl	200µl	200µl
Ultrasonication (duration)	45-30 sec	45 sec	45 sec	40 sec
No. of repeat	2	2	2	2
Organic Removal (with 1% Alkali buffered H_2O_2)	150µl	150µl	150µl	150µl
Duration	10min	10min	10min	10min
No. of repeat	2	2	2	2
Weak acid leach	✕	✓	✓	✕
Conc.	NA	0.0005M HNO_3	0.0005M HNO_3	NA
Volume	NA	250µl	175µl	NA
Duration	NA	Finger tapped 5-6 times	3-4 sec	NA

Paleotemperature reconstructions obtained for the core-top sections based on the 'Procedural Test' analysis are given in Table A3.

Table 2.4: Ca concentrations of the final sample solution obtained from type 'G. ruber (I)' procedural analysis.

G. ruber		***G. siphonifera***	
Sample	**Concentration, Ca (ppm)**	**Sample**	**Concentration, Ca (ppm)**
1TEGR I (0-3cm)	1.29	1TEGS I (0-3cm)	2.147094
2TEGR I (3-5cm)	0.78	2TEGS I (3-5cm)	2.494159
3TEGR I (6-7cm)	1.20	3TEGS I (6-7cm)	0.183303
Mean conc. = 1.09ppm		Mean conc. = 1.61ppm	

*GR represents *G. ruber* and GS represents *G. siphonifera*.

Results obtained from 'Procure Test' analysis suggested the type 'I' cleaning method to be the most appropriate approach producing the optimum average core-top paleotemperature records compared to the type 'II' and type 'III'. However, the final sample concentration (%Ca) remained after TE cleaning was still close to the lower marginal measurement ranges (Table 2.4) indicating a possible risk of appropriate detection during the ICP-OES analysis.

A final set of TE cleaning protocol was thus, decided based on appropriate modifications in the cleaning procedures ensuring effective elemental analysis of the limited available foraminiferal carbonates alongwith with the minimal procedural sample loss. The finalized procedures for TE cleaning of ~100-125µg of carbonate samples of *G. ruber* and *G. siphonifera* for Phase II cleaning, are given in Table 2.5.

Table 2.5: Step wise procedures for Trace Elemental cleaning (Phase II, for G. ruber and G. siphonifera).

Process of Cleaning	***G. ruber***	***G. siphonifera***
Clay Removal (with MQ)	500-750µl	500-750µl
Ultrasonication (duration)	10 sec	8-9 sec
No. of repeat	3	3
Clay Removal (with Methanol)	200µl	200µl
Ultrasonication (duration)	10 sec	8-9 sec
No. of repeat	2	2
Organic Removal (with 1% Alkali buffered H_2O_2)	150µl	150µl
Duration	8-9 min	8-9 min
No. of repeat	2	2
Weak acid leach	NA	NA

The Mg/Ca ratios obtained through the Phase II analysis of *G. ruber* and *G. siphonifera* samples (Table A4) are well within the reported global limits (Mohtadi et al., 2010; Rippert et al., 2015; Ford et al., 2018). The (Al, Fe, Mn)/Ca ratios were under acceptable limits for most of the samples. However, the ratios exceeded the 0.1mmol/mol Ca limit in a few cases where the degree of excess is within the limits of the instrumental analytical precision. The trace elemental ratios of (Al, Fe, Mn)/Ca don't show any co-variance with respect to the Mg/Ca records thus ensuring strong data reliability. Samples with anomalously higher (Al, Fe, Mn)/Ca ratios were rejected out from considerations.

2.7 Stable Isotopic Analysis

The stable isotopic analysis of all the planktonic foraminifers were carried out using the Delta V Isotope Ratio Mass Spectrometer (IRMS) coupled with automated carbonate preparation device, Kiel IV facility at SILICA lab, IISER Kolkata (Fig. 2.17). Using KIEL IV carbonate device for analysis was essential in order to obtain quality data out of limited sample amount (~50-100µg) with better precision (~0.05‰) compared to the conventional manually interfered Carbonate Handling Systems (CHS) (~200µg of carbonate with a precision of 0.1‰). The fundamental principle of isotopic measurement is based on process of reacting the carbonate samples with phosphoric acid to produce the sample CO_2 gas. The CO_2 gas is then thermally ionized and carried into the mass spectrometer in order to measure the different isotopologues of CO_2. The signal intensities of mass-to-charge ratios of 44, 45 and 46 CO_2 isotopologues reflect the abundances of $^{12}C^{16}O^{16}O$, $^{\mathbf{13}}C^{16}O^{16}O$ and $^{12}C^{\mathbf{18}}O^{16}O$. The $\delta^{18}O$ value is calculated from the intensity ratio of masses 46:44.

Figure 2.17: KIEL IV Carbonate Device facility at SILICA lab IISER, Kolkata.

2.7.1 Working Principles of KIEL IV Carbonate System

The KIEL IV Carbonate Device primarily consists of three major sample processing units i.e. a thermostated reaction region, a trapping and gas cleaning system and a microvolume inlet system. The device acts as a fully automated sample preparation system without any manual interferences. The carbonate samples are individually treated with high purity phosphoric acid at elevated temperatures. The reaction releases the sample CO_2 and H_2O along with the non-condensable gases originated from the sample impurities. The released CO_2 is transferred and processed through an all-metal sealed cryogenic trapping system. The cryogenic trapping system consists of a temperature controlled first trap with associated valves, ultra-high vacuum system, a pressure gauge and a microvolume. At first, the CO_2 and H_2O get trapped by the first liquid nitrogen trap at -190°C removing other non-condensable gases out of the channel. The trapped CO_2 is thus purified and further released at -90°C into the microvolume, while the water is completely retained within the first trap. The Isodat software defines the portion of CO_2 to be transferred into the microvolume considering the pressure of the released CO_2 gas ensuring the optimal sample gas pressure in the 3kV DELTA V IRMS system. The pressure of the reference gas supplied parallelly through the dual-inlet system is thus automatically adjusted to the pressure of the sample CO_2. thus The process thus reduces the non-linearities of the mass spectrometer and the analytical uncertainity. Remaining water is removed from the first trapping through baking and evacuating all the valves and gas lines.

2.7.2 Isotopic Analysis

Around 50-100µg of foraminifera samples were crushed and homogenized under cleaned (with acid and MQ, and dried) dry glass plates and transferred into individual sample vials. The vials are placed in to the sample rack and positioned inside the KIEL device assembly. High purity phosphoric acid reservoir present inside under thermostated environment was allowed for heating at 85°C for nearly 45 mins. Phosphorolysis of carbonates, CO_2 transfer and isotopic analysis took place in an automated manner with no cross sample interferences.

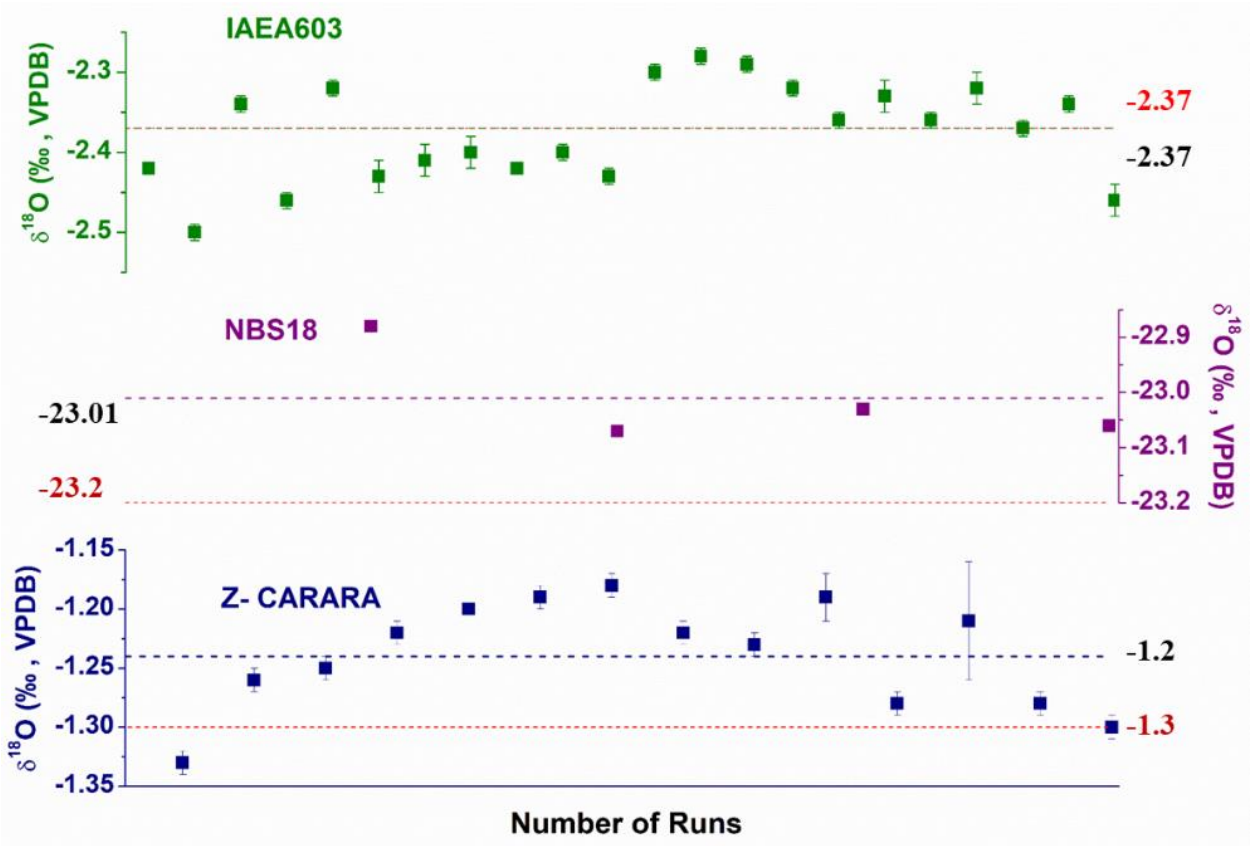

Figure 2.18: Comparison of oxygen isotopic records of different carbonate reference standards measured (mean of multiple runs; black) during the sample analyses with respective consensus values (red).

Known reference standards were run at regular sample intervals to check the data quality and reproducibility. The accuracy and precision obtained through different standard runs in given in Fig. 2.18 and Table 2.6.

Table 2.6: Oxygen isotopic measurements of different carbonate reference standard materials.

Reference Material	Consensus Value ($\delta^{18}O$ ‰, VPDB)	Measured Value* ($\delta^{18}O$ ‰, VPDB)	Deviation from the consensus value (%)	Precision (% RSD)
IAEA603	-2.37	-2.37	0	2.5
NBS18	-23.2	-23.01	0.9	0.3
Z-CARARA	-1.3	-1.24	0.07	3.6

*Indicates the mean value of multiple measurements.

2.8. Estimation of Apparent Calcification Depths (ACDs) and Choices of Appropriate Mg/Ca vs Temperature Calibration Equations

2.8.1 Estimation of Apparent Calcification Depths (ACDs)

The Apparent Calcification Depth (ACD) of an individual planktonic foraminifer represents the average living depth of a planktonic foraminifer within the oceanic water column. Estimation of ACDs of planktonic foraminifers is essential for the selection of suitable Mg/Ca~Temperature calibration equations for paleotemperature reconstructions in the absence of appropriate regional species-specific Mg/Ca ~ Temperature equations. The ACD estimation is also important for the appropriate understandings of the characteristic water depth variabilities and also reconstructing the paleothermocline slope inclinations. The ACDs were obtained by comparing the foraminiferal $\delta^{18}O$ records with the empirically obtained $\delta^{18}O$ profile of the Dissolved Inorganic Carbonate (DIC) ($\delta^{18}Oc$) of the sea water (Anand et al., 2003; Mohtadi et al., 2010; Sagawa et al., 2012).

The oxygen isotopic composition of planktonic foraminifers ($\delta^{18}O_f$) varies as a function of temperature (T_{SW}) and oxygen isotopic composition of the coexisting sea water ($\delta^{18}O_{SW}$). Additionally, the $\delta^{18}O_{SW}$ shows empirically linear variability with respect to the salinity of the sea water (S_{SW}) (Section 1.5.3). At first the present-day $\delta^{18}O_{SW}$ over SK-312/12 location was reconstructed from the mean annual S_{SW} profile obtained from the World Ocean Atlas dataset (WOA2018), using the regional empirical $\delta^{18}O_{SW}$ vs S_{SW} relationship given by Srivastava et al., 2007 (Eq. 2.1), given as:

$$\delta^{18}O_{sw}\ (VSMOW) = -8.89 + 0.27 * S_{sw} \quad \text{(Srivastava et al., 2007)} \qquad (2.1)$$

The $\delta^{18}Oc$ profile was obtained using the mean annual T_{SW} (from WOA2018) and the $\delta^{18}O_{SW}$ (Fig. 2.19) using the experimental relationship provided by Erez and Luz, 1983 (Eq. 2.2), given as:

$$T\ [^{o}C] = 17 - 4.52\ (\delta^{18}O_{carb} - \delta^{18}O_{sw}) + 0.03\ (\delta^{18}O_{carb} - \delta^{18Osw})^2 \quad \text{(Erez and Luz, 1983)} \qquad (2.2)$$

The above relationship (Eq. 2.2) has been commonly utilized for the equatorial Pacific water mass reconstructions and has been chosen for the current study due to the unavailability of appropriate calibrations from the EIO region. The equatorial Pacific is often referred as the most appropriate alternative due to its close similarity and inter-basinal climatic connections with the EIO (Saraswat et al., 2005; Rashid et al., 2007).

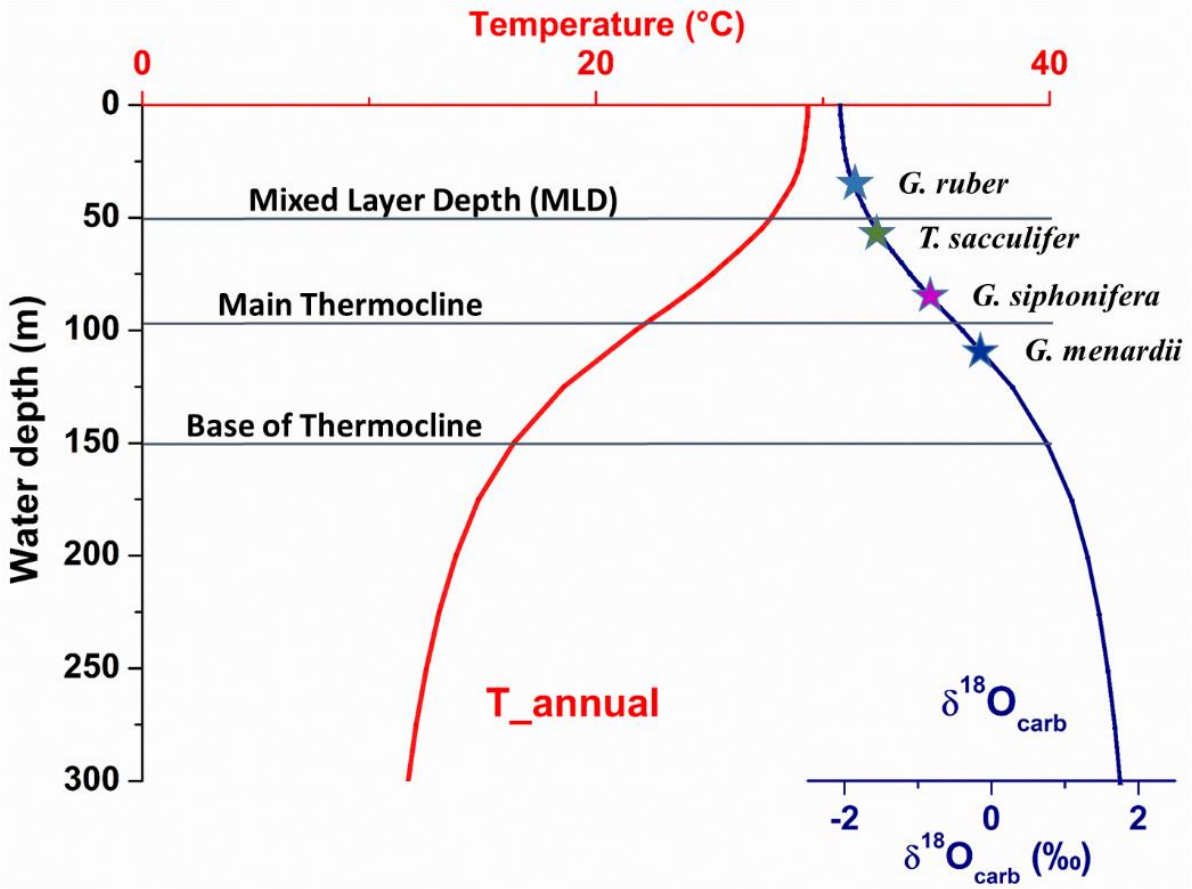

Figure 2.19: Average mean annual temperature (T_annual) and empirical δ^{18}Ocarb profile of SK-312/12 at present. Star (*) represents the estimated ACDs' for the respective planktonic foraminifers.

Average core-top $\delta^{18}O_f$ records are obtained and matched with the empirically obtained δ^{18}Oc profile in order to estimate the ACDs of the individual planktonic foraminifers (Fig. 2.19). Five core-top sections spanning over the Holocene were included in order to obtain the average core-top $\delta^{18}O_f$ records of the chosen depth-specific planktonic foraminifers. The individual ACDs of *G. ruber* (s.s.), *T. sacculifer* (w/s), *G. siphonifera* and *G. menardii* have been obtained to be around 32m, 57m, 83m and 111m respectively indicating a corresponding average oceanic depths habitats of Average Mixed Layer (AML), Mixed Layer Depth (MLD), upper Thermocline (uThm) and lower Thermocline (lThm) respectively (Table 2.7b). Table 2.7 summarises the exercise carried out in order to investigate the validity of all possible sets of ACD estimations obtained through the application of a set of empirical equations most applicable for the EIO region (Stainbank et al., 2019). Estimations are also obtained for three core-top sections. However, the ACD estimations

obtained from the applications of the empirical equation given by Erez and Luz, 1983 (Eq. 2.2) over the five core-top average dataset gives the most reasonable ACD records with reference to the existing IO studies (Fairbanks et al., 1982; Mohtadi et al., 2010; Sagawa et al., 2012; Hollstein et al., 2017a). The individual ACDs estimated for *G. ruber* (s.s.), *T. sacculifer* (w/s), *G. siphonifera* and *G. menardii* are 32m, 57m, 83m and 111m respectively.

Table 2.7: Details of exercise carried out for appropriate ACD estimations over SK-312/12.

(a) List of equations most applicable for EIO as per Stainbank et al., 2019.

Eq1	$T\ [^oC] = 17 - 4.52\ (\delta^{18}O_{Carb} - \delta^{18}O_{SW}) + 0.03\ (\delta^{18}O_{Carb} - \delta^{18}O_{SW})^2$ (Erez and Luz, 1983)
Eq2	$T\ [^oC] = 14.32 - 4.28\ (\delta^{18}O_{Carb} - \delta^{18}O_{SW}) + 0.07\ (\delta^{18}O_{Carb} - \delta^{18}O_{SW})^2$ (Mulitza et al., 2003)
Eq3	$1000\ \ln[d^{18}Ocalcite/d^{18}Osw] = 18.03(1000/T) - 32.42$ (Kim and O'neil, 1997)
Eq4	$T\ [^oC] = 16.9 - 4.38\ (\delta^{18}O_{Carb} - \delta^{18}O_{SW}) + 0.1\ (\delta^{18}O_{Carb} - \delta^{18}O_{SW})$ (Shackleton, 1974)
Eq_ss (*G. ruber*)	$\delta^{18}O_{G.\ ruber} - \delta^{18}O_{SW} = 2.55 - 0.20T$ (r=0.94) (Duplessy et al., 1981)
Eq_ss (*T. sacculifer*)	$\delta^{18}O_{T.\ sacculifer} - \delta^{18}O_{SW} = 2.27 - 0.19T$ (r=0.87) (Duplessy et al., 1981)
Eq_ss (*G. menardii*)	$\delta^{18}O_{G.\ menardii} - \delta^{18}O_{SW} = 2.903 - 0.199T$ (r=0.94) (And and Duplessy, 1985)

*'ss' denotes 'species-specific'.

(b) Appropriate ACDs estimation for SK-312/12.

Species	Av core-top δ18Oforam	Apparent Calcification Depths (ACD) (m)			
		Eq_ss	Eq1	Eq2	Eq4
G. ruber	-1.92	70±2.3m	32±5m	111.8±1.8m	32±5m
T. sacculifer	-1.54	87.3±1.9m	56.8±2.3m	125.5±2.5m	57.3±2.3m
G. siphonifera	-0.89	NA	83.2±1.8m	161.4±3.6m	84.3±1.8m
G. menardii	-0.1	128.5±3.5m	110.7±1.8m	263.6±11.4m	111.8±1.8m

*Bold font represents the most reasonable set of ACDs selected for SK-312/12. No ACDs comparison was obtained using Eq3 for the top 500m oceanic depth.

2.8.2 Choices of Appropriate Mg/Ca vs Temperature Calibration Equations

Appropriate planktonic foraminiferal Mg/Ca vs Temperature calibration equations are absent from the EIO in addition to the selected depth-specific planktonic foraminifers for the present study. Given the fundamental limitations, an effort was made to ensure the selection of the best possible set of calibration equations for the depth-specific upper oceanic plaeothermocline reconstructions for the present study. The equatorial Pacific was selected as the primary region of interest in order to obtain the most appropriate set of Mg/Ca vs Temperature calibration equations.

Under the absence of region specific calibrations, a set of possible calibrations are applied to the foraminiferal Mg/Ca records and the average core-top paleotemperature records are obtained. The average core-top records are then compared with the mean present-day records from the corresponding oceanic depths (Hastings et al., 1998; Rongstad et al., 2020). The calibrations producing the closest average core-top records compared to the mean present-day counterparts are considered as the most appropriate choices.

Table 2.8 represents the average core-top paleotemperature records obtained out of the most applicable calibrations available from the equatorial Pacific Ocean subjected to the selected

Table 2.8: ACDs and selected Mg/Ca vs T calibrations obtained for different planktonic foraminifers.

Species	**ACD (m)**	**Characteristic depth**	**Present T at ACD (°C)**	**Calibration Eq. Mg/Ca~T**	**±σ (°C)**	**Av core-top T_Calibrated (°C)**
G. ruber (s.s.)	32	Average Mixed Layer (AML)	28.8	T= (1/0.077)*ln ((Mg/Ca)/0.455) (Sagawa et al., 2012)	±1.1	28.4
T. sacculifer (w/s)	57	Mixed Layer Depth (MLD)	27.1	T= (1/0.097)*ln ((Mg/Ca)/0.24) (Hollstein et al., 2017b)	±1.0	26.1
G. siphonifera	83	upper Thermocline (uThm)	24.1	T= (1/0.077)*ln ((Mg/Ca)/0.455) (Sagawa et al., 2012)	±1.1	23.1
G. menardii	111	lower Thermocline (lThm)	20.4	T= (1/0.097)*ln ((Mg/Ca)/0.21) (Hollstein et al., 2017b)	±1.0	20.5

foraminiferal species and the equivalent oceanic depth habitats. The species-specific calibrations given by Hollstein et al., 2017 and the multi-species calibration given by Sagawa et al., 2012 were chosen as the best suitable temperature calibration equations for *T. sacculifer* (w/s) and *G. menardii*, and *G. ruber* (s.s.) and *G. siphonifera* respectively. The selected equations are thus, moreover constrained through region, species and depth of oceanic habitat.

2.9 Paleosalinity Reconstruction

The salinity of the ocean represents the total amount of dissolved salt content present within the sea water. In modern oceanographic studies the salinity is represented in terms of the practical salinity unit (PSU) derived from the conductance of the sea water parcel obtained during the CTD operations. The salinity of the sea water (S_{SW}) shows empirically linear relationships with the $\delta^{18}O_{SW}$ since both of the parameters originate from the common ocean-atmospheric coupling processes. Paleosalinity reconstruction of the upper EIO is carried out by applying appropriate $S_{SW} \sim \delta^{18}O_{SW}$ calibrations obtained from the present-day water mass studies, to the $\delta^{18}O_{SW}$ records reconstructed from the paired Mg/Ca and $\delta^{18}O_f$ analyses. The analytical approach utilizes the same set of empirical equations used for ACD calculations (section 2.8.1) but in the reverse order. At first the $\delta^{18}O_{SW}$ record of the past oceanic water mass is reconstructed from the foraminiferal Mg/Ca derived paleo temperature records combined with the corresponding $\delta^{18}O_f$ records obtained from the oxygen isotopic analysis (section 2.7.2) using the empirical relationship given by Eq. 2.2. The obtained paleo $\delta^{18}O_{SW}$ records are then corrected for the Global Ice Volume (GIV) effect using linear interpolation of the GIV correction dataset provided by Waelbroeck et al., 2002 in order to remove the changes in the $\delta^{18}O_{SW}$ caused by global ice-melt fractions. The GIV corrected $\delta^{18}O_{SW}$ records are then applied into the $S_{SW} \sim \delta^{18}O_{SW}$ relationship given by Eq. 2.1 in order to obtain the paleosalinity reconstruction records from the upper EIO. Ideally, the ocean-atmospheric processes governing the surface and the thermocline salinity variations do not remain exactly the same throughout the upper ocean. Hence, the $S_{SW} \sim \delta^{18}O_{SW}$ calibrations can strongly differ between the surface and subsurface water mass regions. However, due to the absence of any appropriate subsurface $S_{SW} \sim \delta^{18}O_{SW}$ calibrations from the EIO thermocline, the present study utilizes the available surface oceanic calibration provided by Srivastava et al., 2007 (Eq. 2.1) as the common equation for the paleosalinity reconstruction of the complete upper EIO.

Chapter 3

Sea Water Radiocarbon Reconstructions and Evidence of a Hydrothermal 'Mystery Interval' during the MIS 3-MIS 2 Transition Period

---

3.1 Introduction: Literature Review

The study of thermocline radiocarbon reconstructions acquired primary scientific attention with the evidence of anomalously radiocarbon depleted records obtained across the global oceanic thermoclines (Marchitto et al., 2007; Stott et al., 2009; Bryan et al., 2010; Thornalley et al., 2011) and shallow intermediate waters (Sikes et al., 2000) during the early deglaciation period (~18 ka afterwards; Fig. 3.1). The degree of anomalous radiocarbon depletions with respect to the contemporaneous atmospheric records couldn't be explained by any kinds of surface and subsurface water mass processes existing during the deglacial time periods (Fig. 3.2). Evidence from ocean-atmospheric climatic modelling studies (Stephens and Keeling, 2000), the Antarctic type Sea Surface Temperature (SST) patterns from low latitude thermoclines (Kiefer et al., 2006; Mohtadi et al., 2010; Naidu and Govil, 2010), the deglacial Antarctic climatic variabilities along with the globally distributed Carbon Isotope Minimum Events (CIME) (Ziegler et al., 2013) collectively indicated towards a common source of origin for the observed deglacial radiocarbon anomalies. The observations led the scientific community to come up with a high level hypothesis that suggests that all the observations are possibly caused by the release of excessive carbon dioxide (CO_2) from an aged supersaturated deep southern oceanic reservoir via upwelling (Stephens and Keeling, 2000; Spero and Lea, 2002), which led to a subsequent increase in the deglacial Antarctic ocean and atmospheric CO_2 and temperature records. A transport of these extremely radiocarbon depleted water into the lower latitude oceans via Sub-Antarctic Mode Water- Antarctic Intermediate Water (SAMW-AAIW) (Spero and Lea, 2002; Liu and Yang, 2003) resulted in a subsequent anomalous radiocarbon depletions in the associated thermoclines and shallow intermediate water depths.

The deglacial radiocarbon depletions from the global ocean thermocline records associated with the southern oceanic source, have reported thermocline $\Delta^{14}C$ ($\Delta\,^{14}C_{Thm}$) values reaching up to a minimum of ~-250‰, i.e. around 520‰ lower than the corresponding atmosphere (Bryan et al., 2010). However, extreme depletions of $\Delta\,^{14}C_{Thm}$ have also been reported from the Eastern Equatorial Pacific (EEP) thermocline during the last deglacial period, where the $\Delta\,^{14}C_{Thm}$ reached up to ~-580‰, observing a ~800‰ lowering compared to the contemporaneous atmosphere. Such extreme depletions are too high in magnitude to be explained by the process of aged supersaturated southern oceanic source contribution (Stott et al., 2009). The exact explanations remained a

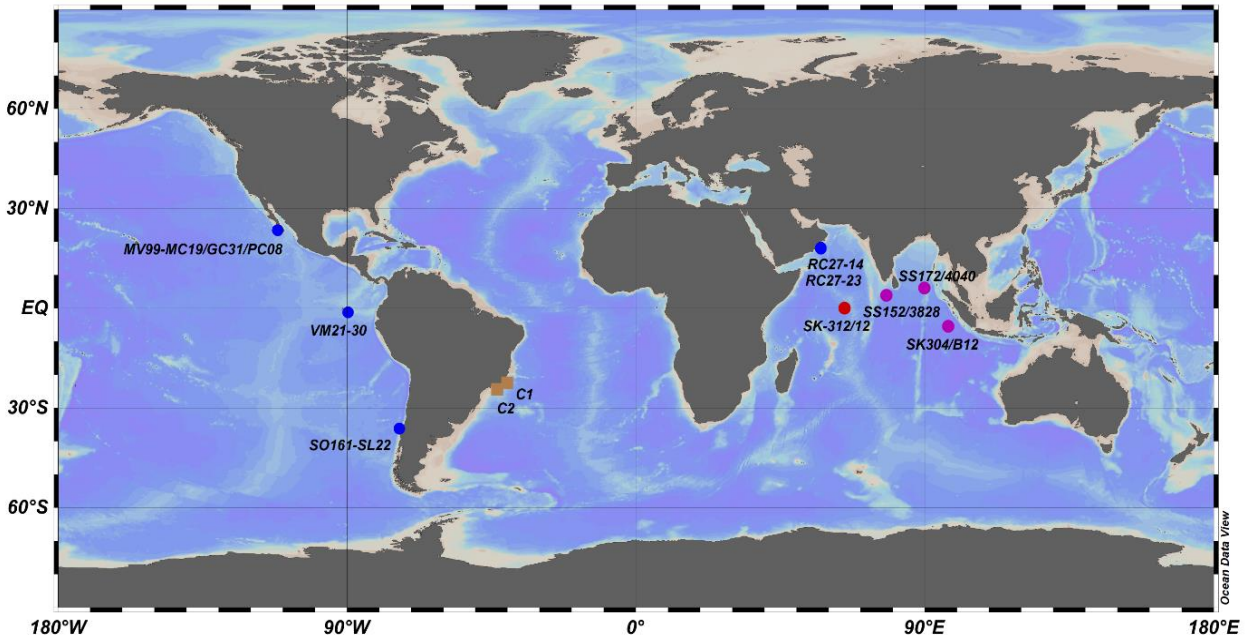

Figure 3.1: Location of global studies discussed in this chapter: core SK-312/12 (present study), core SS152/3828, core SS172/4040 and core SK304/B12 (from EIO (Bharti, 2021; Bharti et al., 2022)), core RC27-14 and RC-27-23 (Arabian sea (Bryan et al., 2010)), multi-core MV99-MC19/GC31/PC08 (Baja, California (Marchitto et al., 2007)), core VM21-30 (Eastern Equatorial Pacific (EEP) (Stott et al., 2009)) and core SO161-SL22 (Chille margin (De Pol-Holz et al., 2010)). C1 and C2 are the deep sea coralline records (Brazil margin (Mangini et al., 2010)).

mystery, until Stott et al., 2019 proposed possible evidence of episodic release of geologic (hydrothermal) carbon into the EEP thermocline as the primary cause responsible for it.

3.2 Motivation and Objectives

The EIO Indian Ocean thermocline is strongly inter-connected with the regional (Annamalai et al., 2005) and global scale climatic variabilities through different ocean-atmospheric and climatic feedback mechanisms (Saji et al., 1999; Mohtadi et al., 2010). The hydrology of the upper EIO is associated with a number of discrete source supplies with distinct water mass properties and variable spatial contributions. Isopycnal studies (You, 1998) have shown present-day evidence of Antarctic water mass influence over the Equatorial Indian Ocean (EIO) through the SAMW-AAIW via ocean-tunnelling (Liu and Yang, 2003) with minimal contribution from ITF. Production and contribution of different intermediate water mass sources into the EIO thermocline are expected to vary over the past glacial-interglacial time periods

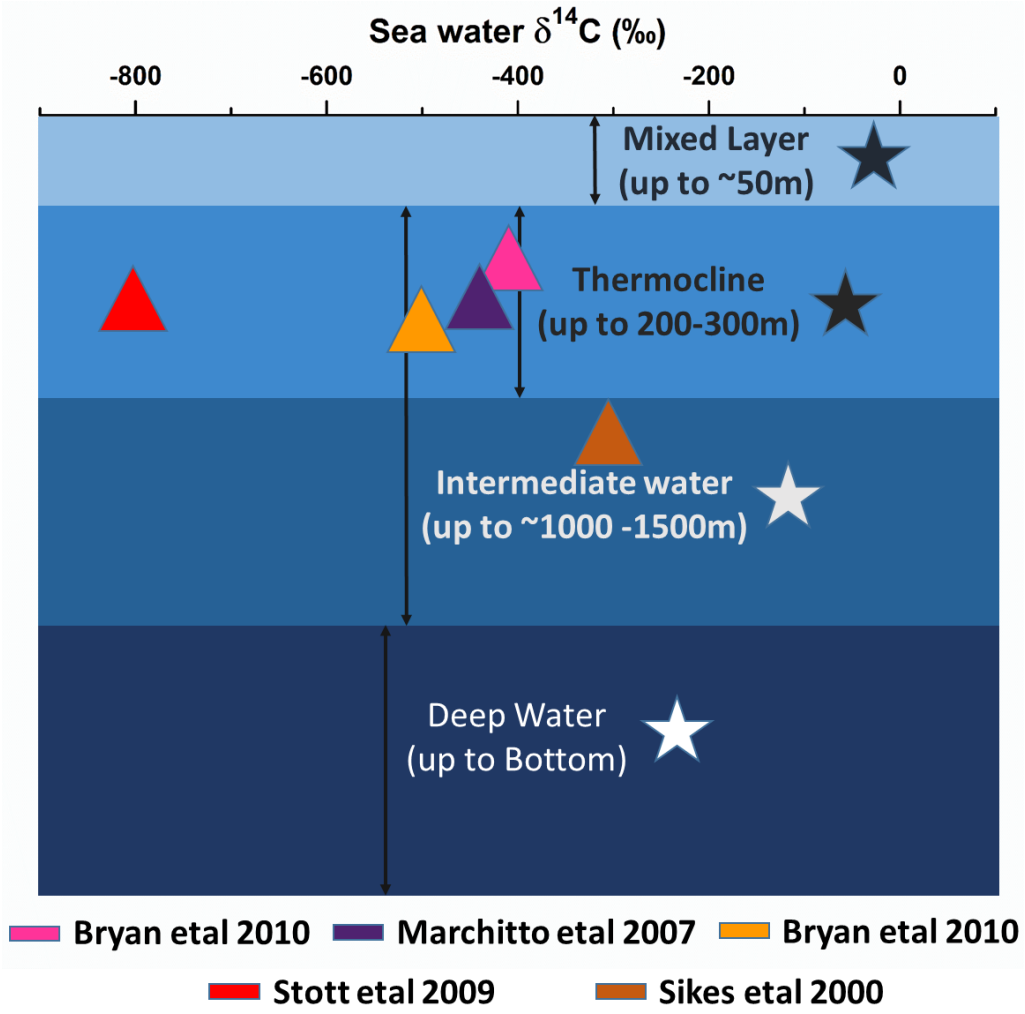

Figure 3.2: Schematic of anomalous early deglacial radiocarbon records obtained from different global oceanic thermoclines and shallow intermediate regions.

through changes in the regional and global sea levels (Kuhnt et al., 2004) as well. Reconstructions of paleothermocline ventilation records from the upper EIO are sparse due to the major challenges associated with the extremely low sedimentation rates and limited sample availabilities. The existing limitations have resulted in an inconclusive understanding about the spatial and temporal distribution of $\Delta^{14}C_{Thm}$ records and the contribution of different source water mass regions in the evolution of the upper EIO radiocarbon ventilations over the glacial-deglacial time periods (Romahn et al., 2014).

The volcanic-hydrothermal systems produce substantial amount of dead geologic carbon in the form of CO_2. The produced CO_2 can lead to extreme radiocarbon depletions in the surrounding oceanic water columns upon mixing. Hydrothermal inputs into the intermediate waters of the

southern Arabian Sea in the tropical Indian Ocean, have been observed to be sourced from large chronic plume events originating from the hydrothermal vents present along the Carlsberg Ridge (Kadko et al., 1995; Chinni and Singh, 2022) following extensive lateral advections (Massoth, 1994) and carriage via the AAIW. In addition to the presence of a number of Mid Oceanic Ridges (MORs) across it, the Indian ocean also hosts a number of potential hotspot systems (Fig. 3.3) which could also act as possible hydrothermal dead carbon sources into the EIO thermocline during the paleoclimatic periods as well.

The present study is a maiden attempt from an open oceanic region in order to reconstruct the millennial scale radiocarbon ventilation records from the upper EIO using the radiocarbon dating technique of depth-specific planktonic foraminifers. The study aims at understanding the evolution of the millennial scale upper oceanic radiocarbon ventilations, the sources and mechanisms of thermocline radiocarbon supply and the global tele-climatic implications of the upper EIO radiocarbon variability over the past 44 ka time period.

3.3 Sources of Radiocarbon Ventilations at Present

The surface oceanography of the studied region SK-312/12 (Fig. 2.2) (0.0068°N; 65.0048°E, water depth 3750m) is predominated by a westward flowing South Equatorial Current (SEC), an eastward flowing Monsoon Current and a strong western boundary Somali Current (SC) (Divakar Naidu and Malmgren, 1999) predominate during the South-West Monsoon (SWM) season. The North-East Monsoon (NEM) current flows westward across the basin, carrying the fresher Bay of Bengal (BoB) water into the studied region (Schott et al., 2009). The thermocline water in this region is supplied dominantly by SAMW-AAIW with a minor contribution from the Indonesian Through Flow (ITF) (You, 1998). However, the ITF signal gets intensely mixed as it crosses through various sills in the Indonesian Sea before reaching into the present studied region (Winfree et al., 1970) (section 2.2).

Among the MORs spread across the Indian Ocean (Fig. 3.3), the Carlsberg Ridge (CR) and the Chagos-Laccadive Ridge (CLR) extend from the Arabian Sea (AS) in the north to the central EIO region. The East Indian Ridge (EIR) spreads across the equator in a north-south trend in the eastern part of the Indian Ocean whereas, the Central Indian Ridge (CIR), the South West Indian Ridge (SWIR) and the South East Indian Ridge (SEIR) transect each other at the Rodriguez Triple Junction (RTJ) in the southern sub-tropics. The active Reunion hotspot and the Amsterdam

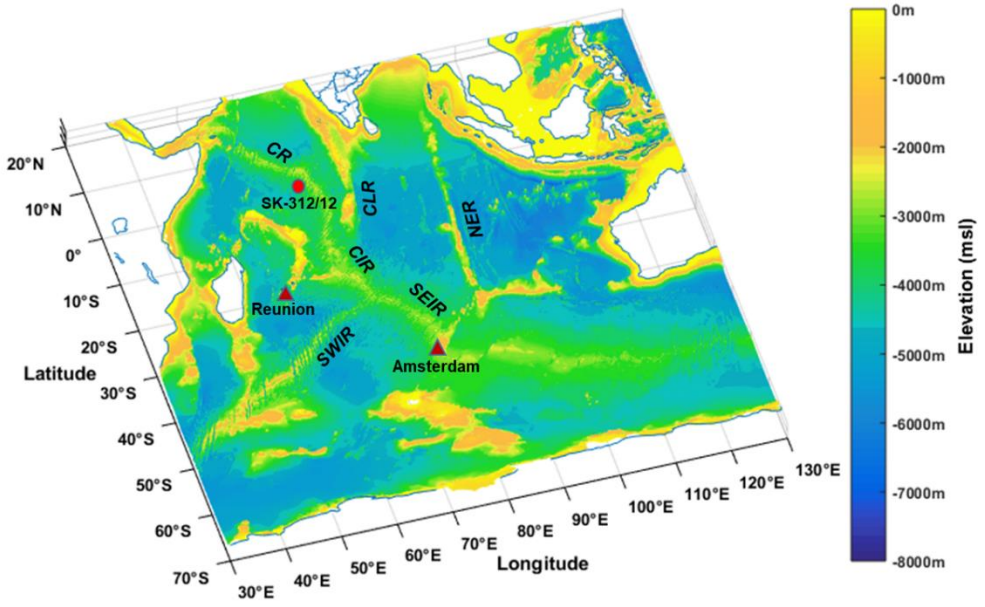

Figure 3.3: List of MORs and major volcanic hotspot systems (discussed in this study) located in the Indian Ocean basin: CR- Carlsberg Ridge, CLR- Chagos-Laccadive Ridge, NER- Ninety East Ridge, CIR- Central Indian Ridge, SWIR- South West Indian Ridge and SEIR- South East Indian Ridge. The red dot shows the location of core SK-312/12. Bathymetry data source: (NASA Earth Observations et al., 2002).

volcanic island are also present in the central Indian Ocean and the south Indian Ocean respectively.

3.4 Calculation of Sea Water Radiocarbon Concentration

The $\Delta^{14}C$ concentration of past sea water for the mixed layer and the thermocline were calculated using the following equation (1) given by Adkins and Boyle, 1997, in order to obtain the initial sea water $\Delta^{14}C$ concentration, given as;

$$\Delta^{14}C_{WM} = [\{e^{(-14C\ age/8033)} / e^{(-Cal\ age/8266)}\}-1]*1000 \quad (1)$$

Where WM denotes water mass and the unit of $\Delta^{14}C_{WM}$ is ‰. The ^{14}C age is the radiocarbon age and Cal age is the calendar age respectively. Values 8033 and 8266 are the libby and true mean life times of ^{14}C respectively.

3.5 Results

3.5.1 SK-312/12 Records

The radiocarbon record of seawater from SK-312/12 mixed layer ($\Delta^{14}C_{ML}$) and thermocline ($\Delta^{14}C_{Thm}$) (Table. 3.1) are plotted in Fig. 3.4. The $\Delta^{14}C_{ML}$ varies between a minimum of ~-4‰ at 6 ka BP to a maximum of ~420‰ at ~33.7 ka BP, with a mean $\Delta^{14}C_{ML}$ of ~215‰. The timing of $\Delta^{14}C_{Thm}$ minimum coincides with that of the $\Delta^{14}C_{ML}$ maximum with a magnitude of ~-455‰. The $\Delta^{14}C_{Thm}$ maximum of ~190‰ is observed during the LGM. The average $\Delta^{14}C_{Thm}$ remains at ~-145‰.

The $\Delta^{14}C_{ML}$ variation of SK-312/12 is more or less similar with the northern hemispheric atmospheric $\Delta^{14}C$ ($\Delta^{14}C_{Atm}$) record (Reimer et al., 2020). The overall $\Delta^{14}C_{ML}$ is lower than the corresponding $\Delta^{14}C_{Atm}$ ranging between ~25-190‰, which is attributed to the reservoir age corrections. A comparison with the surface oceanic $\Delta^{14}C$ ($\Delta^{14}C_{Sur}$) records from the EIO reported by Bharti, 2021; Bharti et al., 2022 (Fig. 3.5) shows a similar trend of variation among all the data sets. The $\Delta^{14}C_{Thm}$ variability are comparable among these EIO cores (Fig. 3.5 and Table 3.2) along with that of the Arabian Sea (AS) (Bryan et al., 2010) and the Baja California (Marchitto et al., 2007) record (Fig. 3.6). This provides reliability to the current data set and the sample treatment procedures followed. Additionally, it also indicates that the effect of secondary calcification and diagenetic alteration are negligible on the mixed layer and thermocline foraminifer species over the studied region, unlike the benthic foraminifers that thrive under ambient bottom oceanic conditions. Rigorous sample treatments like Barker et al., 2003 (method for Mg/Ca analysis, which is followed by Bharti, 2021; Bharti et al., 2022) thus, need not be followed.

Table 3.1: Chronology and radiocarbon records (Mixed Layer and Thermocline) of core SK-312/12.

Mixed Layer						Thermocline		
Core Depth (cm)	**^{14}C age (yr BP)**	**Error (±1σ) (yr)**	**Calendar age (yr BP)**	**Error (±1σ) (yr)**	**$\Delta^{14}C_{ML}$ (‰)**	**^{14}C age BP**	**Error (±1σ) (yr)**	**$\Delta^{14}C_{Thm}$ (‰)**
4	6076	72	6214	218	-4	6240	68	-24
6.5	6554	53	7075	163	40	7010	58	-16
9.5	8064	75	8560	237.5	32	9900	125	-178
11.5	9011	58	9316	192.5	5	10317	59	-145
14.5	9348	78	10341	253.5	91	10688	69	-76
16.5	10539	71	11393	201	68	13075	107	-220
19.5	11845	77	13168	244.5	125	13695	71	-105
21.5	12828	118	14668	212	194	15372	73	-129
24.5	14237	68	17068	222	339	16512	82	9
26.5	16623	100	18256	168	149	17971	84	-28
29.5	16965	73	19798	19798	327	19302	77	-7
31.5	18108	80	21207	229.5	365	19212	79	189
35.5	20789	91	23912	235	356	23636	106	-48
39.5	20828	126	24210	347	399	25643	124	-231
45.5	23709	99	27108	279.5	388	29858	147	-354
49.5	26716	123	30110	310.5	372	32971	190	-369
55.5	28293	147	31450	332	326	35122	200	-433
65.5	29934	153	33710	439.5	421	37666	258	-457
69.5	41969	376	43871	678	86	44180	371	-175

The late MIS 3 (Marine Isotope Stage 3) $\Delta^{14}C_{ML}$ at ~34 ka BP is ~355‰ higher compared to the mid MIS 3 (~44 ka BP) record. The $\Delta^{14}C_{ML}$ further reduces to ~325‰ at ~31.5 ka BP and remained more or less steady around ~385‰ till 24 ka BP. The early LGM (Last Glacial Maximum) shows

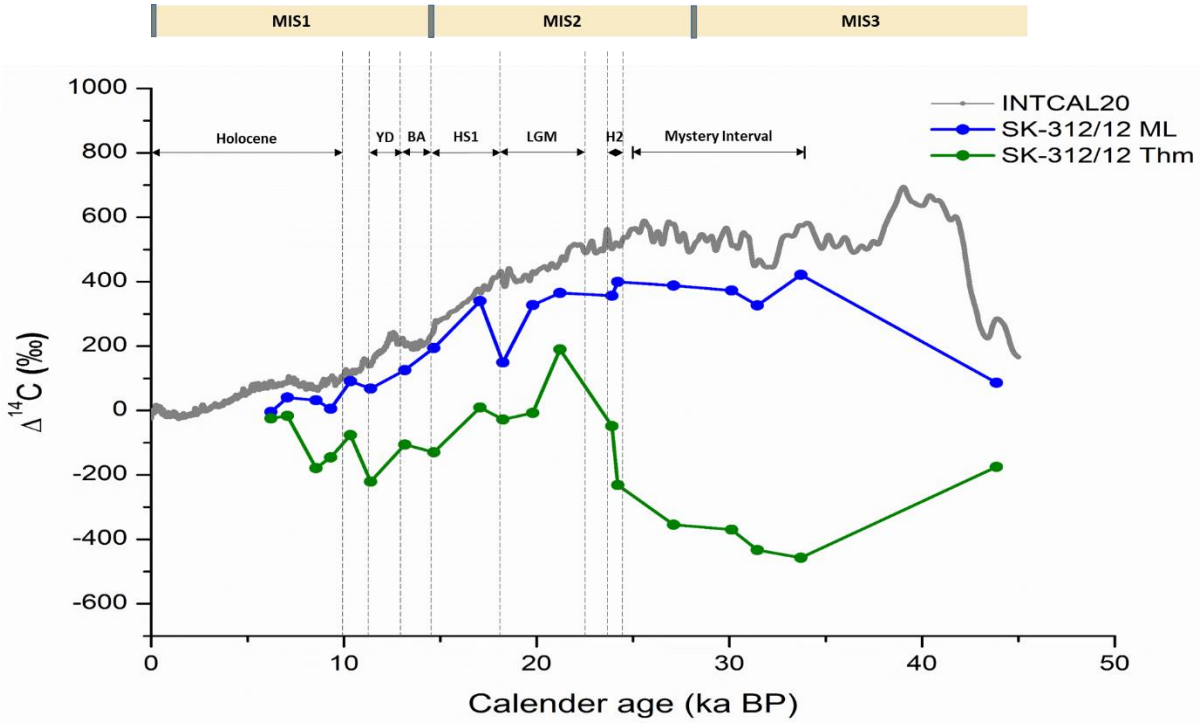

Figure 3.4: $\Delta^{14}C$ records of core SK-312/12 (mixed layer (ML): blue and thermocline (Thm): olive green) along with the northern hemispheric atmospheric $\Delta^{14}C$ record ($\Delta^{14}CAtm$) (INTCAL20) (Reimer et al., 2020) (grey).

a steady record of ~360‰ till ~21 ka BP followed by a sharp reduction (by ~175‰) between ~19.8 ka BP to 18.3 ka BP during the end of LGM. The deglacial period began with a sharp rise in the $\Delta^{14}C_{ML}$ by ~190‰, reaching up to ~340‰ at 17 ka BP following decrease up to the early Holocene (~9.3 ka BP). The later part of Holocene observed a limited variation to reach to the minimum value of ~-4‰ around ~6 ka BP.

The late MIS 3 records the minimum $\Delta^{14}C_{Thm}$ of ~-455‰ at ~33.7 ka BP. It gradually increases up to ~-230‰ till ~24 ka BP. The boundary period at 24 ka BP observes a sharp increase by ~180‰ in $\Delta^{14}C_{Thm}$. The $\Delta^{14}C_{Thm}$ further follows a significant increase by ~230‰ reaching the highest value of ~190‰ during the LGM (at ~21.2 ka BP). This highest peak was immediately followed by ~200‰ reduction in the $\Delta^{14}C_{Thm}$ during the latter part of LGM. A continuous decrease was followed there after till ~11.4 ka BP. The transition to Holocene is marked by ~145‰ increase at ~10.3 ka BP. A further decrase (up to ~8.5 ka BP) and increase (from ~8.5 ka BP onwards) by ~100‰ and ~150‰ respectively were observed in the $\Delta^{14}C_{Thm}$ for the rest part of the Holocene. The $\Delta^{14}C_{Thm}$ shows moderate to extremely high depletions from the atmospheric value for the most

of the core records. The deglacial period, the LGM, early MIS 2 (Marine Isotopic Stage 2) and late MIS 3 record a maximum atmosphere to thermocline $\Delta^{14}C$ contrast of ~350‰, ~400‰, ~920‰ and ~1030‰ respectively.

3.5.2 Regional and Global Comparison

The $\Delta^{14}C_{ML}$ record of SK-312/12 shows closely similar variations with the surface $\Delta^{14}C$ records reported by Bharti, 2021 and Bharti et al., 2022 from the EIO indicating a common surface and mixed layer radiocarbon dynamics operating over this region. The $\Delta^{14}C_{Thm}$ record of SK-312/12 show minor variations relative to the other EIO cores (except a few anomalous points of SK304/B12) (Fig. 3.5 and Table. 3.2) possibly caused by spatially different thermocline hydrologies. Considerable number of $\Delta^{14}C_{Thm}$ data points from multi-core record MV99-MC19/GC31/PC08 (Marchitto et al., 2007) and RC27-14 & RC27-23 (Bryan et al., 2010) lie almost in similar range with SK-312/12 core records for the last ~24 ka. However, the $\Delta^{14}C_{Thm}$ of SK-312/12 reduces to extremely lower range for the remaining part of the record which is the principal matter of discussion of this current study (Fig. 3.6). The deep sea coral records from the Brazil margin (Mangini et al., 2010) represent relatively higher values than SK-312/12 thermocline for most of the time period. Core VM21-30 from the Eastern Equatorial Pacific (EEP) (Stott et al., 2009) has recorded a 'Mystery Interval' with $\Delta^{14}C_{Thm}$ reaching up to ~-850‰ with respect to the corresponding atmospheric record. The magnitude of $\Delta^{14}C_{Thm}$ depletions are comparable with the extremely anomalous $\Delta^{14}C_{Thm}$ depletions recorded by SK-312/12 between 25-34 ka BP during the MIS 3-MIS 2 transition. We identify this event of anomalously high $\Delta^{14}C_{Thm}$ depletion from core SK-312/12 as a newly identified MIS 3-MIS 2 transition 'Mystery Interval'.

Table 3.2: Thermocline radiocarbon records of core SK304/B12.

Chronology		Thermocline			
Calendar age (yr BP)	**Error (±1σ) (yr)**	**Species**	**^{14}C age BP**	**Error (±1σ) (yr)**	**$\Delta^{14}C_{Thm}$ (‰)**
11397	150	P. obliquiloculata	11176	63	-12.4029
12314	168.5	P. obliquiloculata	11611	48	45.30033
13358	123	P. obliquiloculata	18647	57	-506.031
13806	160	P. obliquiloculata	13414	57	0.353582
13481	128	P. obliquiloculata	13752	49	-77.8438
19750	220	P. obliquiloculata	33354	164	-828.439
32572	301.5	P. obliquiloculata	35429	136	-374.968
34037	167	P. obliquiloculata	33481	213	-48.9809
34364	153	P. obliquiloculata	37256	164	-381.587

3.6 Discussions

The $\Delta^{14}C_{ML}$ variability from core SK-312/12 is quite similar to the $\Delta^{14}C_{Atm}$ record (Reimer et al., 2020), indicating a strong atmospheric coupling with the mixed layer for most of the time period. However, the $\Delta^{14}C_{Thm}$ record of SK-312/12 remains strongly decoupled from the mixed layer and the atmosphere, indicating a major control of subsurface oceanic processes and surface stratification on the paleo thermocline ventilation of the western central EIO (Fig. 3.4).

3.6.1 The MIS 3-MIS 2 Transition 'Mystery Interval'

The $\Delta^{14}C_{Thm}$ record from core SK-312/12 observes extremely depleted radiocarbon concentrations of ~1000‰ with respect to the corresponding atmosphere during the 25-34 ka BP 'Mystery Interval'. Marchitto et al., 2007 and Bryan et al., 2010 proposed the external influx of $\Delta^{14}C$ depleted southern water as the primary cause of highly depleted intermediate waters observed from the Baja, California and the Arabian Sea during the early deglaciation. This could account only for

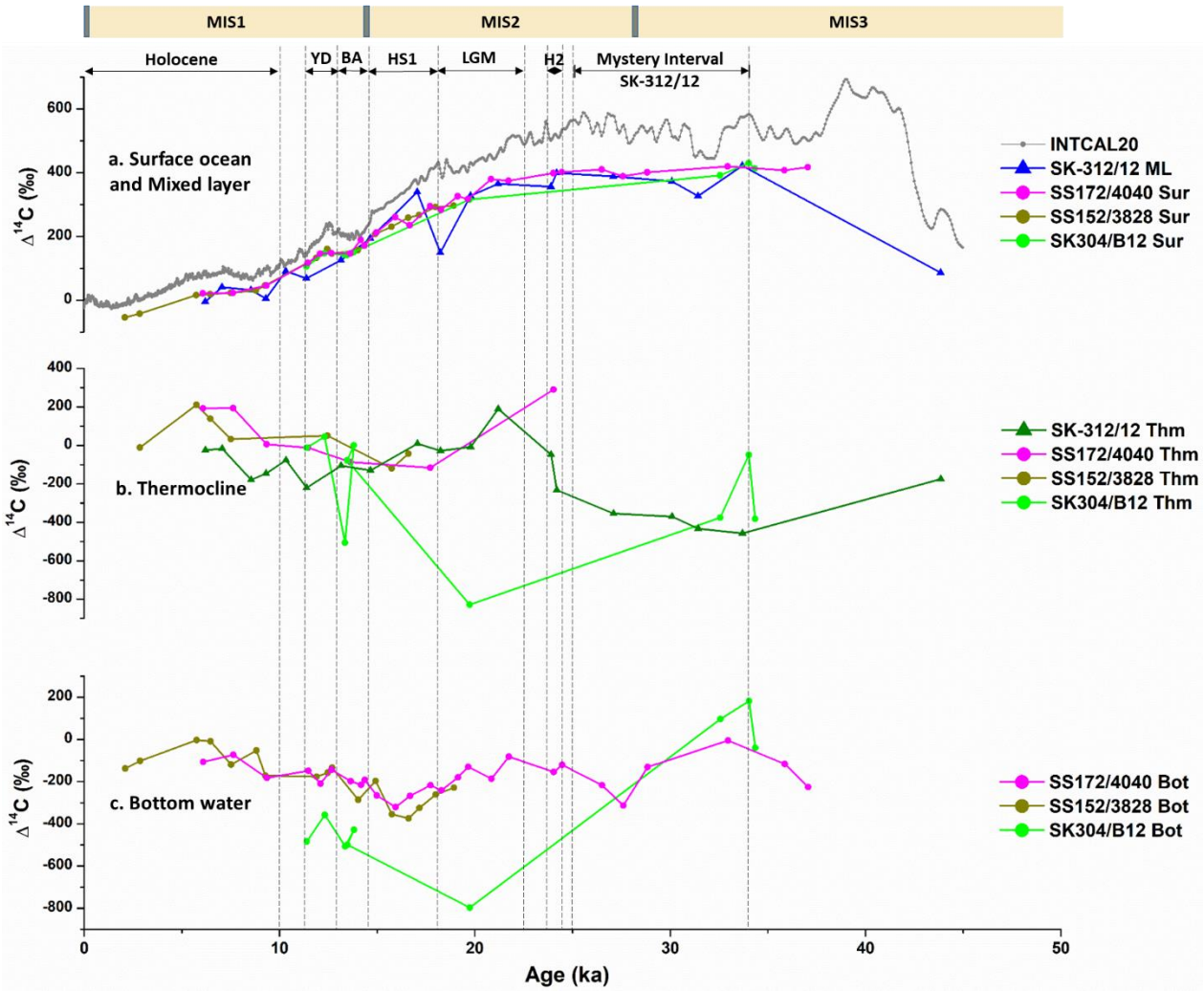

Figure 3.5: Comparison of $\Delta^{14}C$ records of core SK-312/12 with available EIO (core SS152/3828 and core SK304/B12) and south BoB (core SS172/4040) records from (Bharti, 2021; Bharti et al., 2022). (a) The surface ocean (Sur) and mixed layer (ML) records, plotted against the northern hemispheric atmospheric $\Delta^{14}C$ record ($\Delta^{14}C_{Atm}$) (INTCAL20) (Reimer et al., 2020), (b) The thermocline (Thm) records and (c) The bottom water (Bot) records.

~460‰ $\Delta^{14}C_{Thm}$ depletions with respect to the contemporaneous atmospheric record (Bryan et al., 2010; Marchitto et al., 2007) (Fig. 3.6). Additionally, Bryan et al., 2010 stated that processes like in-situ aging and upward mixing of ^{14}C depleted deep water are unlikely to contribute such excess degrees of $\Delta^{14}C_{Thm}$ depletions, since the vertical diffusive mixing is quite slow across the thermocline (Fairbanks, 1989) and the possibility of mixing from the deep ocean is limited to more than ~3 km water depths (Broecker and Barker, 2007). However, Stott et al., 2009 reported an

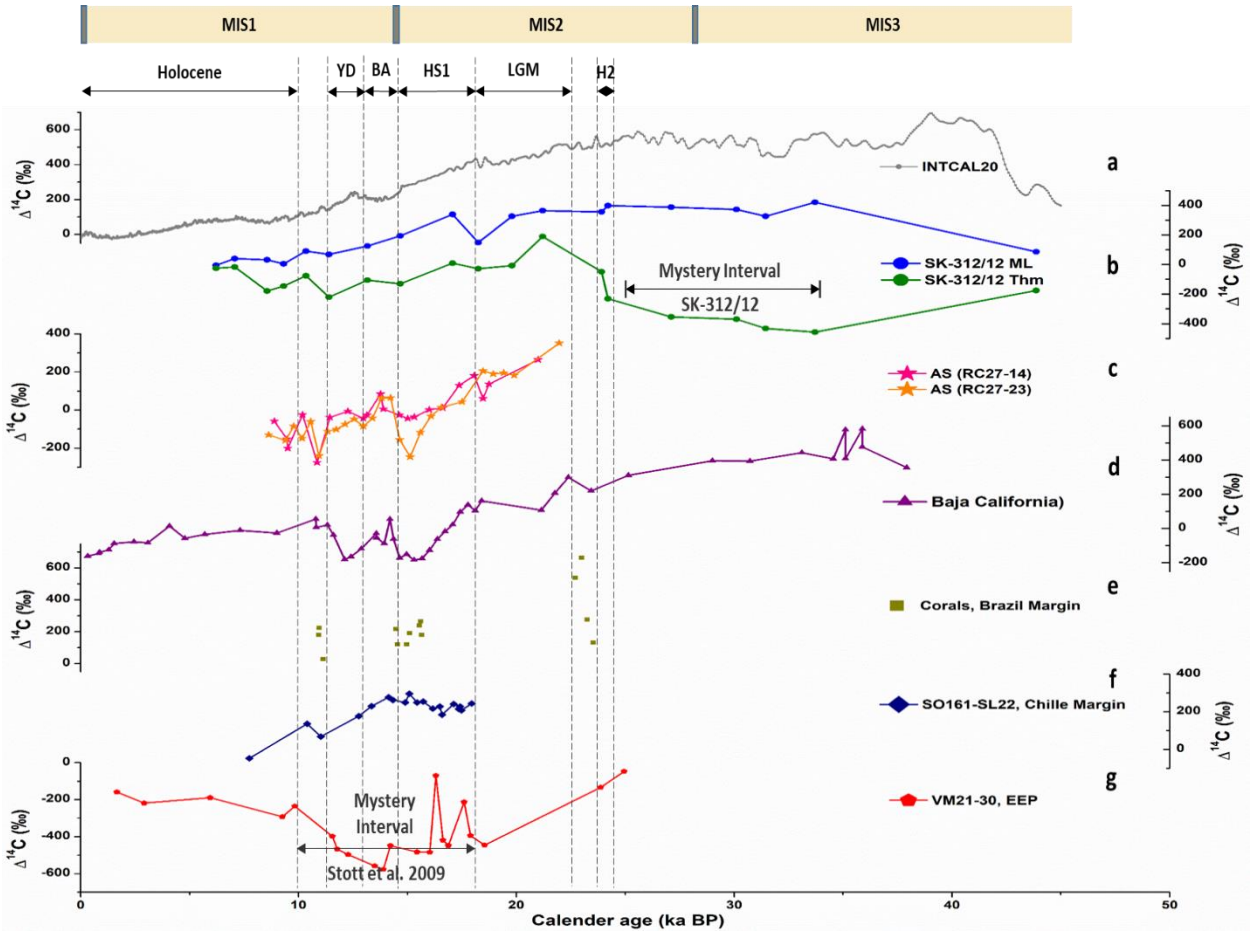

Figure 3.6: $\Delta^{14}C$ records from global ocean thermoclines (b (olive green), c, d, e, f and g) along with the northern hemispheric atmospheric record (a) and the mixed layer record from SK-312/12 (b (blue)). a. Northern hemispheric atmospheric record (Δ^{14}CAtm) (INTCAL20, Reimer et al., 2020) (gray), b. Mixed layer (blue) and thermocline (olive green) records from SK-312/12, c. Sediment core records from RC27-14 (pink) and RC-27-23 (orange) (Arabian sea (Bryan et al., 2010)), d. Multi-core record from MV99-MC19/GC31/PC08 (Baja, California (Marchitto et al., 2007)) (violet), e. Deep sea coralline records (Brazil margin (Mangini et al., 2010)) (dark yellow), f. Sediment core record from SO161-SL22 (Chille margin (De Pol-Holz et al., 2010)) (navy blue) [The ^{14}C ages have been recalibrated using Marine20 calibration curve (Heaton et al., 2020) in CALIB 8.2 (Stuiver et al., 2021) with a reservoir age of 49±30 yr (Merino-Campos et al., 2019)] and g. Sediment core record from VM21-30 (Eastern Equatorial Pacific (EEP) (Stott et al., 2009)) (red).

extreme $\Delta^{14}C_{Thm}$ depletion of ~850‰ with respect to the corresponding atmosphere from the EEP during the early deglaciation period (Fig. 3.6). The magnitude of such a depletion is too high to be

explained by the ventilation of deglacial aged southern-oceanic source via SAMW/AAIW (Stott et al., 2019). The reason remained a mystery until Stott et al., 2019 proposed evidence of episodic hydrothermal carbon release to be the plausible cause of extreme radiocarbon depletion in the EEP thermocline. In addition to SK-312/12, core SK304/B12 from eastern EIO (Fig. 3.1) also shows such extreme level of $\Delta^{14}C_{Thm}$ depletions during ~32-34 ka BP (Fig. 3.5, Fig. 3.7 and Table. 3.2). Due to extremely limited benthic foraminifer abundance, the bottom water $\Delta^{14}C$ ($\Delta^{14}C_{Bot}$) records of the core SK-312/12 could not be reconstructed. However, an assessment from available EIO records (Bharti, 2021; Bharti et al., 2022) suggest absence of any anomalous bottom water conditions over EIO during the studied time period. Under such circumstances, the extreme level of $\Delta^{14}C$ depletions in the SK-312/12 thermocline could only occur due to a selective ventilation of highly anomalous ^{14}C depleted source in to its thermocline during the 25-34 ka BP Mystery Interval.

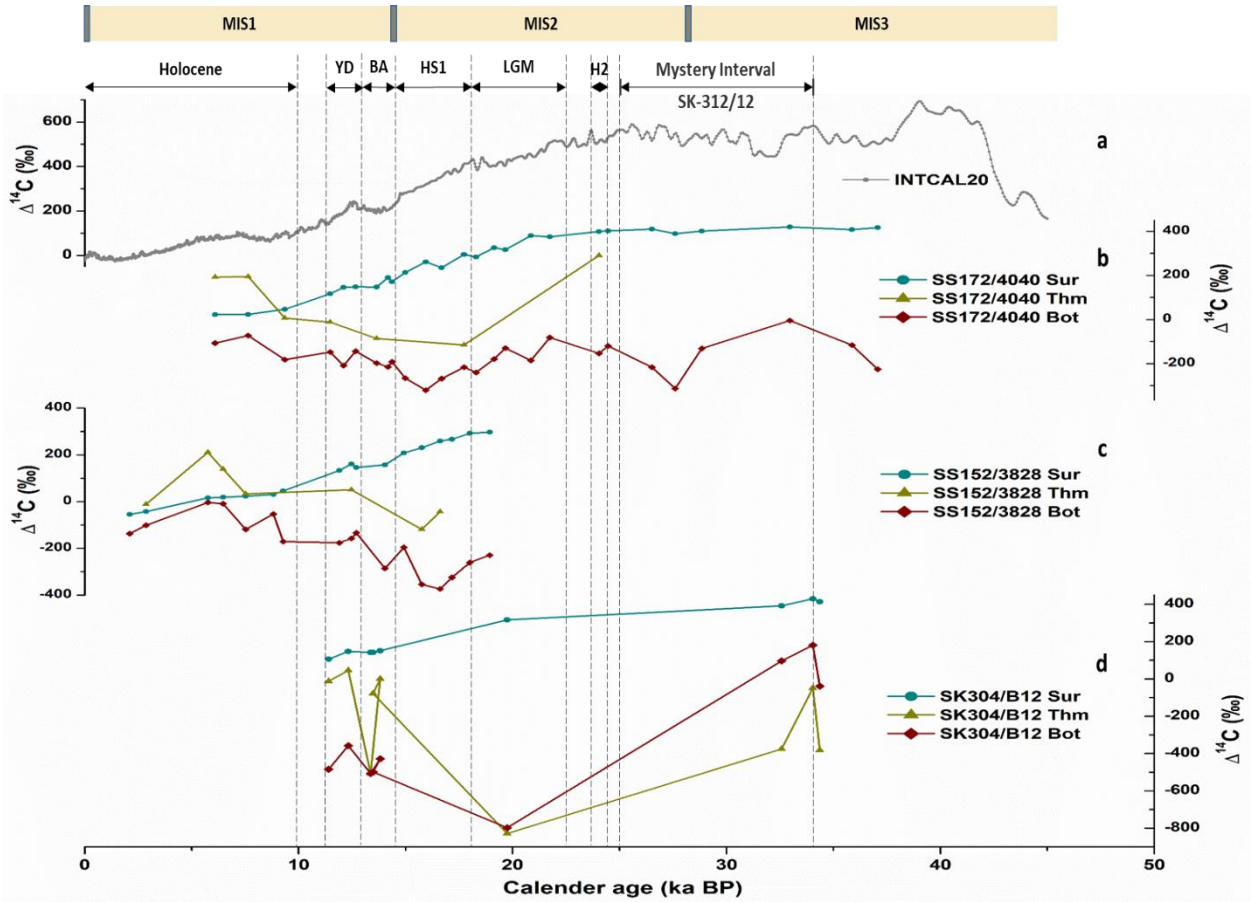

Figure 3.7: Surface ocean (Sur), thermocline (Thm) and bottom water (Bot) $\Delta^{14}C$ records from (b) core SS172/4040, (c) core SS152/3828 and (d) core SK304/B12 along with (a) the northern hemispheric atmospheric $\Delta^{14}C$ record ($\Delta^{14}CAtm$) (INTCAL20) (Reimer et al., 2020).

The magnitudes of the $\Delta^{14}C_{Thm}$ depletions from SK-312/12 are extremely high to be explained by any subsurface water mass processes like advective mixing, diffusive mass transfer and the aged southern oceanic source ventilation hypothesis. The only plausible mechanism can be attributed to a significant contribution of dead geologic carbon from any volcanic-hydrothermal origin. Available paleo-volcanic records from the tropical Indian ocean represent limited hydrothermal activities from the Carlsberg ridge (Panchang et al., 2007; Yu et al., 2018) on millennial time scales. Hydrothermal activities from the Central Indian Ridge (CIR) have been significant during the Holocene (~3-7 ka BP, (Lim et al., 2020)) and the last deglaciation (Lim et al., 2021). Paleo-volcanic events have also been reported from the Talus Tips site (16±2 ka BP, 22.7±3 ka BP and 52±5 ka BP) and the Sonne Field regions (18±2 ka BP and 12.5±1.5 ka BP) from MESO zone, Central Indian Ridge. These activities are however, episodic in nature with intermittent cessations rather than being continuous (Lalou et al., 1998).

The Reunion Hotspot located in the Reunion Island in the Mascarene Basin (Saint-Ange et al., 2013) (Fig. 3.3) continues to be active till date (Marty et al., 1993) since its timing of formation before 2.1 Ma (Rancon, 1985). Out of its two main edifices, i.e. the Piton des Neiges and the Piton de la Fournaise (Marty et al., 1993), the activity of Piton des Neiges apparently ended between 20-40 ka BP (Gillot and Nativel, 1982). The Piton de la Fournaise is still very active to date. However, it is characterized by frequent small volume eruptions (Peltier et al., 2009) due to its entire edifice being almost devoid of gas emanations and mineral springs (Marty et al., 1993). Another record of paleo volcanic-hydrothermal activity from the Indian Ocean has been reported by Carvallo et al., 2003 from the Amsterdam Island (77.3°E, 37.5°S) (Fig. 3.3), a structurally double-strato volcanic island. It has witnessed two transitional lava flow events estimating around 26±15 ka BP and 18±9 ka BP respectively. The location of this volcanic island lies in close latitudinal proximity of the SAMW/AAIW formation, making it countable as a possible hydrothermal source for the SK-312/12 $\Delta^{14}C_{Thm}$ depletion during the 25-34 ka BP Mystery Interval.

Among all the possible events discussed above, the 20-40 ka BP termination event of Piton des Neiges from Reunion Hotspot and the 26±15 ka BP lava flow event from the Amsterdam Island aptly coincide with the timing of the SK-312/12 Mystery Interval. Thus, either or both of these two events could have been the responsible source(s) of geologic dead carbon supply into the SK-312/12 thermocline during the SK-312/12 Mystery Interval. Additionally, the hydrothermal plume

excursions might have been associated with massive heat fluxes, thus undergoing extensive lateral advection (Massoth, 1994) followed by their transport into the EIO thermocline via SAMW/AAIW.

The paleo-volcanic events reported from the Central Indian Ridge have been excluded from possible source choices because of the reported episodic natures of the eruptions. However, lucid information regarding the accurate timings of paleo volcanic-hydrothermal eruptions are essential in order to obtain a clear understanding about the exact source and subsurface oceanic mechanisms of hydrothermal dead carbon supply into the EIO thermocline during this newly identified Mystery Interval.

3.6.2 The North Atlantic Climatic Tele-Connection during Heinrich 2

The $\Delta^{14}C_{Thm}$ record of SK-312/12 observes a steep rise at the ~24 ka BP boundary, coinciding with the timing of North Atlantic Heinrich 2 (H2) event (Fig. 3.4 and Fig. 3.6). This rapid rise in the $\Delta^{14}C_{Thm}$ value represents the termination of prevailing hydrothermal dead carbon supply into the SK-312/12 thermocline during the 25-34 ka BP Mystery Interval. The similarity in the timing of occurrence of H2 and the termination of hydrothermal source ventilation into the SK-312/12 thermocline, shows a clear climatic tele-connection between these two events. The H2 event has been reported to have strong tele-climatic influences over the tropical Indian Ocean through the slowdown of Atlantic Meridional Overturning Circulation (AMOC) and associated changes in the Hadley circulation resulting in the weakening of SWM and strengthening of NEM via southward displacement of the ITCZ (Godad et al., 2022). Studies have reported intensely reduced water mass conditions from the Arabian Sea thermocline (Pattan et al., 2017), reduction in supply of North Atlantic Deep Water (NADW) into the Indian Ocean bottom water (Bharti et al., 2022) and increased SST records from the ITF region (Levi et al., 2007) associated with the H2 climatic event. However, with limited available information, it is difficult to ascribe how the initiation of H2 event, subsequent AMOC slowdown, the southward displacement of ITCZ and the NEM intensification could play a significant role in restricting the hydrothermal source ventilation into the EIO thermocline at ~24 ka BP. The Heinrich 1 (H1) and Heinrich 3 (H3) events do not show any significant influence on the thermocline radiocarbon ventilation records.

During the MIS 3 to pre-LGM time period, the $\Delta^{14}C_{Thm}$ record of SK-312/12 is in complete contrast with the $\Delta^{14}C_{ML}$ and $\Delta^{14}C_{Atm}$ records (Fig. 3.6). This clearly indicates that the thermocline

was strongly decoupled from the surface mixed layer and the atmosphere during this period. However, the $\Delta^{14}C_{ML}$ variability was in well conjunction with the $\Delta^{14}C_{Atm}$ records. These observations are consistent with the earlier observations that have stated an early decoupling of Indian Ocean thermocline from the surface ocean during the MIS 3 compared to the Pacific (Skinner et al., 2015; Ronge et al., 2016) and the Atlantic (Skinner et al., 2010), which were still ventilating until the entire deep Southern Ocean cut-off from the surface during LGM.

3.6.3 Ventilation Records during LGM

The $\Delta^{14}C_{Thm}$ record from SK-312/12 shows an apparently coupled mixed layer and thermocline $\Delta^{14}C$ reduction but a decoupled atmospheric condition during the LGM (Fig. 3.4). Studies have showcased strong evidence of ocean acting as a sink of atmospheric CO_2 during the LGM (Skinner et al., 2017) thus, leading to increase in the surface and mixed layer $\Delta^{14}C$. However, reduction in the $\Delta^{14}C_{Thm}$ and subsequently in $\Delta^{14}C_{ML}$ from SK-312/12 during LGM, contradicts the above earlier notion. The contrary outcome strongly suggests the contribution of subsurface water mass influence. It appears that the LGM $\Delta^{14}C_{Thm}$ depletion was probably associated with the influence of a second phase of hydrothermal activity, caused by decompression melting of the uppermost mantle as a result of the LGM sea-level lowest stand (Stott and Timmermann, 2011), into the EIO thermocline. Again, the hydrothermal emanations could have undergone extensive lateral advections followed by their carriage via SAMW/AAIW into the SK-312/12 thermocline (as discussed in section 5.1). A coupled reduction in the $\Delta^{14}C_{ML}$ possibly resulted from the intensification of equatorial upwelling and associated mixing of the upper EIO caused by the strengthening of Wyrtki Jets during the LGM (Punyu et al., 2014). Among all the paleo volcanic-hydrothermal records discussed in section 5.1, the volcanic events from the Sonne Field regions (18±2 ka BP) and the Talus tips site (16±2 ka BP, 22.7±3 ka BP) from the MESO zone, CIR, the 18±9 ka BP lava flow event from the Amsterdam Island, and the termination of Piton des Neiges, Reunion Island (20-40 ka BP) appear to be among the possible contributing source(s) of geologic dead carbon supply resulting in the $\Delta^{14}C_{Thm}$ depletion of SK-312/12 during LGM.

3.6.4 Deglacial Thermocline Ventilation

The $\Delta^{14}C_{Thm}$ records from the AS and Baja, California show similar range of variability with core SK-312/12 during the last ~24 ka (Fig. 3.6). Based on the inferences of Bryan et al., 2010, it is concluded that the overall similarity in the records of the AS, the Baja, California and

the SK-312/12 possibly indicates a similar mechanism operative in these associated regions, and that the processes involved are most likely of oceanographic origin rather than geologic. The core SK-312/12 records an increase in the $\Delta^{14}C_{Thm}$ during the H1, similar to the AS records and the multi-core records from Baja, California. As per Bryan et al., 2010, these early deglacial observations are primarily attributed to the advection of ^{14}C-depleted deep southern-ocean water via SAMW-AAIW into the low latitude intermediate waters during the last deglaciation. The $\Delta^{14}C_{Thm}$ variations from core SK-312/12 between YD to early Holocene (~9 ka BP) are quite similar between the Baja, California and the SK-312/12 records (Fig. 3.6). A negative $\Delta^{14}C$ excursion observed in the YD record of SK-312/12 is also apparent in the Baja, California record along with a distinct $\Delta^{14}C$ minima at the YD termination. However, such a $\Delta^{14}C_{Thm}$ minimum is absent from the AS records. Marchitto et al., 2007 has attributed the YD $\Delta^{14}C$ depletion from Baja, California to be the result of SAMW-AAIW influence. The absence of $\Delta^{14}C_{Thm}$ minimum from the AS record (Fig. 3.6) has been attributed to the local processes of differential water mass mixing or upwelling by Bryan et al., 2010. The similar variation pattern observed between core SK-312/12 and Baja, California record between YD to early Holocene possibly indicates that both the regions were under similar oceanographic influences where a $\Delta^{14}C$ depletion (or enrichment) might have been associated with an increased (or decreased) SAMW/AAIW ventilation. Additionally, the AS and the central EIO might have remained uninfluenced by poor or limited ventilations of the ^{14}C depleted SAMW-AAIW into the EIO thermocline following the YD time period.

Detailed investigations of past ^{14}C records are necessary to obtain a clear picture on the millennial paleo ventilation status of the tropical Indian Ocean thermocline. Accurate timings of paleo volcanic-hydrothermal activities along with their extensive regimes of influences need to be defined in order to obtain a better understanding of the exact source and transport mechanisms of hydrothermal dead carbon supply into the EIO thermocline. The North Atlantic climatic influence on the hydrothermal source termination into the EIO thermocline during the H2 event requires further attention of research in order to figure out the exact paleoceanographic and paleoclimatic mechanisms associated in driving the North Atlantic tele-climatic influence into the Indian Ocean thermocline hydrothermal ventilation.

The outcome of the present study along with the recent discoveries compel the modern oceanographic research community to acknowledge the role of geologic carbon as a vital source

of depleted radiocarbon concentrations in the subsurface ocean and to consider its potential contributions in the geochemical evolution of the upper oceanic and atmospheric radiocarbon dynamics.

3.7 Conclusion

The $\Delta^{14}C_{SW}$ records from the upper ocean have been reconstructed from the western central EIO over the last 44 ka as a maiden attempt from an open ocean thermocline. An extremely depleted thermocline radiocarbon interval has been identified during 25-34 ka BP, named as the MIS 3-MIS 2 transition 'Mystery Interval'. Contemporaneous volcanic activities reported from the Reunion hotspot and/or the Amsterdam Island appear to be the responsible source(s) of geologic dead carbon supply resulting in anomalous radiocarbon depletion in the EIO thermocline. A second phase of hydrothermal activity is also evident during the Last Glacial Maximum (LGM) possibly resulted from the enhanced volcanic-hydrothermal activity triggered by the glacial sea level low-stand. The timing of hydrothermal source supply termination into the EIO thermocline following the Mystery Interval at ~24 ka BP, exactly coincides with the North Atlantic H2 event. This indicates a strong tele-connection of North Atlantic climatic variability on the hydrothermal ventilation in the EIO thermocline. However, the exact mechanism associated with the initiation of H2 event, the AMOC slowdown and the southward shifting of ITCZ on the hydrothermal supply termination in the EIO thermocline, remains a matter of further investigation. Unlike the H2, the H1 and H3 appear to have little influence on the EIO thermocline ventilation.

The 'Mystery Interval' during 25-34 ka BP represents a strongly decoupled EIO thermocline from the corresponding mixed layer and the atmosphere, unlike the Pacific and the Atlantic. The atmosphere during the LGM, remained decoupled from the surface ocean and the thermocline whereas, the mixed layer and the thermocline were mutually coupled as a result of the upper oceanic mixing caused by the intensification of equatorial upwelling over the EIO. The deglacial thermocline radiocarbon depletion is primarily associated with the aged supersaturated southern ocean sourced ventilation into the EIO thermocline via SAMW-AAIW.

Chapter 4

Quantitative Reconstruction of Equatorial Indian Ocean Paleothermocline using Planktonic Foraminiferal Mg/Ca Records

4.1. Introduction

The oceanic thermocline plays a primary role in the upper ocean-atmospheric heat and gaseous exchange processes and helps provide the long term climatic stabilities by transferring the surface climatic anomalies into the subsurface and deep oceanic reservoirs (Schott et al., 2009; Pagani et al., 2010). It provides a suitable platform for microhabitat growth through necessary upper oceanic water mass stratifications. The thermocline witnesses major transitions in the primary physical and chemical oceanic parameters such as the density, salinity, oxygen ion concentrations and the primary productivity due to the strong variations in the processes that are directly or indirectly linked to the oceanic temperature conditions (Longhurst et al., 1995; Shapiro, 2009; Schmitz, 2018). The EIO thermocline is strongly associated with the regional (Du et al., 2020) and global climatic variabilities through the inter-basinal (Ummenhofer et al., 2017) and interhemispheric (Nilsson-Kerr et al., 2019) climatic transfers and changes in its mean thermal conditions. Understanding the characteristic evolution of the EIO thermocline is thus crucial for the regional and global paleo oceanographic and paleo climatic reconstruction studies.

4.2. Motivation and Objectives

Despite its unique importance, paleothermocline reconstruction studies are extremely limited from the EIO region due to the major technical and methodological challenges leading to a substantial gap in the understanding of the millennial scale evolution of the Equatorial Indian Ocean paleothermocline and its implications on the regional and global paleoclimatic variabilities. A limited number of studies have been carried out so far (Mohtadi et al., 2010, Kwiatkowski et al., 2015 and Pang et al., 2021, and by Rippert et al., 2015) from the coastal EIO boundaries possibly to avoid the risk of sample abundancies. However, such a common approach leads to a strong possible interference of the local climatic variabilities in overprinting the global climatic signatures resulting in indiscrete interpretations and scientific assessments. Additionally, all the studies have relied upon a single planktonic foraminiferal representative for the paleothermocline leading to the complete underestimation of the plaeoclimatic significances of the intra-thermocline variabilities. The obtained results have shown discrepancies in the common understanding of the origin and distribution of the deglacial Antarctic Intermediate Water masses over the upper EIO region. The results also witness contrasting thermocline variation patterns leading to inconclusive statements

regarding the appropriate sources of EIO thermocline water circulations during the glacial-deglacial time periods.

The existing limitations set the primary motive for the present study with the objectives to carry out a detailed paleothermocline reconstruction from an open oceanic region of the EIO using the Mg/Ca records of the depth specific planktonic foraminifers extending from the surface to the lower thermocline. The study aims at obtaining a quantitative reconstruction of the EIO paleothermocline accounting for the intra-thermocline variabilities, and understanding the millennial scale evolution of the upper EIO thermal structure and implications towards the regional and global scale paleoclimatic variabilities.

4.3. Results: Paleotemperature Reconstructions

Paleotemperature records were reconstructed using the species-specific Mg/Ca vs Temperature calibration equations as mentioned in section 2.8.2. The average error (±1σ) in the paleotemperature reconstruction records for *G. ruber* (s.s.) and *G. siphonifera* is ±1.1°C and for *T. sacculifer* (w/s) and *G. menardii* is ±1.0°C. Paleo temperature records obtained for *G. ruber* varies between 24.3°C to 29.2°C, with a mean of 26.2°C. Paleo temperature record for *T. sacculifer* (w/s) varies between 22°C to 27.1°C, with a mean of 24.3°C. Paleo temperature record for *G. siphonifera* varies between 19.8°C to 24.8°C, with a mean of 22. °C. Paleo temperature record for *G. menardii* varies between 15.8°C to 22.8°C, with a mean of 18. °C (Fig. 4.1 and Table B1).

The abbreviations AML, MLD, uThm and lThm have been used to address the corresponding oceanic depths represented by the indivisual ACDs of *G. ruber* (s.s.), *T. sacculifer* (w/s), *G. siphonifera* and *G. menardii* in the SK-312/12 thermocline respectively. The thermal segments between AML to MLD, MLD to uThm and uThm to lThm are addressed as S1, S2 and S3 respectively. Paleotemperature reconstruction studies commonly consider the temperature of the ML as an integral part of the thermocline structure representing the upper boundary limit of it. The term thermocline will thus be alternatively used to address the complete upper oceanic thermal structure in the upcoming sections of this study as well.

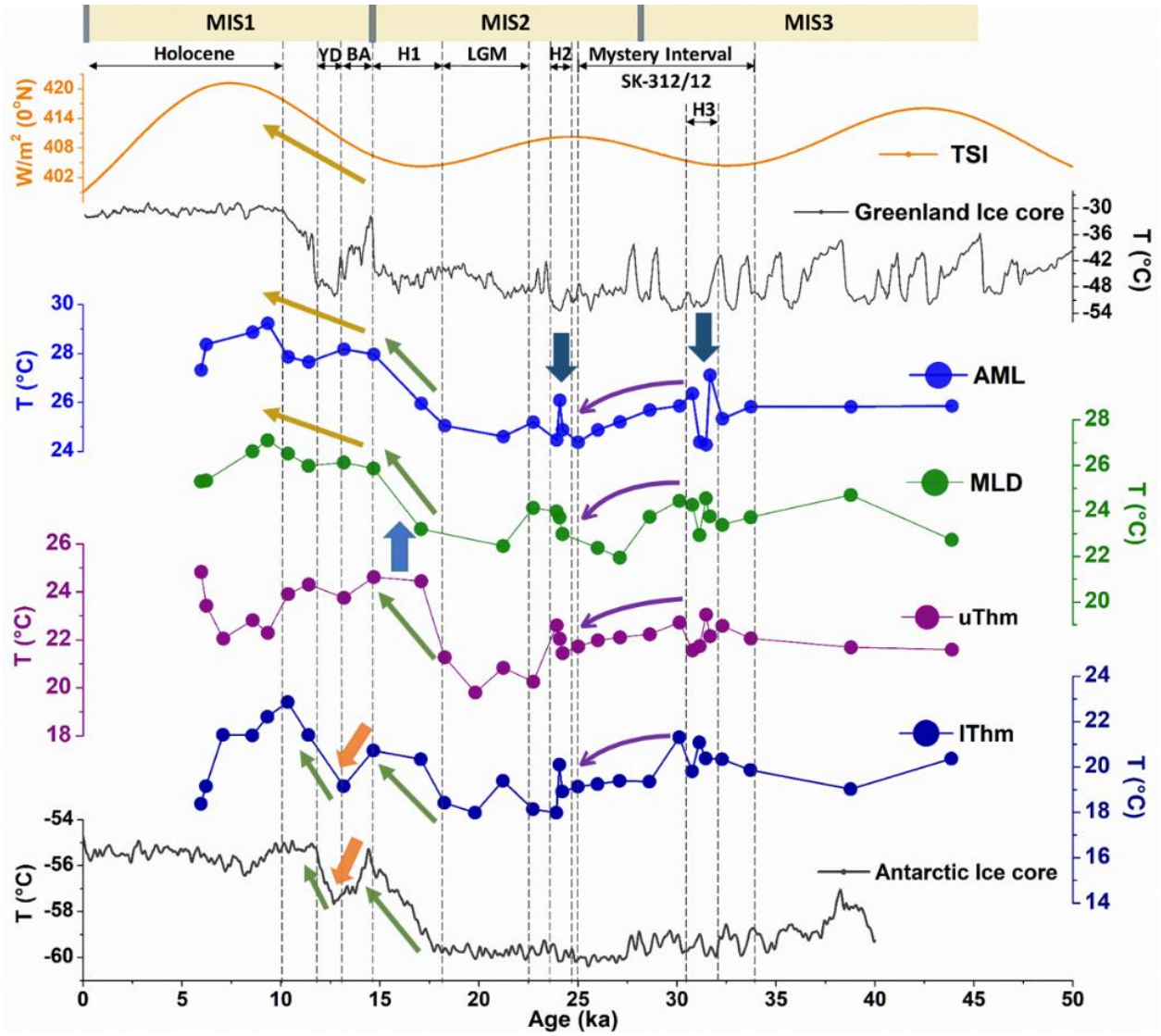

Figure 4.1: Paleotemperature records from SK-312/12 thermocline: (c) Mixed Layer Depth (MLD), (d) upper Thermocline (uThm), (e) main Thermocline (mThm) and (f) lower Thermocline (lThm). Along with (a) the Total Solar Insolation (TSI at 0°N, 60°E), (b) North Atlantic ice-core GISP2 and (g) the Antarctic ice-core EDC.

4.4. Discussions

4.4.1 Paleotemperature Variability

Fig. 4.1 represents the paleotemperature records from SK-312/12 thermocline. Paleotemperature records show minimum variability during MIS3 compared to MIS1 and MIS2. The AML, the upper and the lower thermocline show minimum temperature variability during 25-34 ka, the period of hydrothermal 'Mystery Interval' (Chapter 3). Distinct shifts in temperatures are observed

at all depths during H2 and H3 representing strong tele-climatic influences of North Atlantic climatic variability over the EIO regional climate. The LGM records an overall cooling in thermocline from mixed layer to lower thermocline. A continuous warming was observed in mixed layer (ML) from the early deglaciation period, followed by cooling in the latter part of the Holocene. The uThm and the lThm however show mutually opposite thermal patterns during the mid-Holocene.

Average temperatures during different paleoclimatic intervals are calculated for each foraminiferal depth (Table B2). Paleotemperature variations at different planktonic foraminiferal depths with respect to the present day record are presented in Table B3. The upper oceanic thermal profile of SK-312/12 remained cooler than present from the mid MIS3 to LGM at all depth sections. Around ~3.5 ºC of cooling is observed in the ML and ~2.3 ºC cooling is observed in the uThm during the mid-MIS3. The ML was 3.5-4 ºC cooler during the early MIS2 with ~1-2 ºC cooling observed in the thermocline. The LGM recorded a strong cooling by 4-4.5 ºC in the ML, around ~3.5 ºC and ~1.8 ºC cooling in the uThm and the lThm respectively. Around ~1 ºC and 1.3 ºC cooling was observed at MLD and lThm respectively during the BA/ACR. The uThm was cooler by ~1.7 ºC whereas the lThm was warmer by 1.3 ºC during the early Holocene. The mid-Holocene recorded 1-2 ºC cooling in the ML and ~1.6 ºC cooling in the lThm, whereas, the uThm remained similar to the present day condition.

4.4.2 Paleoclimatic Implications and the Climatic Tele-connections

The variational pattern remained similar in mixed layer (T_{MLD}) to that of AML (except H2, which has been noticed in temperature record discussions) indicating that the MLD remained coupled and mixed with the AML throughout the paleo record. Relative differences in the paleotemperature records between successive thermal depths is plotted in Fig. 4.3. An increase in the magnitude of relative paleotemperature difference would indicate an increase in the slope and stratification of the corresponding thermal segment. The s1, s2 and s3 represent the magnitudes of the individual slopes of the thermocline segments S1, S2 and S3 respectively.

Paleotemperature records in AML (T_{AML}) and uThm (T_{uThm}) remained more or less constant, whereas, it increased in MLD (T_{MLD}) and slightly decreased in lThm (T_{lThm}) during the mid-MIS3 (Fig. 4.1). The increase in T_{MLD} indicates a possible deepening of the MLD resulting in a

thickening of the ML due to increased surface mixing. The lThm possibly observed a minor shallowing during this period.

Strong N. Atlantic climatic influences are observed during the H3 and H2 cold-events throughout the SK-312/12 thermocline representing a primary control of the northern high-latitudinal tele-climatic connectivity. The degrees of the tele-climatic influences are higher over the surface ocean compared to the deeper thermoclines. The intensity of H3 is apparently pre-dominant than the corresponding tele-climatic influence of H2. It is important to notice that the signature of H3 is indistinguishable in the radiocarbon records of the SK-312/12 thermocline (Fig. 3.4, Chapter3). The primary cause of such differential proxy observations is possibly attributed to the differential proxy response of the hydrothermal influx to the respective proxy parameters. Thus, the hydrothermal influx could have produced significant contributions to the radiocarbon variability through abundant dead carbon supply, whereas, its relative contributions on the sea water Mg/Ca was comparatively much more limited in order to overcast the tele-climatic cooling produced by the Heinrich event.

Paleotemperature records decreased throughout the SK-312/12 thermocline during LGM primarily attributed to the increased global cooling added with the cold SAMW–AAIW contributions (Pahnke et al., 2008; Jung et al., 2009; Mahesh and Banakar, 2014). An intermittent punctuation in the thermocline temperature record is possibly attributed to the intermittent weakening of the glacial winters (Mahesh and Banakar, 2014). Paleotemperature variability during H1 appears to be strongly associated with the Antarctic climatic reversal through enhancement in the early degalcial SAMW-AAIW influxes into the EIO thermocline as discussed in Chapter3 (section 3.1). Strong mixing is observed at the MLD resulting from the possible upwelling of the SAMW-AAIW carrying the Antarctic climatic signatures into the surface mixed layer of the EIO. The observations provide strong agreement to the earlier upper oceanic paleo climatic reconstruction studies as well (Bryan et al., 2010; Kiefer et al., 2006; Mohtadi et al., 2010; Naidu and Govil, 2010; Visser et al., 2003). The Antarctic climatic variability continued to influence the lThm temperature during the early MIS1 resulting in a subsequent decrease during the BA/ACR and an increase up to the pre-Holocene. However, its influence on the uThm was negligible and almost absent on the ML. The stratification in S3 thus increased slightly during BA/ACR and followed a strong decrease resulting in a well-mixed water mass condition prior to Holocene.

Paleotemperature records of the ML (AML and MLD) were primarily under the influence of the Total Solar Insolation (TSI) from the early MIS1 up to the Holocene time period. Stratification in S1 thus decreased slowly in S1 during the early MIS1 up to the pre-Holocene, whereas, the S2 observed an increase in stratification subsequently. Stratification within the ML increased slowly during the Holocene due to the relatively higher degree of warming in AML compared to the MLD.

The results discussed above clearly represent the interhemispheric tele-climatic controls on the millennial scale climatic evolution of the EIO thermocline. The North Atlantic climatic variability was more persistent during the H2 and H3, whereas, the Antarctic climate dominated from the early deglaciation to early MIS1 time periods.

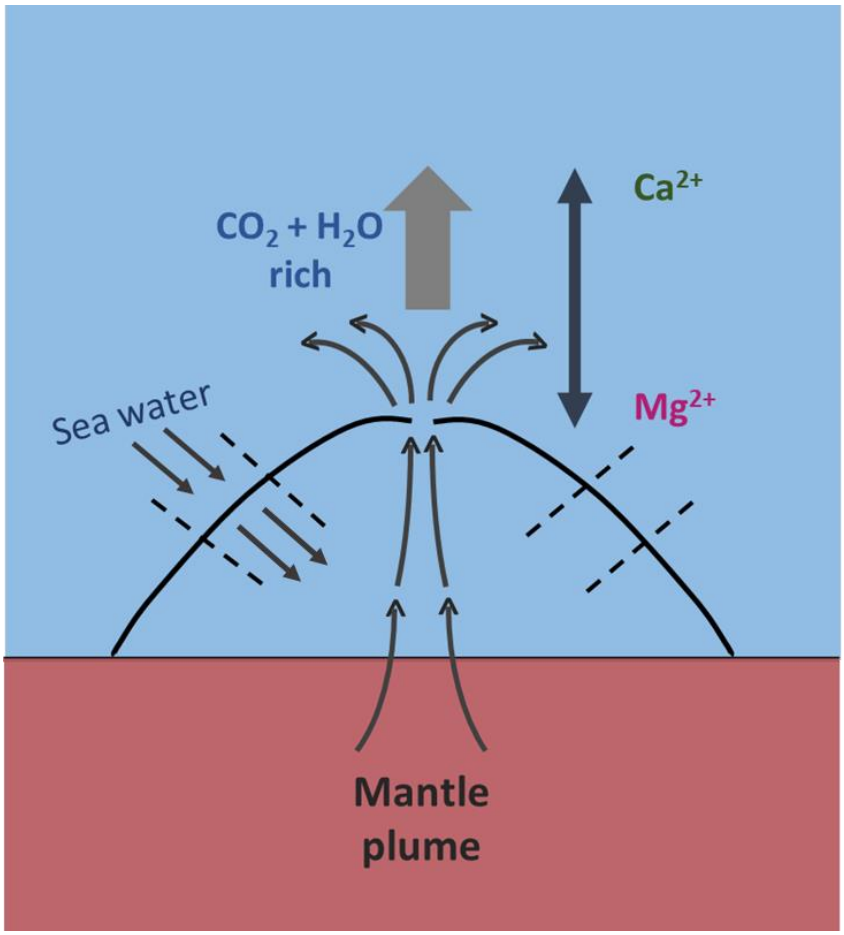

Figure 4.2: Schematic of Hydrothermal Flux Release during Volcanic Exhumations.

4.4.3 The Hydrothermal Mystery Interval

Radiocarbon evidence of hydrothermal influence in to the SK-312/12 thermocline during the MIS3-MIS2 transition has been discussed in detail in the Chapter 3. The current section investigates the influences of the earlier examinations on the sea water paleotemperature records. The paleotemperature reconstructions obtained from the SK-312/12 paleothermocline strongly supports the earlier inference of an existing hydrothermal 'Mystery Interval' during the MIS3-MIS2 transition (Fig. 3.4 and Fig. 3.6) based on the corresponding Mg/Ca variation records of the associated planktonic foraminifers. During the process of a volcanic-hydrothermal release, the hydrothermal fluids react with the basaltic magma exchanging the seawater Mg with the basaltic Ca into it (Seyfried and Bischoff, 1981; Berndt et al., 1988). The process thus decreases the Mg and increases the Ca concentration in the hydrothermal fluids resulting in a significant reduction in its corresponding Mg/Ca ratio. Mixing of these hydrothermal fluids with the sea water will lead to a subsequent reduction in the sea water Mg/Ca ratio which will later be reflected in the foraminiferal shells calcifying under these water mass environments. The Mg/Ca records from all the four planktonic foraminifers from SK-312/12 show a gradual decrease during the hydrothermal 'Mystery Interval', neglecting the H3 climatic perturbations, between 25-34 ka. The pattern of variation is very much identical in *G. ruber* (AML), *G. siphonifera* (uThm) and *G. menardii* (lThm) indicating a constant process influencing the complete upper EIO at SK-312/12 during this time period. However, a mixing of water mass within S2 (Fig. 4.1 and Fig. 4.3) is observed during the onset of MIS2 (~27 ka) leading to a relative decrease in T_{MLD}, which could be considered as a possible outcome of strong hydrochemical alterations of the sea water caused by the upwelling hydrothermal fluids at the transitional boundary of the upper thermocline. Observations by Massoth, 1994 provide mechanistic evidences of the hydrothermal fluids to reach the shallow oceanic depths through extensive lateral advections associated with high heat fluxes.

Radiocarbon records could not confirm the complete upper oceanic hydrothermal intervention during the 'Mystery Interval'. However, the Mg/Ca records of the upper EIO provide possible evidence for the same. Considering a complete upper oceanic perturbations of the hydrothermal influxes, it can be suggested that the absence of hydrothermal signatures in the mixed layer radiocarbon records is possibly associated with a contemporaneous atmospheric moderation through constant ocean-atmospheric radiocarbon transactions during this time period.

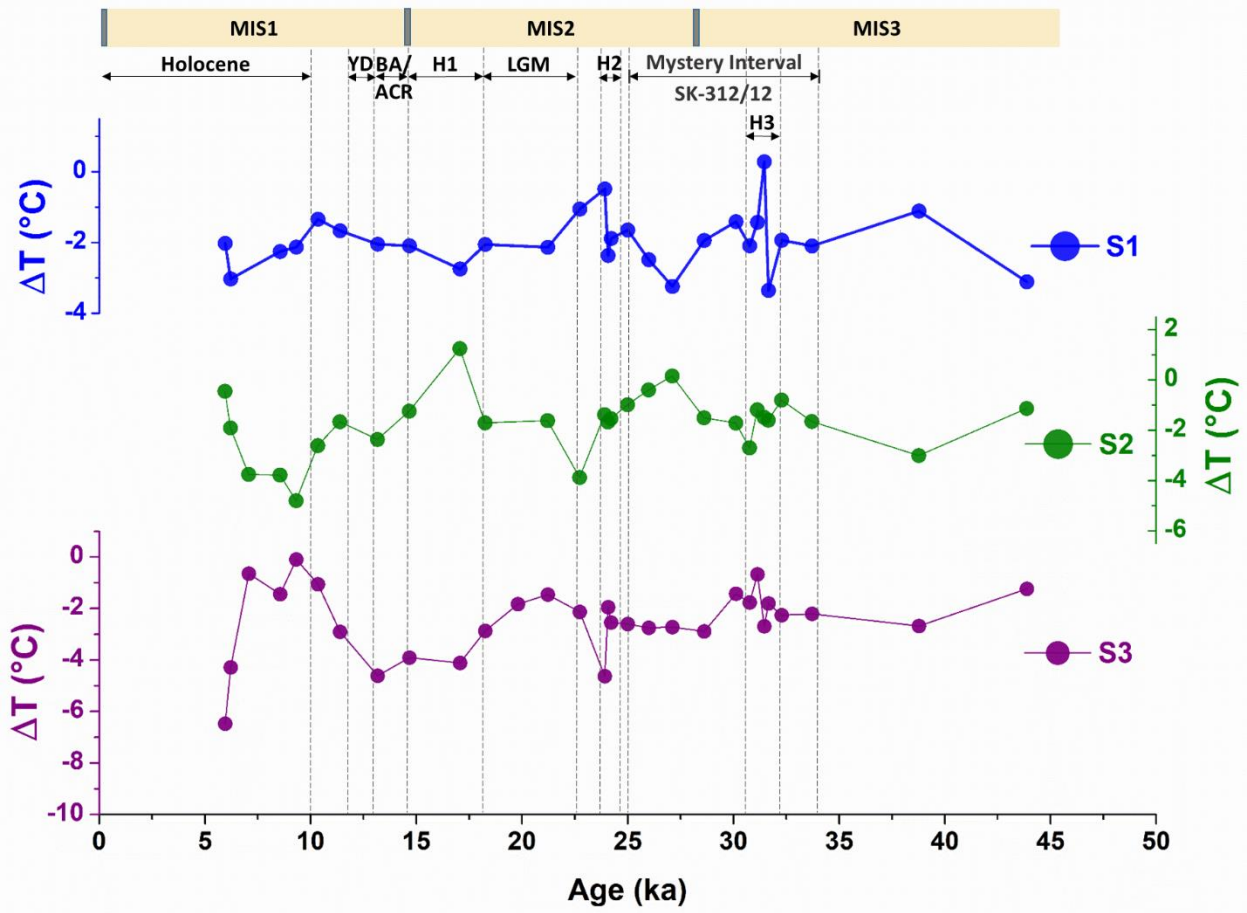

Figure 4.3: Thermocline stratification. (a) S1: Temperature difference between MLD and uThm, (b) S2: Temperature difference between uThm and mThm, and (c) S3: Temperature difference between mThm and lThm.

4.4.4 The Holocene Thermocline Variability

Paleotemperature records from uThm and lThm observed strong variations during the mid-Holocene associated with a rapid increase and decrease in T_{uThm} and T_{lThm} respectively. Such a variation is quite abnormal to the existing upper oceanic water mass conditions over the EIO in association with the prevailing high-latitude climatic systems (Fig. 4.1). An attempt was made to compare the Holocene thermocline paleotemperature variations with the available ITF strength variability records (Fig. 4.4). The comparisons show an interesting match between the T_{lThm} and the peak ITF strength during the early Holocene (~10 ka). The observations provide strong correspondence with the modelled outcomes by Kuhnt et al., 2004 that suggests an increase in the ITF strength following the interglacial sea-level rise resulting in a reduced proportion of Antarctic Intermediate Water mass contributions. Rippert et al., 2015 in their upper oceanic thermocline

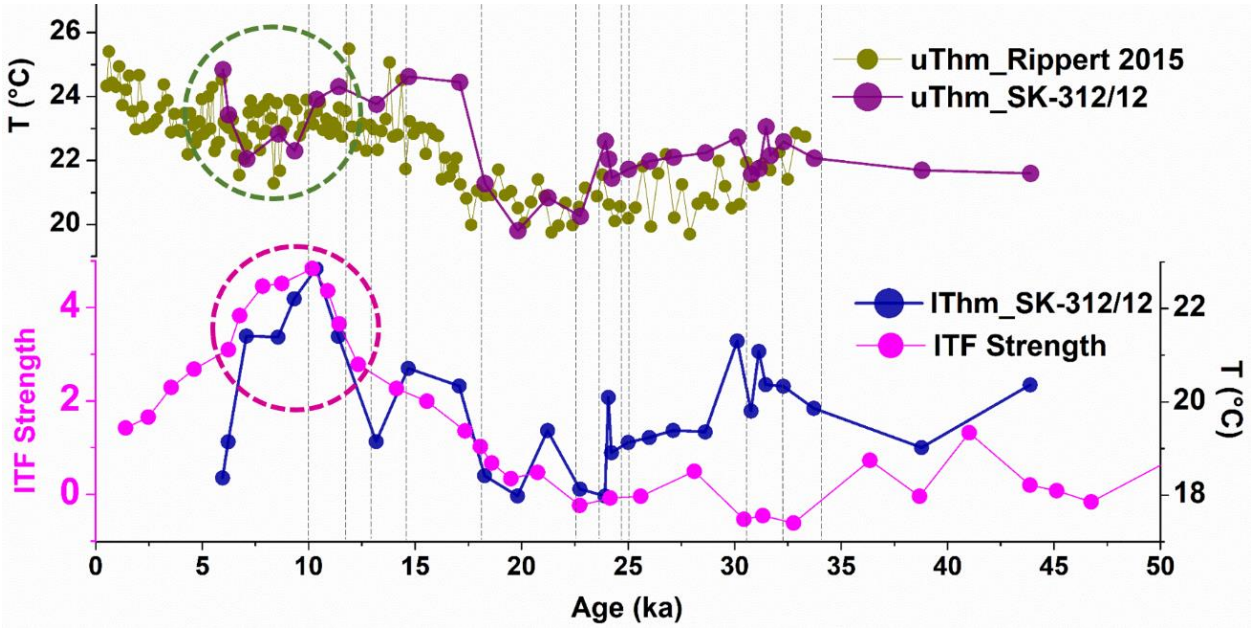

Figure 4.4: Comparison with the Indonesian Through Flow (ITF) strength variability and the upper thermocline paleotemperature records from Tanzania coast by Rippert et al., 2015.

reconstruction study from off Tanzania coast in the western EIO (WEIO) have suggested an increased Red Sea Water contribution into the upper thermocline through the similar mechanism as proposed by Kuhnt et al., 2004. A comparison of the Holocene records from the uThm of SK-312/12 show a possible match with the corresponding records reported by Rippert et al., 2015. The combined interpretations of the Holocene thermocline temperature variabilities from the SK-312/12 sediment core possibly suggest an increase in the production and distributions of the regional intermediate water sources into the EIO during the early Holocene interglaciation and warming. The ITF was the predominant source of lower thermocline water mass ventilation whereas the RSW was the leading source for the upper thermocline of the EIO.

4.4.5 Temporal Evolution of SK-312/12 Paleothermocline

Fig. 4.5 represents the fundamental thermal structures observed by an individual oceanic thermocline, named as type I, type II and type III. The type I represents a straight structure with a constant downward slope. The type II represents a net concave up structure whereas the type III represents a net convex up thermal profile. A type I thermocline structure would indicate an ideally stable thermal condition with no net vertical water mass advections. Whereas, a type II structure will reflect a net downwelling and water mass mixing at the upper sections of thermocline or a net

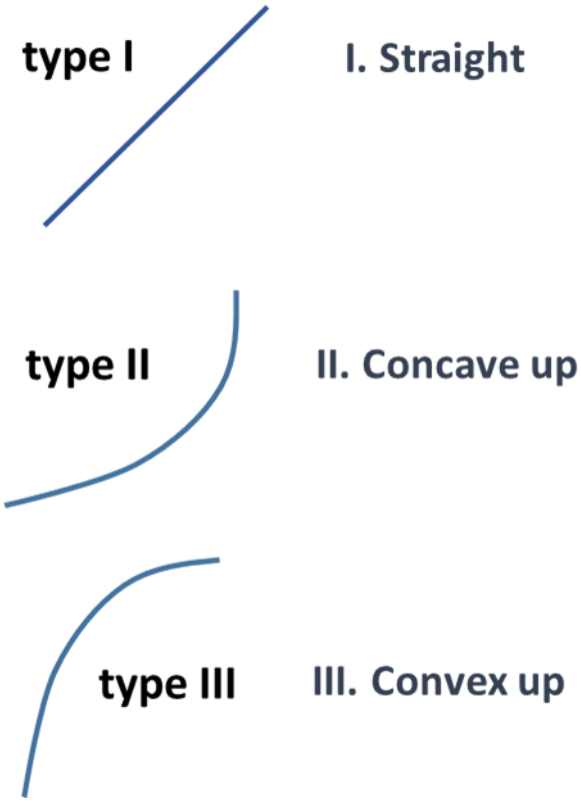

Figure 4.5: Thermal structures of thermocline stratification.

upwelling and water mass stratification at the lower section of it. A type III structure would subsequently indicate a net upwelling and water mass stratification in the upper thermocline section or a net downwelling and water mass mixing in the lower section of it.

Paleotemperature records corresponding to the characteristic millennial paleoclimatic intervals were averaged out and plotted in Fig. 4.6 for understanding the temporal evolution of the SK-312/12 paleothermocline and the paleoclimatic implications of the thermocline inclination variabilities. The present-day annual mean temperature profile over SK-312/12 (WOA2018) is also plotted for a relative structural assessment. The observations indicate an overall type I thermocline inclination existing during the MIS3, H3 and LGM primarily associated with more or less uniform upper EIO cooling. Type II structural inclination is observed during H2 and BA/ACR. The nature of the structural inclination of thermocline during the H2 is primarily associated with increased surface oceanic cooling compared to the deeper thermocline. Whereas, the structural inclination during BA/ACR is caused by selective lower thermocline cooling by the SAMW-AAIW. Intra-thermocline mixings are observed during H1 and early MIS2 associated with intra-thermocline upwelling. The differential inclinations in the upper and lower thermocline sections

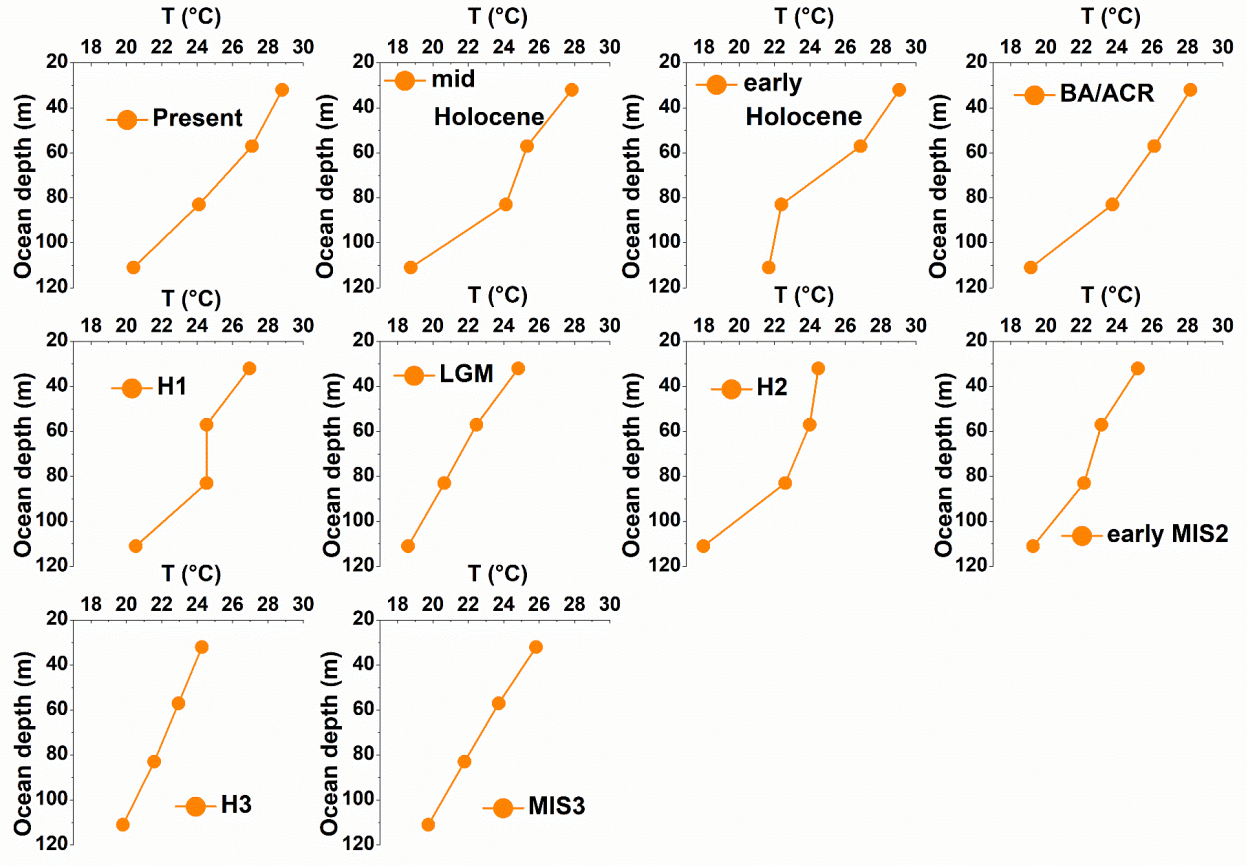

Figure 4.6: Temporal evolution of SK-312/12 paleothermocline.

during the early Holocene and the mid Holocene are characterised by the ITF and RSW influx variabilities. The present-day thermocline observes a close type I structural pattern with a slightly reduced ML stratification possibly being attributed to the increase in the mean global oceanic temperature associated with the increasing global warming. No type III structure is observed within the last 44 ka paleothermal history of the SK-312/12 thermocline.

Additional investigations are required to understand the mechanisms associated with the differential dominance of interhemispheric North Atlantic-Antarctic climatic shifts over the EIO paleoclimate. Extensive multi-species reconstructions are necessary to obtain more complete thermal profiles to better understand the subsurface and deep water paleotemperature and water mass variabilities. Better proxy studies are necessary to understand the source and the mechanism of transport of the hydrothermal influx during the 'Mystery Interval' and its contributions to the global atmospheric carbon dynamics.

4.5 Conclusion

A quantitative reconstruction of the EIO paleothermocline has been carried out as a maiden attempt from an open Indian Oceanic region using the Mg/Ca records of four different depth specific upper oceanic planktonic foraminifers. The results are compared with the contemporaneous regional and global paleoclimatic records to understand the broader implications of the thermal evolution of the upper EIO and its critical climatic tele-connectivities. Global climatic tele-connections of the North Atlantic and the Antarctic paleoclimate have been observed on the EIO paleothermocline. The North Atlantic climate predominates during the H2 and H3 events during the glacial period, whereas, the Antarctic climatic influence predominates during the deglacial period, especially in the lower thermocline region. Strong intra-thermocline mixings are evidenced during the H1 and early MIS2 period associated with intra-thermocline water mass upwellings. Inter-basinal water mass ventilations and climatic transfers are observed during the Holocene, with strong enhancement in the ITF strength variability into the lower thermocline of western EIO. A contemporaneous increase in the RSW water mass production is also evidenced within the upper thermocline region.

Chapter 5

Paleosalinity Reconstructions and Paleoceanographic Evolution of the Upper Equatorial Indian Ocean

5.1. Introduction

The oceanic salinity represents the total amount of dissolved salt concentrations present within the sea water. In modern oceanographic studies, the sea water salinity is represented in terms of the Practical Salinity Unit (PSU) derived from the electrical conductance of a sea water parcel obtained during the CTD cast operations. Variations in the sea water salinity is primarily governed by the fundamental hydro-climatic processes of Evaporation-Precipitation (Craig and Gordon, 2013), diffusion and advective water mass transfers (Thirumalai and Richey, 2016) like upwelling, downwelling and external mass mixings (Craig and Gordon, 1965; Clark and Fritz, 1999). Paleo salinity reconstruction studies thus provide significant implications towards the evolutions of various surface and subsurface paleooceanographic and atmospheric processes along with their broader global scale paleoclimatic implications (Elderfield and Ganssen, 2000; Benway et al., 2006; Banakar et al., 2010a).

The salinity of the sea water (S_{SW}) observes strong empirically linear relationship with the oxygen isotopic composition of the corresponding water mass ($\delta^{18}O_{SW}$), since both of the parameters are controlled by the common ocean-atmospheric and hydrologic processes. Variations in the salinity of the mixed layer is primarily determined by the net Evaporation-Precipitation (E-P) balance taking place at the surface under a given in-situ water mass condition. An increase in the evaporation increases the S_{SW} as well as the $\delta^{18}O_{SW}$, whereas, an increase in precipitation will reduce both of the associated parameters. The salinity of the intermediate and deep ocean is primarily influenced by the advective ventilation of the corresponding depth sources. A relatively minor contribution is provided from the overlying surface ocean through vertical downwelling.

5.2. Motivation and Objectives

The hydrology of the upper EIO represents widespread implication towards the regional and global climatic variabilities by providing major controls over the atmospheric and hydrologic cycles through coupled upper ocean-atmospheric feedback mechanisms and changes in its mean thermal conditions (Saji and Yamagata, 2003; Held and Soden, 2006; Vecchi and Soden, 2007). Paleosalinity reconstruction studies from the EIO paleothermocline is however absent except for the one from the south-west Sumatra coast form the WEIO by Mohtadi et al., 2010b. This study is limited to the single species representation of the thermocline leading to complete underestimation of the paleoceanographic and paleoclimatic significances of the intra-thermocline variabilities. The

near coast location also poses strong limitations of the local salinity perturbations leading to possible scientific misinterpretations on the associated regional and global scale ocean-atmospheric and climatic variabilities. The study additionally lacks appropriate explanation for the source of glacial-deglacial paleothermocline variabilities as well. The existing limitations clearly advocate for a potential requirement of a detailed paleosalinity reconstruction study from an open oceanic thermocline over the EIO in order to bridge the existing gap in the scientific understanding of the millennial scale evolution of the upper ocean-atmospheric and climatic variabilities operating over the glacial-deglacial time periods.

The primary objectives of the present study were to obtain a quantitative paleosalinity reconstruction from the upper EIO and understanding the regional and global implications of the surface and sub-surface paleooceanic-atmospheric and hydro-climatic processes operating over the EIO region.

5.3 Present-day Salinity Profile over SK-312/12

Fig. 5.1 represents the annual mean salinity profile obtained from the World Ocean Atlas 2018 (WOA18) dataset, over the SK-312/12 study location. The general pattern of an oceanic salinity profile over an equatorial region shows maximum magnitude in the surface ML followed by a gradual decrease into subsurface deeper oceanic depths. In addition to a gradual decrease observed at the sub-thermocline depths, the present-day salinity profile over SK-312/12 represents an increased salinity protrusion in the sea water salinity (S_{SW}) between the lower ML and the upper uThm depths. This increased salinity protrusion is primarily attributed to the southward propagation and influx of the Arabian Sea High Salinity Water (ASHSW) into the subsurface EIO depths after its production in the northern Arabian Sea (AS) (section 1.3.2). The protrusion results in the development of a characteristic tongue like shape in the vertical S_{SW} profile, called as the ASHSW tongue. Predominant influx of ASHSW takes place around the MLD and the uppermost section of the uThm, below which there is a gradual decrease in the S_{SW} following gravitative settlement.

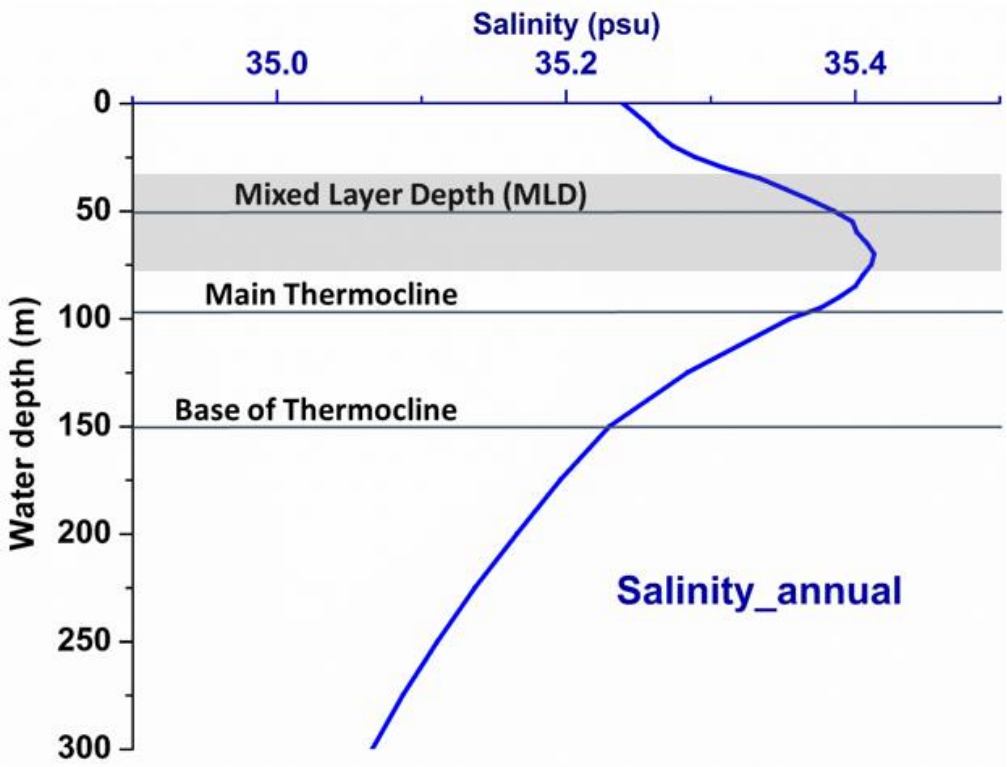

Figure 5.1: Present-day annual mean salinity profile (WOA18) over SK-312/12.

5.4 Paleosalinity Reconstruction

The paleosalinity records from the EIO paleothermocline were obtained following the approach described in Chapter 2 under section 2.9. At first the $\delta^{18}O_{SW}$ records of the past oceanic water mass were reconstructed using the foraminiferal Mg/Ca derived paleo temperature records (T_{SW}) combined with the corresponding $\delta^{18}O_f$ records (Fig. 5.2, Table C1-C4) obtained from the oxygen isotopic analysis (section 2.7.2) and applying them to the empirical equation given by Erez and Luz, 1983 (Eq. 2.2). The obtained paleo $\delta^{18}O_{SW}$ (Fig. 5.3, Table C1-C4) records are then corrected for the Global Ice Volume (GIV) effect using linear interpolation of the GIV correction dataset provided by Waelbroeck et al., 2002 in order to remove the changes in the $\delta^{18}O_{SW}$ caused by global ice-melt fractions. The GIV corrected $\delta^{18}O_{SW}$ records (Fig. 5.4, Table C1-C4) are then applied into the empirical $S_{SW} \sim \delta^{18}O_{SW}$ relationship given by Srivastava et al., 2007 (Eq. 2.1) in order to obtain the paleosalinity (S_{SW}) (Fig. 5.5, Table C1-C4) reconstruction records from the SK-312/12 paleothermocline.

Under ideal conditions, the ocean-atmospheric processes governing the surface and the thermocline water mass salinity are different in the respective empirical relationships. However, subject to the absence of appropriate subsurface $S_{SW} \sim \delta^{18}O_{SW}$ calibrations from the EIO

thermocline, the present study utilizes the available surface oceanic calibration provided by Srivastava et al., 2007 (Eq. 2.1) as the common equation for the paleosalinity reconstruction of the complete upper EIO.

5.5 Results

5.5.1 Oxygen Isotopic Records of Planktonic Foraminifers

The oxygen isotopic records of individual planktonic foraminifers ($\delta^{18}O_f$) were obtained from the oxygen isotopic analysis of the individual shell carbonates using the KIEL IV carbonate system (section 2.7.2). The $\delta^{18}O_f$ records of *G. ruber (s.s.)* ($\delta^{18}O_{G.\ ruber}$) varies between -2.31‰ to -0.20‰ with a mean value of -1.01‰. The $\delta^{18}O_f$ records of *T. sacculifer* (w/s) ($\delta^{18}O_{T.\ sacculifer}$) varies

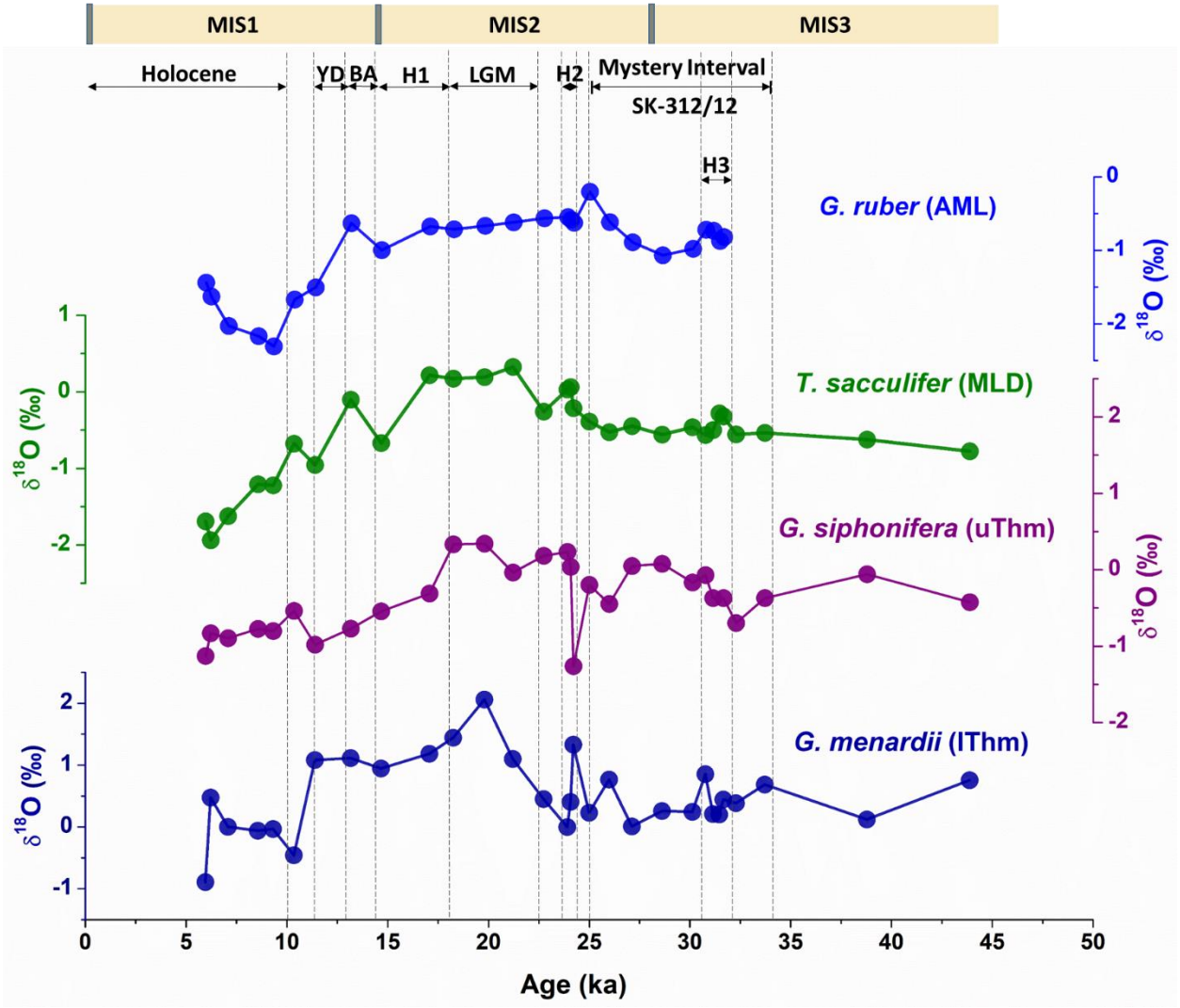

Figure 5.2: Foraminiferal oxygen isotopic records from SK-312/12 paleothermocline.

between -1.94‰ to 0.33‰ with a mean value of -0.54‰. The $\delta^{18}O_f$ records of *G. siphonifera* ($\delta^{18}O_{G.\ siphonifera}$) varies between -1.26‰ to 0.34‰ with a mean value of -0.37‰. The $\delta^{18}O_f$ records of *G. menardii* ($\delta^{18}O_{G.\ menardii}$) varies between a -0.89‰ to 2.06‰ with a mean value of 0.51‰ (Fig. 5.2, Table C1-C4).

5.5.2 Oxygen Isotopic Records of the Oceanic Water Mass

Fig. 5.3, Table C1-C4) represents the oxygen isotopic records of the past upper EIO water mass ($\delta^{18}O_{SW}$) reconstructed using the $\delta^{18}O_f$ and the T_{SW} into the calibration equation, Eq. 2.2 given by Erez and Luz, 1983. The records obtained from the *G. ruber (s.s.)* dataset represent the corresponding records of the average mixed layer (AML). The $\delta^{18}O_{SW}$ records obtained from *T. sacculifer* (w/s), *G. siphonifera* and *G. menardii* represent the Mixed Layer Depth (MLD), the

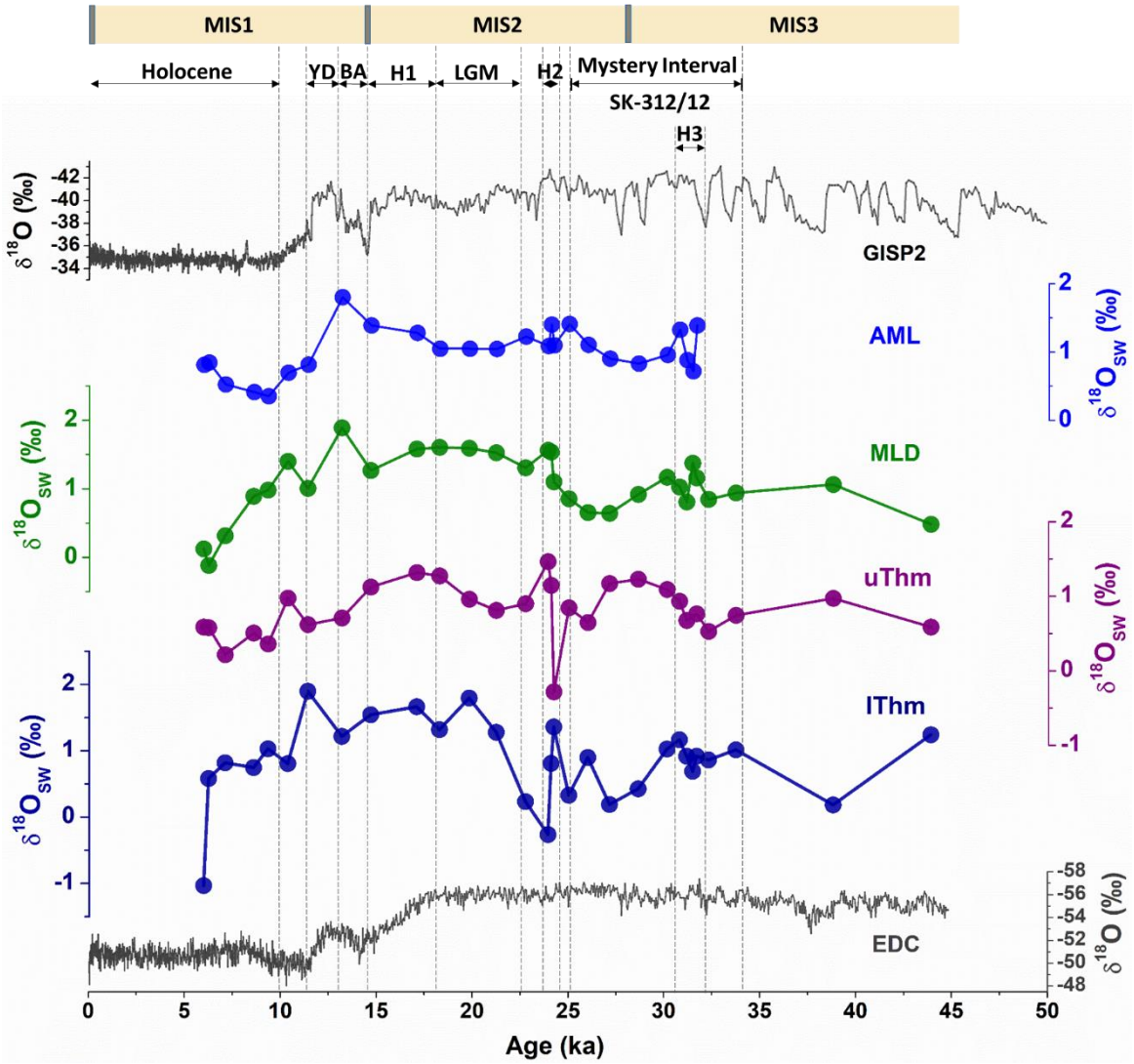

Figure 5.3: GIV uncorrected sea water oxygen isotopic records from SK-312/12 paleothermocline.

upper thermocline (uThm) and the lower thermocline (lThm) oceanic depths respectively. The $\delta^{18}O_{SW}$ records of AML varies between 0.35‰ to 1.80‰ with a mean value of 1.01‰. The $\delta^{18}O_{SW}$ records of MLD varies between -0.12‰ to 1.89‰ with a mean value of 1.05‰. The $\delta^{18}O_{SW}$ records of uThm varies between -0.28‰ to 1.46‰ with a mean value of 0.81‰. The $\delta^{18}O_{SW}$ records of lThm varies between -1.03‰ to 1.90‰ with a mean value of 0.85‰. (Fig. 5.3, Table C1-C4).

The North Atlantic climatic influences are clearly observed during the H3 and H2 events. The BA-warming is marked by corresponding $\delta^{18}O_{SW}$ peaks within the AML and MLD indicating a limited influence into the thermocline water depths. The Antarctic intermediate water mass influences

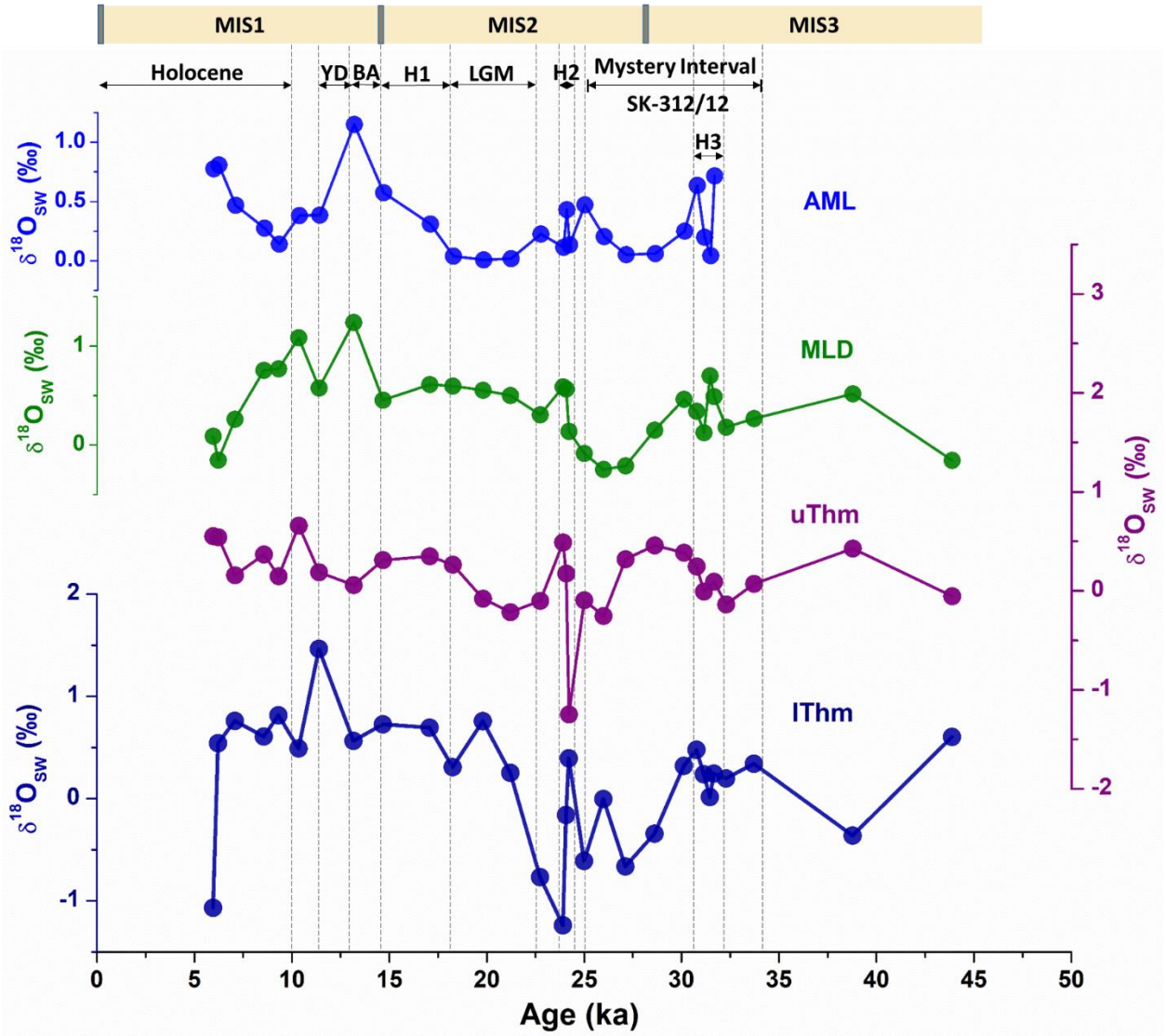

Figure 5.4: GIV corrected sea water oxygen isotopic records from SK-312/12 paleothermocline.

were variable on the thermocline regions of SK-312/12 over the glacial-deglacial time period (Fig. 5.3).

The $\delta^{18}O_{SW}$ records were corrected for the Global Ice Volume (GIV) effect in order to eliminate the variations in the $\delta^{18}O_{SW}$ caused by changes in the global ice-melt fractions over the paleoclimatic periods using linear interpolation of the GIV correction dataset provided by Waelbroeck et al., 2002. The obtained results are given in Table C1-C4 and plotted in Fig. 5.4. The result obtained for AML varies between 0.01‰ to 1.15‰ with a mean value of 0.34‰. The record for MLD varies between -0.25‰ to 1.24‰ with a mean value of 0.38‰. The record from uThm varies between -1.25‰ to 0.66‰ with a mean value of 0.14‰. The lThm record varies between -1.24‰ to 1.46‰ with a mean value of 0.19‰.

5.5.3 Paleosalinity Reconstructions of SK-312/12 Paleothermocline

Paleosalinity records from SK-312/12 thermocline were obtained by using the GIV corrected $\delta^{18}O_{SW}$ records into the empirical $\delta^{18}O_{SW} \sim S_{SW}$ relationship given in Eq. 2.1 proposed by Srivastava et al., 2007. The results represent the paleosalinity of the AML to be varying between 32.95‰ to 37.18‰ with a mean record of 34.19‰. The MLD represents a paleosalinity variation between 32.01‰ to 37.51‰ with a mean record of 34.34‰. The uThm represents a paleosalinity variation from 28.30‰ to 35.36‰ with a mean record of 33.44‰. The lThm represents a paleosalinity variation from 28.34‰ to 38.35‰ with a mean record of 33.62‰ (Fig. 5.5, Table C1-C4).

5.6 Discussions

The paleosalinity of the average mixed layer (S_{AML}) has remained lower during the cold periods like LGM and early MIS2, whereas the salinity at the MLD (S_{MLD}) has remained relatively higher during the LGM. The S_{AML} reduced during the early Holocene followed by an increase during the mid-Holocene. The S_{MLD} records a constant decrease during the subsequent time period. Paleosalinity records from the uThm (S_{uThm}) and lThm (S_{lThm}) were variable during the glacial-deglacial time periods possibly attributed to the differential intermediate water mass contributions (Fig.5.5).

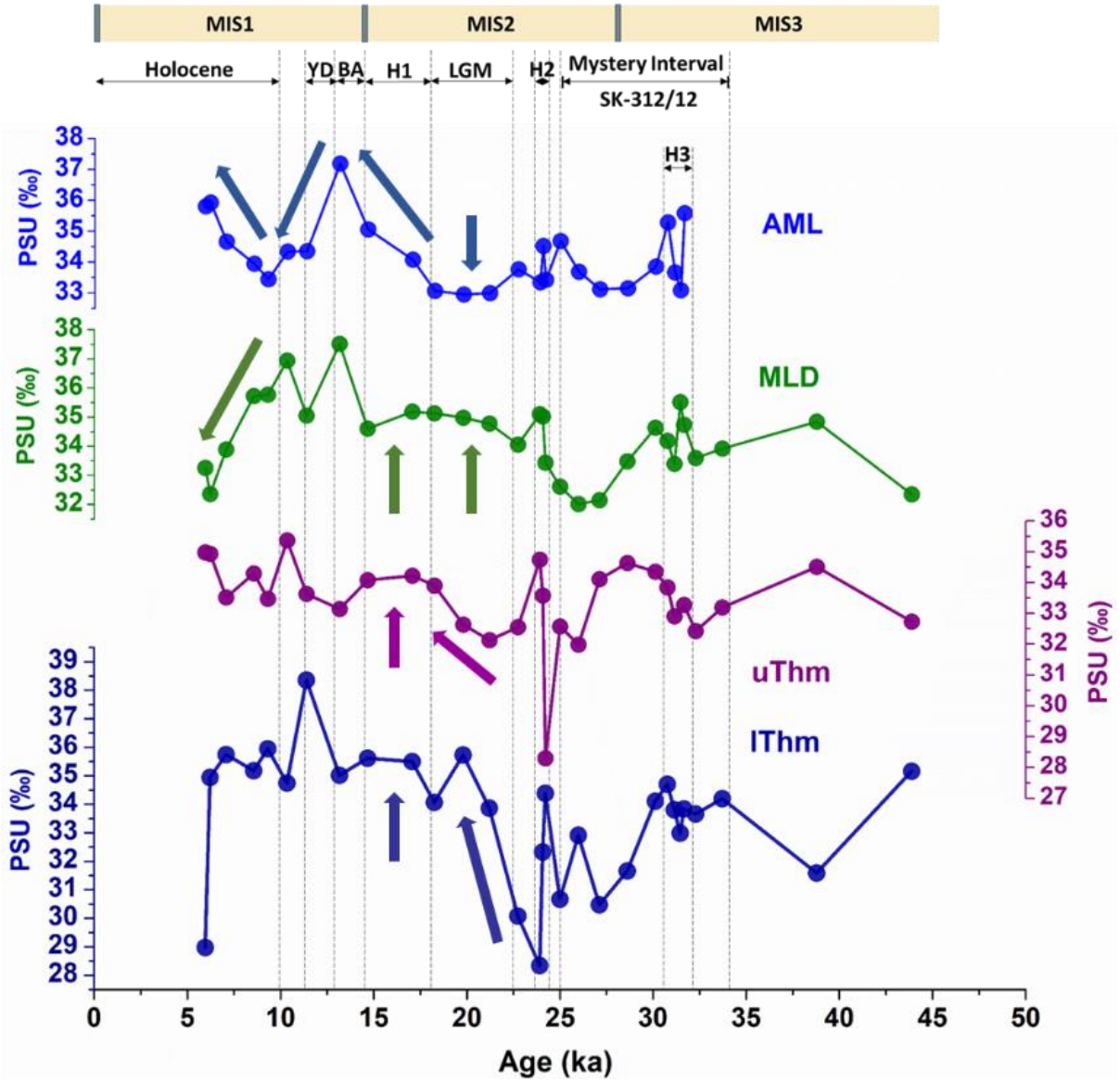

Figure 5.5: Paleosalinity records from SK-312/12 paleothermiclne.

5.6.1 The Surface Ocean Variability

Fig. 5.6 represents the mean paleosalinity records of SK-312/12 averaged over the specific paleoclimatic time periods spanning over the last 44 ka.The variations in the S_{AML} record represent a reduction during the colder time periods of early MIS2, H2 and LGM followed by a constant increase during the warmer H1 and the BA-warming periods. Considering a negligible terrestrial and fresh water influxes over the SK-312/12 study region, the primary cause of the S_{AML} variability is associated with the subsequent variations in the equatorial precipitation. The equatorial

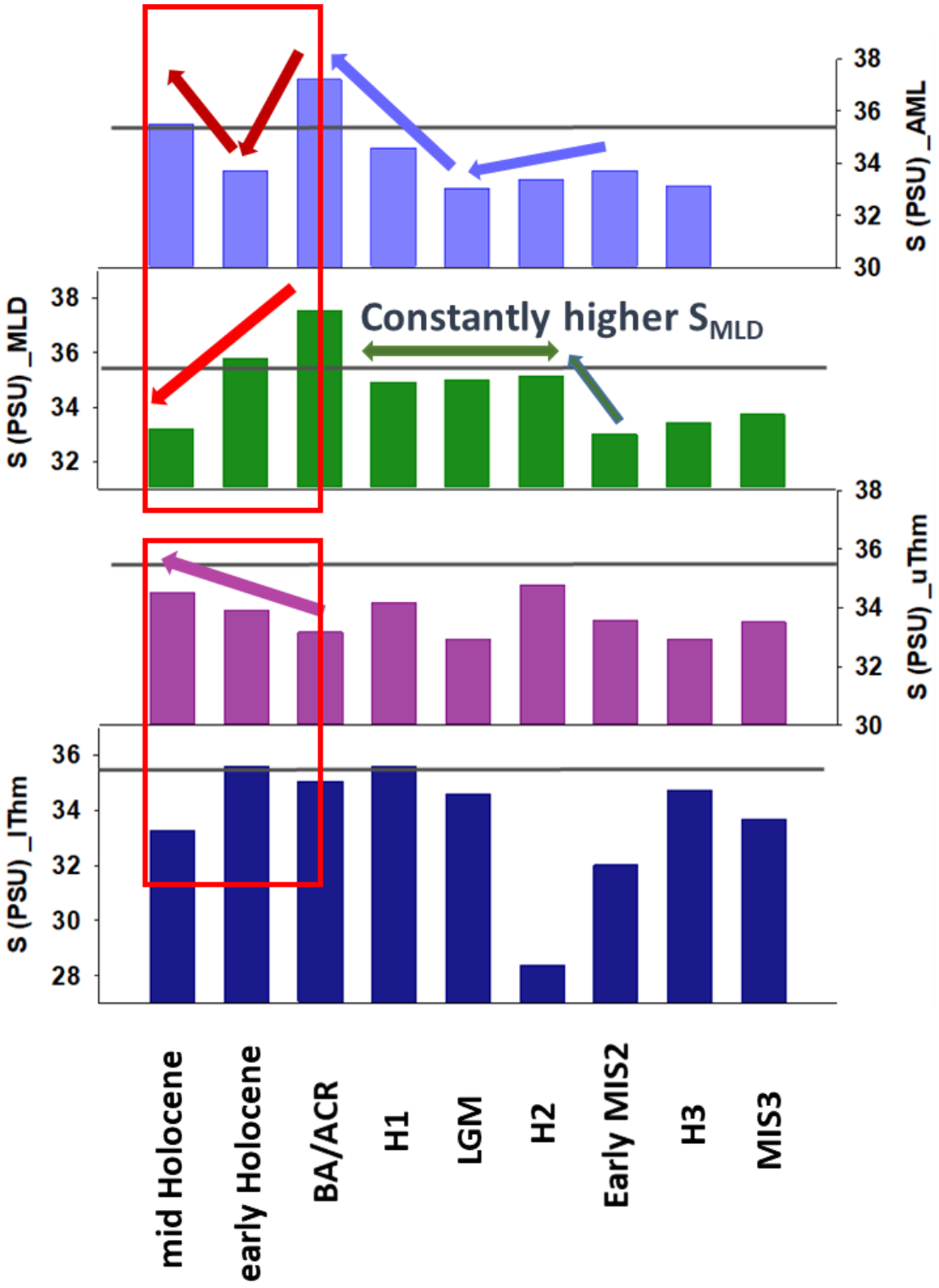

Figure 5.6: Variations in the mean paleosalinity records during different paleoclimatic intervals. Grey lines represent the present-day records over SK-312/12.

precipitation is the predominant source of fresh water addition into the surface EIO resulting from persistent warming of the equatorial water mass caused by higher solar influx and subsequent precipitation produced by the rising branch of the lower atmospheric Hadley cell circulations. During the warmer climatic periods, the Inter Tropical Convergence Zone (ITCZ) shifts northwards farther over the Indian subcontinent due to the increased relative sub-continental warming compared to the Indian Ocean. The process results in a relative decrease in the equatorial precipitation and a subsequent increase in the evaporation over the western EIO driven by strong SW monsoonal winds. Whereas, the ITCZ shifts southwards during the colder periods, aligning near the equator thus results in an enhancement of the equatorial precipitation with reduced water mass evaporation. An increased evaporation and reduced precipitation leads to increase in the S_{AML} during the warmer climatic periods, whereas, a reduced evaporation and an increase in the equatorial precipitation leads to a resultant decrease in the S_{AML} during the colder climatic periods. The colder glacial periods have thus evidenced a lowering in the S_{AML} record, whereas, the warmer early deglacial periods have witnessed a subsequent increase in the corresponding records.

5.6.2 Variabilities in the Mixed Layer Depth

The present-day oceanic salinity profile over SK-312/12 indicates a predominant contribution of ASHSW taking place into the Mixed Layer Depth (MLD) of the SK-312/12 thermocline. The present study utilises the above characteristic observation as the distinct criteria to investigate the variability of the ASHSW mass exchange over the EIO during different paleoclimatic time periods. The observations show an elevated S_{MLD} during the colder H1, H2 and LGM periods compared to the relatively cooler MIS3-MIS2 transition periods.

The Arabian Sea High Salinity Water (ASHSW) is formed in the upper northern AS due to the reduced fresh water supply associated with the limited contributions of the south-west monsoonal (SWM) precipitation over the northern Arabian Sea (AS). The cold North-East Monsoonal (NEM) winds promote further enhancement in the surface oceanic salinity over the northern AS through wind driven evaporation and cooling. Both of the above processes thus combinedly facilitate a significant enhancement of the sea surface salinity over the northern AS. The increased salinity results in a subsequent increase in the density of the corresponding water mass allowing it to sink

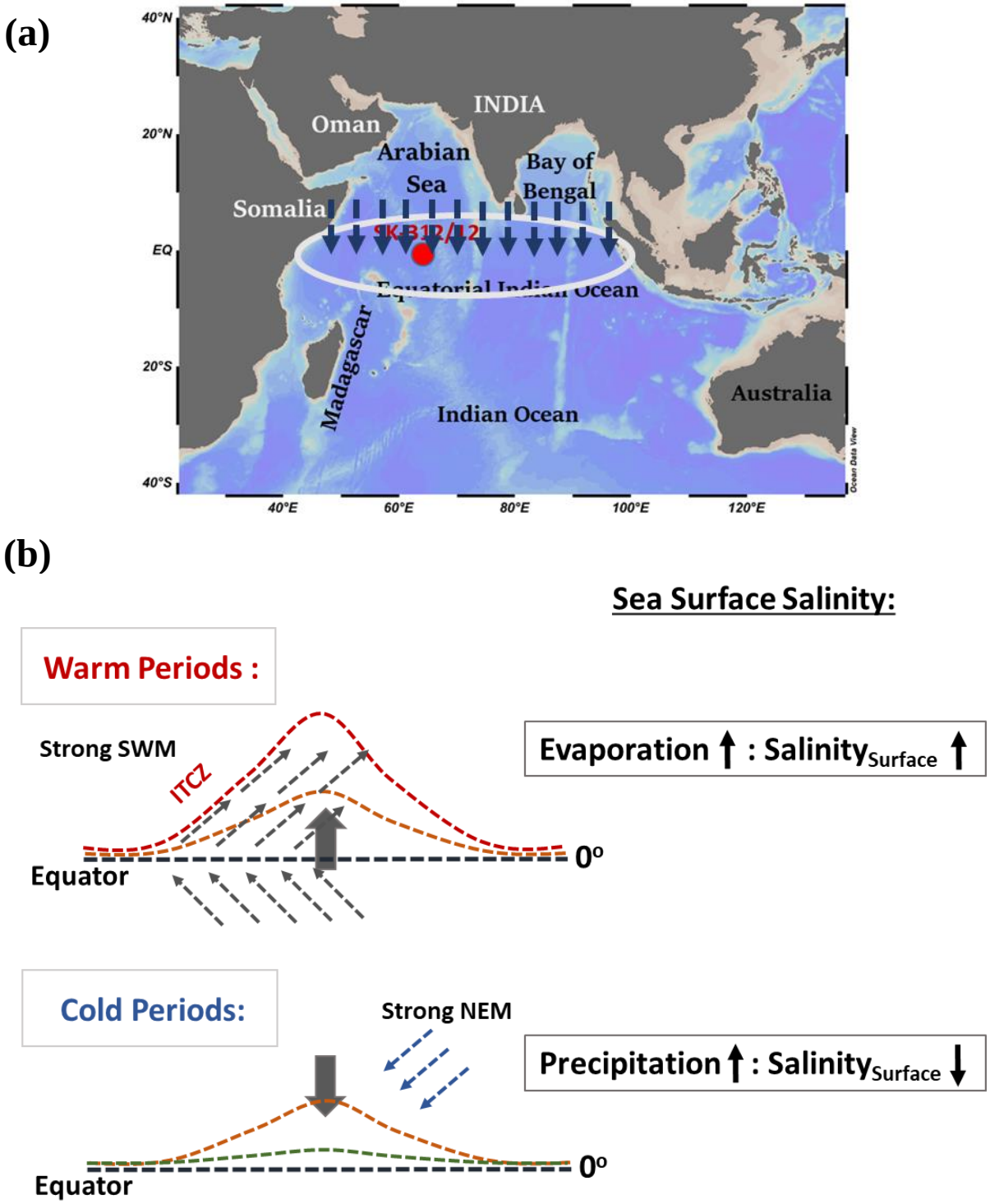

Figure 5.7: Schematic representation of the mechanism of surface oceanic salinity variations during warm and cold climatic periods. (a) The dark blue downward arrows represent the equatorial precipitation. (b) Schematic explanation of shift in ITCZ and variations in equatorial precipitation during warm and cold climatic periods.

and spread at subsurface oceanic depths contributing its fluxes into the EIO and the BoB (Sanchez-Franks et al., 2019; Kumar and Prasad, 1999) in the form of ASHSW (Section 1.3.2). The production and contribution of the ASHSW is thus strongly controlled by the Indian Monsoonal variability.

Fig. 5.8 represents the schematic explanations of the possible variations in the ASHSW during the past warmer and colder climatic periods. During the warmer climatic periods, the ITCZ shifts significantly northwards over the Indian sub-continent leading to an enhancement of south-west monsoon (SWM). The process leads to an increase in the fresh water contribution of the monsoonal precipitation over the northern AS. An increased fresh water supply leads to a subsequent freshening of the northern AS surface water thus inhibiting the production of the ASHSW. Whereas, the Indian Summer Monsoon system weaken during the colder climatic periods leading to reduced fresh water additions over the northern AS, thus favoring the increase in the surface oceanic salinity over the northern AS. A strengthening of the Indian Winter Monsoon (Tiwari et al., 2005; Godad et al., 2022) during the cold climatic periods further enhances the formation of ASHSW through increased surface oceanic cooling caused by the cold north-east monsoonal winds. The observed S_{MLD} variations from SK-312/12 clearly complement the above explanations by representing an enhancement in the production and equatorial distribution of the ASHSW during the colder glacial periods and a relative reduction in its formation during the warmer paleoclimatic periods.

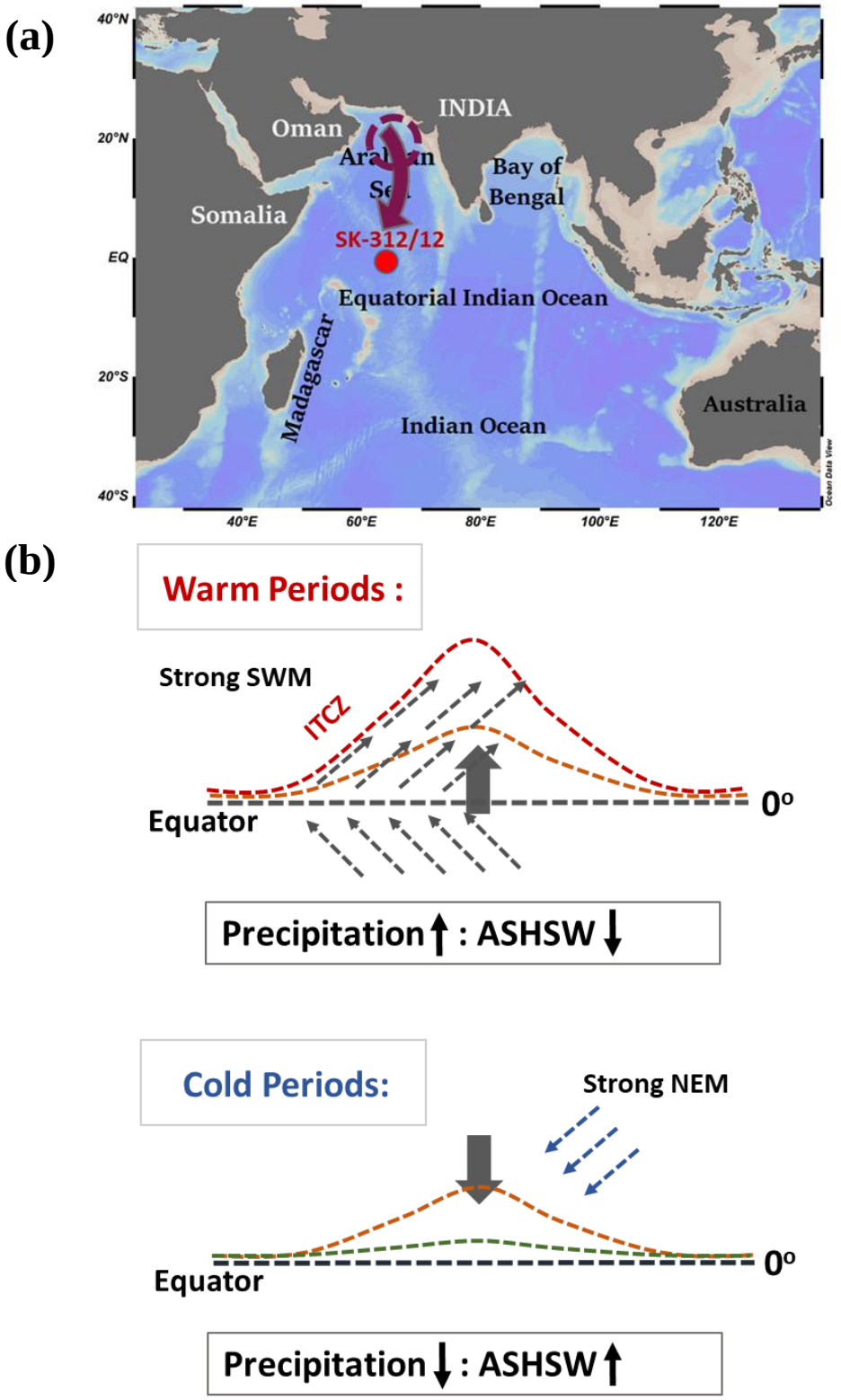

Figure 5.8: Schematic representation of mechanism of ASHSW variability during warm and cold climatic periods. (a) Production and southward propagation of ASHSW (b) Shifting of ITCZ, subsequent changes in precipitation over northern AS and ASHSW production.

5.6.3 Paleosalinity Variations during the Holocene

The surface salinity variations during the Holocene deviate from the scientific explanations discussed in section 4.5.1. The Holocene was a period of south-west monsoonal strengthening (Tiwari et al., 2010), which should lead to a constant increase in S_{AML} over the SK-312/12 region. However, the early Holocene observes a decrease in the S_{AML} that strongly disregards the fundamental consensus of the primary influence of south-west monsoonal (SWM) variability upon the S_{AML} variations of SK-312/12 during the early Holocene. Subsidiary information available from the Indo-Pacific equatorial paleooceanographic studies provide strong observational evidence of an IOD-ENSO like coupled climatic state existing during the warm Holocene periods (Rein et al., 2005; Liu et al., 2023), which could potentially modify the fundamental mechanism of the ocean-atmospheric and climatic processes operating over the EIO.

Fig. 5.9 represents the schematic explanation of the influence of IOD-ENSO coupling in bringing modification into the regional climatic operations over the EIO through changes in the general patterns of the surface oceanic hydro-climatic circulations. The early Holocene experienced an El-Nino like condition over the equatorial pacific and a subsequent positive IOD condition prevailing over the EIO. The combination of both of the processes would result in a warmer surface oceanic condition over the western EIO and a relatively cooler surface condition over the eastern EIO. The effect of the process would lead to an enhanced moisture production and subsequent precipitation over the western EIO, leading to a decrease in the S_{AML} record. Whereas, the mid Holocene observed a La-Nina and negative IOD coupling state over the Indo-Pacific equatorial oceanic region, which would lead to a subsequent reduction in precipitation and increased wind driven evaporation over the western EIO with a contemporary increase in precipitation over the warmer eastern equatorial surface ocean. This lead to a resultant increase in the S_{AML} as observed in the SK-312/12 record during the mid Holocene period.

The constant reduction in the S_{MLD} was possibly caused by the enhancement in the SWM intensity during the Holocene (Tiwari et al., 2010).

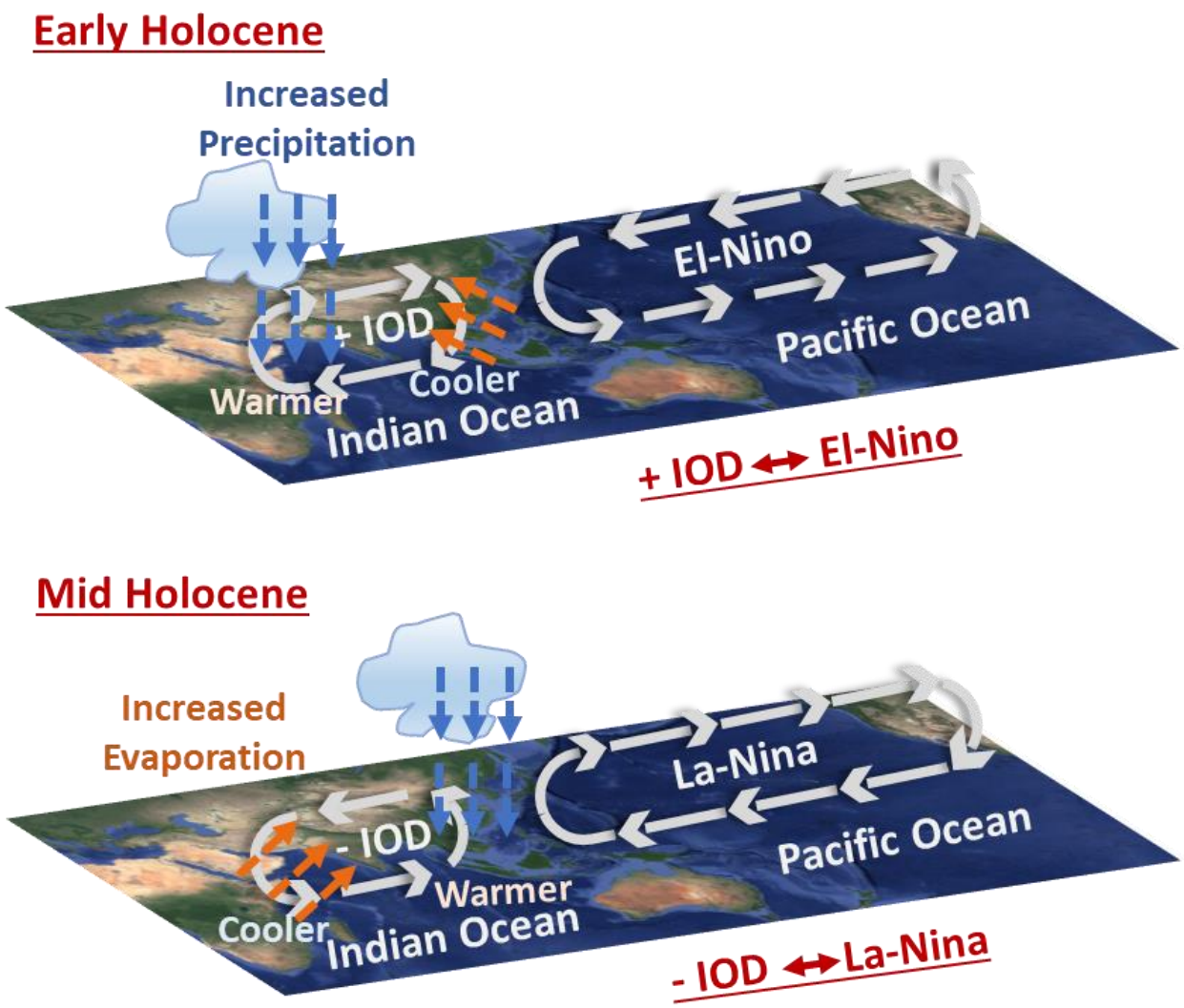

Figure 5.9: Schematic representation of ENSO-IOD coupling resulting in variation in equatorial precipitation and surface oceanic salinity variations during the early Holocene (upper) and mid Holocene (lower) climatic periods. The notations '+ IOD' and '– IOD' denote positive IOD and negative IOD respectively.

5.6.4 Paleosalinity Variations from the Subsurface Thermocline

The thermocline during H1 was under the complete influence of Antarctic Intermediate water masses as discussed in chapter 3 and chapter 4. The salinity records remained more or less steady in the MLD, uThm and lThm, however, an increase in the S_{AML} is possibly attributed to the increased surface oceanic evaporation experienced by the warmer Antarctic Intermediate Water mass produced during the subsequent time period of Antarctic Cold Reversal (ACR). An increase in salinity in the thermocline during LGM was possibly associated with the increase in the supply

of ASHSW into the upper thermocline and the enhancement of the equatorial upwelling (Chandana et al., 2018) driving an effective mixing and rise in salinity of the lower thermocline water. Whereas, the S_{uThm} and S_{lThm} are influenced by RSW and ITF respectively, as inferred earlier.

The salinity variations of the upper thermocline (S_{uThm}) is possibly associated with mixed contributions of the ASHSW and the Antarctic Intermediate Waters during the glacial-deglacial period, whereas, the Holocene variability is possibly dominated by the increased contributions of RSW (Chapter 4). The salinity of the lower thermocline is primarily associated with the Antarctic Intermediate Water mass contributions during the glacial-deglacial time periods, whereas, the ITF strength predominated the Holocene time period (Chapter 4).

5.7 Conclusion

A quantitative paleosalinity reconstruction of the EIO paleothermocline has been carried out as a maiden study attempt from an open Indian Oceanic region from four characteristic water depths using the depth-specific planktonic foraminifers. The results represent an overall surface salinity reduction during the cold climatic periods and corresponding increase during the warm climatic periods. The primary cause of this surface oceanic salinity variations is primarily associated with the corresponding decrease and increase in the surface oceanic evaporation, associated with the relative shifting of ITCZ across the EIO, during the cold and warm climatic periods respectively. The production and distribution of the ASHSW into the EIO increased during the cold climatic periods due to a subsequent reduction in the SWM precipitation and strengthening of NEM, whereas, the production and distribution of ASHSW reduced during the warm periods due to the increase in fresh water addition over the northern AS along with the subsequent reduction in the NEM wind strength. The Holocene climatic variability was predominated by the IOD-ENSO coupled phenomenon. The reduction in the surface oceanic salinity over the SK-312/12 region during the early Holocene resulted due to the prevailing positive IOD conditions, whereas, the negative IOD conditions resulted in a subsequent increase in the surface oceanic salinity during the mid Holocene. The paleosalinity records of the upper thermocline was under a mixed influence of the ASHSW and the Antarctic Intermediate Water with a predomination of RSW during the Holocene. The lower thermocline was primarily contributed by the Antarctic Intermediate Waters for most of the glacial-deglacial period with a strong ITF influence observed during the Holocene period.

Chapter 6

Summary and Future Scope

6.1. Summary

The present study is a maiden attempt from an open Equatorial Indian Ocean (EIO) to obtain a quantitative reconstruction of a complete paleothermocline profile using the depth-specific planktonic foraminifers from the characteristic upper oceanic water depths. The study aims at understanding the millennial scale evolution of the EIO paleothermocline and its broader implications towards the regional and global paleoceanographic and paleoclimatic variabilities. The study has been carried out using a sediment core SK-312/12 situated over the western central EIO within a small basin around 300 km south of the transect zone between the Bao-Chuan fracture zone and the Carlsberg ridge, at 0°N, 65°E. The oceanography of the study region is predominated by an eastward flowing south-west monsoon current and a strong western boundary Somali Current (SC) during the summer monsoon period and a north-east monsoonal current carrying fresher Bay of Bengal waters during the winter monsoon period. Three major proxies from the planktonic foraminiferal shells have been investigated that include the Mg/Ca, the radiocarbon (^{14}C) and the stable oxygen isotopic records of the planktonic foraminifers ($\delta^{18}O_f$). The chronology of the sediment core extends up to last 44 ka of the last glacial-interglacial time periods. Some of the salient outcomes obtained from the current research work are:

- A preliminary evidence of an extremely radiocarbon depleted hydrothermal interval has been identified from the EIO paleothermocline spanning between 25-34 ka, which has been named as the MIS3-MIS2 Transition 'Mystery Interval'.
- Significant volcanic activities reported from the Amsterdam Island and (or) the Reunion hotspot during the contemporaneous Mystery Interval time period, appear to be the responsible source(s) of the necessary hydrothermal dead carbon supply into the EIO thermocline.
- A strong North Atlantic climatic tele-connection has been observed on the termination of the hydrothermal source ventilation into the EIO thermocline during the Heinrich 2 (H2) climatic period. The mechanism explaining the tele-climatic control of the H2 event in terminating the hydrothermal source ventilation existing through the Mystery Interval however, remains unclear.
- The deglacial radiocarbon depletions of the EIO paleothermocline was primarily associated with the contribution of the aged supersaturated deep southern oceanic reservoir via Sub-

Antarctic Mode Water-Antarctic Intermediate Water (SAMW-AAIW) through ocean-tunneling.

- Strong tele-climatic connections of the high-latitude climatic systems have been observed on the millennial scale reconstruction records of the SK-312/12 paleothermocline. The influence of the North Atlantic climate predominates during the Heinrich events (H2 and H3) over the glacial period, whereas, the Antarctic climatic influences predominates over the subsurface thermocline during the glacial and early deglacial periods.
- Interbasinal climatic connectivity is observed during the Holocene with a strong evidence of the enhancement of the Indonesian Through Flow into the lower thermocline depths of the western EIO.
- The upper thermocline possibly represented a mixed response of the Antarctic Intermediate Water masses and the surface oceanic variabilities during the periods of advective water mass mixings. The influence of RSW was possibly enhanced over the upper thermocline region of SK-312/12 during the Holocene time period.
- The paleotemperature records of the mixed layer primarily remained under the influence of the total solar insolation, whereas, the thermocline waters more strongly controlled by the intermediate water source variabilities.
- The salinity of the surface ocean was primarily controlled by the evaporation-precipitation balance associated with the meridional shifting of the Inter-Tropical Convergence Zone (ITCZ). The strong northward shift of ITCZ over the Indian sub-continents during the warm climatic periods, resulted in an increase in the surface oceanic evaporation over the western EIO, thus resulting in an increase in the sea surface salinity. Whereas, an increased southward shift of ITCZ around the equator helped in enhanced moisture collection and subsequent equatorial precipitation, thus, leading to a decrease in the sea surface salinity record.
- The salinity at the mixed layer depth (MLD) over the SK-312/12 study region is primarily associated with the Arabian Sea High Salinity Water (ASHSW) mass contribution. The paleosalinity reconstructions from the MLD suggested an increased production and contribution of ASHSW into the subsurface EIO during the cold climatic periods, whereas, the contribution decreased during the warm climatic periods through a reduced production of the ASHSW mass. During the cold climatic periods, the strengthening of south-west

monsoon due to increased northward shifting of ITCZ across the equator, promotes increased fresh water supply into the northern Arabian Sea (AS), thus decreasing the surface oceanic salinity of the regional water mass and inhibiting the formation of high saline surface water to promote the ASHSW formation. A weakening of north-east monsoon (NEM) is also responsible for its limited cold wind supplies to promote surface evaporation and cooling to aid the ASHSW formation. On the contrary, ITCZ moves close to the equator during the cold climatic intervals resulting in a decrease in the SWM strength and a subsequent increase in the strength of the NEM. This leads to a reduction in the fresh water supply into the northern AS produced by the SWM precipitation, thus promoting the formation of high saline surface water around the region. An increased NEM strength also favours the formation of ASHSW by providing strong cold NEM wind driving surface evaporation and cooling to increase the sea water density.

- The surface salinity records obtained during the Holocene however, don't comply with the general hydro-climatic circulation mechanisms. The results indicate a decrease in the surface oceanic salinity caused by the prevailing positive IOD-El-Nino coupling over the Indo-Pacific equatorial region during the early Holocene. A negative IOD-La-Nina coupling during the mid Holocene resulted in a subsequent increase in the sea surface salinity record.
- The paleosalinity variations of the upper thermocline was under the mixed influence of the ASHSW and the Antarctic Intermediate water during the glacial-deglacial periods with a predomination of Red Sea Water influence during the Holocene. The lower thermocline observed a primary contribution of the Antarctic Intermediate Waters for most of the glacial-deglacial periods, however, the Indonesian Through Flow predominated the paleosalinity records during the Holocene.

6.2. Future Scope

The present study has critically investigated various surface and subsurface paleoceanoographic and paleoclimatic processes associated with the paleoclimatic evolution of the SK-312/12 paleothermocline. However, a several emerging study aspects have evolved out of the present observations as potential aspects for future research, that are briefly discussed in the following section.

- Detailed geochemical and geophysical investigations need to be carried out over the Indian Ocean basin in order to delineate the possible sources and mechanisms of past radiocarbon ventilation records into the EIO paleothermocline.
- The tele-climatic influence of the North Atlantic Heinrich event needs special scientific attention to understand the plausible mechanism associated with the tele-climatic regulation and interruption of the hydrothermal source ventilation into the EIO paleothermocline following the Mystery Interval.
- High-resolution sediment cores from limited local climatic perturbation regions should be attempted to obtain fine scale paleoclimatic variability records of the EIO.
- Long-term reconstruction records of IOD-ENSO variabilities are required for obtaining comparative assessments of inter-basinal and inter-hemispheric paleo-climatic evolutions.
- Improved regional calibrations for paleotemperature reconstructions and the paleosalinity reconstructions of the subsurface thermocline are necessary for a better accuracy in the quantitative estimations to provide better paleoclimatic assessments.
- Essential efforts need to be carried out in order to explore the deeper ocean using the subsequent planktonic water mass proxy records in order to obtain a comprehensive understanding of the integrated history of the paleooceanographic evolutions.

Appendices

Appendix A: Dataset Relevant to Chapter 2

Table A1: Analytical results of planktonic foraminifers (Phase I) measured using ICP-OES.

(a) *G. ruber* and *T. sacculifer*

		G. ruber			***T. sacculifer***		
Core Depth (cm)	**Age (ka)**	**Mg conc. (ppb)**	**Ca conc. (ppm)**	**Mg/Ca (mmol/mol)**	**Mg conc. (ppb)**	**Ca conc. (ppm)**	**Mg/Ca (mmol/mol)**
1.5	6.0	-0.06	0.13	-0.80	7.49	4.43	2.79
4	6.2	0.13	0.23	0.90	2.67	1.57	2.80
6.5	7.1	1.82	0.95	3.16	0.25	0.37	1.11
9.5	8.6	0.54	0.44	2.04	8.49	4.41	3.17
11.5	9.3	0.28	0.22	2.10	11.62	5.76	3.33
14.5	10.3	0.21	0.21	1.68	13.93	7.31	3.14
16.5	11.4	0.54	0.48	1.88	10.86	6.00	2.98
19.5	13.2	0.13	0.25	0.83	16.63	9.06	3.03
21.5	14.7	0.00	0.04	0.16	9.30	5.20	2.95
24.5	17.1	0.40	0.43	1.53	4.35	3.15	2.28
26.5	18.3	-0.14	0.03	-7.94	4.17	2.60	2.65
29.5	19.8	-0.49	0.00	269.08	0.92	1.02	1.50
31.5	21.2	1.28	0.95	2.23	2.15	1.68	2.12
33.5	22.7	1.54	1.01	2.52	4.39	2.90	2.50
35.5	23.9	0.97	0.77	2.08	3.06	2.06	2.46
37.5	24.1	3.25	2.20	2.44	3.96	2.72	2.40
39.5	24.2	0.89	0.67	2.18	2.92	2.16	2.23
41.5	25.0	2.96	1.87	2.61	0.22	0.52	0.71
43.5	26.0	1.40	1.12	2.07	1.68	1.32	2.10
45.5	27.1	-0.45	0.00	-185.83	1.46	1.19	2.02
47.5	28.6	-0.38	0.00	210.12	3.65	2.51	2.40
49.5	30.1	-0.26	0.00	144.37	5.13	3.29	2.57

51.5	30.8	-0.32	0.04	-13.68	4.29	2.80	2.53
53.5	31.1	-0.40	0.00	331.97	2.71	2.01	2.22
55.5	31.5	-0.30	0.01	-82.72	3.19	2.03	2.60
57.5	31.7	-0.47	0.00	389.77	3.23	2.21	2.41
59.5	31.9	3.24	1.98	2.70	1.50	1.24	2.00
61.5	32.1	-0.17	0.17	-1.65	0.99	0.99	1.65
63.5	32.3	3.29	1.95	2.77	3.39	2.41	2.32
65.5	33.7	1.33	0.97	2.26	6.27	4.31	2.40
67.5	38.8	2.29	1.43	2.65	4.36	2.73	2.64
69.5	43.9	2.17	1.33	2.68	1.92	1.45	2.18

(b) *G. siphonifera* and *G. menardii*

		G. siphonifera			***G. menardii***		
Core Depth (cm)	**Age (ka)**	**Mg conc. (ppb)**	**Ca conc. (ppm)**	**Mg/Ca (mmol/mol)**	**Mg conc. (ppb)**	**Ca conc. (ppm)**	**Mg/Ca (mmol/mol)**
1.5	6.0	0.31	0.48	1.06	7.20	9.52	1.25
4	6.2	0.55	0.54	1.67	5.72	7.01	1.35
6.5	7.1	0.18	0.35	0.84	10.55	10.38	1.68
9.5	8.6	0.48	0.59	1.35	16.33	16.11	1.67
11.5	9.3	0.65	0.64	1.69	17.64	16.06	1.81
14.5	10.3	0.16	0.32	0.80	18.89	16.16	1.93
16.5	11.4	0.23	0.43	0.88	15.29	15.04	1.68
19.5	13.2	0.14	0.28	0.83	10.14	12.42	1.35
21.5	14.7	0.19	0.31	1.02	12.93	13.60	1.57
24.5	17.1	0.23	0.45	0.83	11.61	12.67	1.51
26.5	18.3	-0.14	0.20	-1.19	9.42	12.39	1.25
29.5	19.8	-0.22	0.12	-2.89	9.39	12.88	1.20
31.5	21.2	-0.04	0.32	-0.21	9.46	11.32	1.38
33.5	22.7	0.59	0.75	1.30	7.23	9.78	1.22
35.5	23.9	0.36	0.52	1.14	5.74	7.88	1.20
37.5	24.1	0.23	0.32	1.18	10.75	12.02	1.48

39.5	24.2	0.77	0.72	1.75	9.05	11.34	1.32
41.5	25.0	0.11	0.29	0.63	6.03	7.40	1.34
43.5	26.0	0.17	0.37	0.77	8.57	10.41	1.36
45.5	27.1	-0.11	0.17	-1.07	8.73	10.45	1.38
47.5	28.6	0.27	0.48	0.93	8.76	10.52	1.37
49.5	30.1	0.35	0.59	0.96	10.52	10.46	1.66
51.5	30.8	-0.05	0.22	-0.34	10.82	12.44	1.43
53.5	31.1	0.13	0.44	0.47	9.97	10.13	1.62
55.5	31.5	0.22	0.47	0.76	11.20	12.19	1.51
57.5	31.7	0.12	0.32	0.59	8.40	10.26	1.35
59.5	31.9	0.14	0.42	0.56	8.12	11.08	1.21
61.5	32.1	0.36	0.63	0.95	10.67	13.56	1.30
63.5	32.3	0.81	0.96	1.38	10.81	11.81	1.51
65.5	33.7	-0.07	0.23	-0.51	8.99	10.28	1.44
67.5	38.8	-0.17	0.13	-2.20	13.92	17.27	1.33
69.5	43.9	0.00	0.28	-0.02	11.31	12.31	1.51

Table A2: Core-top paleotemperature reconstructions of indivisual planktonic foraminifers based on the Phase I analysis.

(a) *G. ruber*

		***G. ruber* (s.s.)**	**Paleotemperature (°C)**		
Core Depth (cm)	**Age (ka)**	**Mg/Ca (mmol/mol)**	**T=(1/0.09)*ln((Mg/Ca)/0.38) (Dekens et al., 2002)**	**T=(1/0.089)*ln((Mg/Ca)/0.3) (Lea et al., 2000)**	**T=(1/0.077)*ln(((Mg/Ca)/0.455) (Sagawa et al., 2012)**
1.5	6.0	-0.80	23.7	24.3	22.7
4	6.2	0.90	22.6	23.2	21.4
6.5	7.1	3.16	25.8	26.5	25.2
9.5	8.6	2.04	20.9	21.5	19.5
11.5	9.3	2.10	26.4	27.0	25.9
		Mean	23.9	24.5	22.9
		Present-day mean	**28.8**		

(b) *T. sacculifer*

		T. sacculifer	**Paleotemperature (°C)**		
Core Depth (cm)	**Age (ka)**	**Mg/Ca (mmol/mol)**	**T=(1/0.097)*ln((Mg/Ca)/0.24)** (Hollstein et al., 2017a)	**T=(1/0.077) ln((Mg/Ca)/0.64) (Mulitza et al., 2003)**	**T=(1/0.083)ln((Mg/Ca)/0.47)) (Farmer et al., 2007)**
1.5	6.0	2.79	25.3	19.1	21.5
4.0	6.2	2.80	25.3	19.2	21.5

9.5	8.6	3.17	26.6	20.8	23.0
11.5	9.3	3.33	27.1	21.4	23.6
		Mean	26.1	20.1	22.4
		Present-day mean	**27.1**		

* Depth 6.5cm is not considered for *T. sacculifer* due to inefficient data quality.

(c) *G. siphonifera*

		G. siphonifera	**Paleotemperature (°C)**		
Core Depth (cm)	**Age (ka)**	**Mg/Ca (mmol/mol)**	**T=(1/0.09)*ln((Mg/Ca)/0.532) (Anand et al., 2003)**	**T=(1/0.097)*ln((Mg/Ca)/0.21)** (Hollstein et al., 2017a)	**T=(1/0.077)*ln((Mg/Ca)/0.455) (Sagawa et al., 2012)**
1.5	6.0	1.063389	7.6952533	16.722771	11.02492
4	6.2	1.672452	12.726695	21.391119	16.905826
6.5	7.1	0.83899	5.0617226	14.279289	7.9467676
9.5	8.6	1.354338	10.382495	19.216088	14.165852
11.5	9.3	1.689675	12.840533	21.496742	17.038884
		Mean	9.7413398	18.621201	13.41645
		Present-day mean	**24.1**		

(d) *G. menardii*

		G. menardii	**Paleotemperature (°C)**		
Core Depth (cm)	**Age (ka)**	**Mg/Ca (mmol/mol)**	**T=(1/0.09)*ln((Mg/Ca)/0.38)) (Anand et al., 2003)**	**T=(1/0.097)ln((Mg/Ca)/0.21)** (Hollstein et al., 2017a)	**T=(1/0.068)ln((Mg/Ca)/0.41) (Mohtadi et al., 2010)**
1.5	6.0	1.25	13.2	18.4	16.4
4.0	6.2	1.35	14.0	19.1	17.5
6.5	7.1	1.68	16.5	21.4	20.7
9.5	8.6	1.67	16.5	21.4	20.7
11.5	9.3	1.81	17.3	22.2	21.8
		Mean	15.5	20.5	19.4
		Present-day mean	**20.4**		

Table A3: Paleotemperature reconstructions obtained from the 'Procedural Test' results.

G. ruber		**Paleo Temperature (°C)**	
Sample	**Mg/Ca mmol/mol**	**T= (1/0.09) * ln((Mg/Ca)/0.38) (Dekens et al., 2002)**	**T= (1/0.089)*ln((Mg/Ca)/0.3) (Anand et al., 2003)**
Type: *G. ruber* (I) (core section)			
1TEGR I (0-3cm)	4.27	26.9	29.8
2TEGR I (3-5cm)	3.85	25.7	28.7
3TEGR I (6-7cm)	4.24	26.8	29.7
Average $T_{core-top}$ =		**26.5**	**29.4**
Type: *G. ruber* (II) (core section)			
1TEGR II (0-3cm)	3.53	24.8	27.7
2TEGR II (3-5cm)	3.76	25.5	28.4
3TEGR II (6-7cm)	3.80	25.6	28.5
Average $T_{core-top}$ =		**25.3**	**28.2**
12TEGR II (29-30cm)	2.76	22.0	24.9

Type: *G. ruber* (III) (core section)			
1TEGR III (0-3cm)	3.75	25.4	28.4
2TEGR III (3-5cm)	3.42	24.4	27.3
3TEGR III (6-7cm)	3.68	25.2	28.2
Average $T_{core-top}$ =		**25.0**	**28.0**
11TEGR III (26-27cm)	2.84	22.3	25.3
17TEGR III (39-40cm)	2.84	22.4	25.3

(b) *G. siphonifera*

G. siphonifera		**Paleo Temperature (°C)**		
Sample	**Mg/Ca mmol/ mol**	**T= (1/0.09)*ln((Mg/Ca) /0.532) (Anand et al., 2003)**	**T= (1/0.097)*ln((Mg/Ca)/0.21)** (Hollstein et al., 2017a)	**T= (1/0.077)*ln((Mg/Ca) /0.455) (Sagawa et al., 2012)**
Type: *G. siphonifera* (I) (core section)				
1TEGS I (0-3cm)	2.35	16.5	24.9	21.3

2TEGS I (3-5cm)	2.77	18.3	26.6	23.4
3TEGS I (6-7cm)	-0.60	NA	NA	NA
Average $T_{core-top}$ =		**17.4**	**25.7**	**22.4**

Table A4: Analytical results obtained during Phase II analysis of *G. ruber* and *G. siphonifera*.

		G. ruber			***G. siphonifera***		
Core Depth (cm)	**Age (ka)**	**Mg conc. (ppb)**	**Ca conc. (ppm)**	**Mg/Ca (mmol/mol)**	**Mg conc. (ppb)**	**Ca conc. (ppm)**	**Mg/Ca (mmol/mol)**
1.5	6.0	3.66	1.62	3.73	3.10	1.66	3.08
4	6.2	3.04	1.24	4.04	2.78	1.66	2.76
6.5	7.1	4.71	2.24	3.47	4.27	2.83	2.49
9.5	8.6	8.79	3.45	4.20	4.55	2.84	2.64
11.5	9.3	5.51	2.10	4.32	4.02	2.62	2.53
14.5	10.3	6.22	2.64	3.89	5.78	3.33	2.87
16.5	11.4	8.15	3.51	3.82	10.18	5.68	2.96
16.5	11.4	8.14	3.52	3.81	10.17	5.68	2.95
19.5	13.2	9.28	3.84	3.98	5.96	3.47	2.83
21.5	14.7	7.16	3.01	3.92	5.43	2.96	3.03
24.5	17.1	6.93	3.40	3.36	4.03	2.22	2.99
26.5	18.3	4.10	2.16	3.13	3.77	2.66	2.34
29.5	19.8	4.75	2.18	3.59	4.52	3.56	2.09
31.5	21.2	3.70	2.02	3.02	3.10	2.26	2.26
33.5	22.7	5.11	2.66	3.17	2.85	2.17	2.17
35.5	23.9	3.31	1.83	2.99	9.61	6.09	2.60
35.5	23.9	3.32	1.82	3.00	9.60	6.10	2.59
37.5	24.1	5.56	2.71	3.39	2.36	1.57	2.48
39.5	24.2	3.96	2.11	3.09	2.26	1.57	2.37
41.5	25.0	3.05	1.69	2.97	3.00	2.04	2.43
43.5	26.0	6.08	3.26	3.08	4.76	3.17	2.47
43.5	26.0	6.11	3.26	3.09	4.73	3.16	2.47
45.5	27.1	3.47	1.81	3.17	4.97	3.29	2.50
47.5	28.6	4.59	2.30	3.29	5.76	3.78	2.51
47.5	28.6	4.58	2.31	3.27	5.78	3.78	2.52
49.5	30.1	5.18	2.57	3.33	5.36	3.37	2.62
51.5	30.8	6.11	2.91	3.46	6.47	4.45	2.40

51.5	30.8	6.09	2.89	3.47	6.48	4.46	2.39
53.5	31.1	3.43	1.90	2.97	4.44	3.02	2.43
55.5	31.5	3.60	2.02	2.95	4.98	3.06	2.69
57.5	31.7	2.66	1.19	3.67	3.14	2.07	2.51
59.5	31.9	4.80	2.54	3.11	7.54	4.84	2.57
59.5	31.9	4.80	2.54	3.11	7.48	4.82	2.56
61.5	32.1	8.71	4.26	3.38	5.49	3.41	2.66
61.5	NA	NA	NA	NA	5.49	3.41	2.66
63.5	32.3	6.39	3.29	3.20	5.61	3.57	2.59
65.5	33.7	3.89	1.93	3.32	4.96	3.28	2.49
67.5	38.8	5.53	2.75	3.32	5.41	3.69	2.42
69.5	43.9	3.43	1.70	3.33	3.59	2.47	2.40

Appendix B: Dataset Relevant to Chapter 4

Table B1: Paleotemperature records of individual foraminifers from SK-312/12.

Paleotemperature Records (°C)							
G. ruber		T. sacculifer		G. siphonifera		G. menardii	
Age ka	Temperature	Age ka	Temperature	Age ka	Temperature	Age ka	Temperature
6.0	27.3	6.0	25.3	6.0	24.8	6.0	18.4
6.2	28.4	6.2	25.3	6.2	23.4	6.2	19.1
				7.1	22.1	7.1	21.4
8.6	28.9	8.6	26.6	8.6	22.8	8.6	21.4
9.3	29.2	9.3	27.1	9.3	22.3	9.3	22.2
10.3	27.9	10.3	26.5	10.3	23.9	10.3	22.9
11.4	27.6	11.4	26.0	11.4	24.3	11.4	21.4
13.2	28.2	13.2	26.1	13.2	23.8	13.2	19.1
14.7	28.0	14.7	25.9	14.7	24.6	14.7	20.7
17.1	26.0	17.1	23.2	17.1	24.4	17.1	20.3
18.3	25.0	18.3	NA	18.3	21.3	18.3	18.4
19.8	NA	19.8	NA	19.8	19.8	19.8	18.0
21.2	24.6	21.2	22.5	21.2	20.8	21.2	19.4
22.7	25.2	22.7	24.1	22.7	20.3	22.7	18.1
23.9	24.5	23.9	24.0	23.9	22.6	23.9	18.0
24.1	26.1	24.1	23.7	24.1	22.0	24.1	20.1
24.2	24.9	24.2	23.0	24.2	21.5	24.2	18.9
25.0	24.4	25.0	NA	25.0	21.7	25.0	19.1
26.0	24.9	26.0	22.4	26.0	22.0	26.0	19.2
27.1	25.2	27.1	22.0	27.1	22.1	27.1	19.4
28.6	25.7	28.6	23.7	28.6	22.2	28.6	19.4
30.1	25.9	30.1	24.4	30.1	22.7	30.1	21.3
30.8	26.4	30.8	24.3	30.8	21.6	30.8	19.8
31.1	24.4	31.1	22.9	31.1	21.7	31.1	21.1
31.5	24.3	31.5	24.6	31.5	23.1	31.5	20.4

31.7	27.1	31.7	23.8	31.7	22.2	31.7	NA
32.3	25.3	32.3	23.4	32.3	22.6	32.3	20.3
33.7	25.8	33.7	23.7	33.7	22.1	33.7	19.9
38.8	25.8	38.8	24.7	38.8	21.7	38.8	19.0
43.9	25.9	43.9	22.7	43.9	21.6	43.9	20.4

Table B2: Average paleotemperature records during different paleoclimatic periods.

Average temperature (°C) during different paleoclimatic periods										
Ocean depth (m)	Present Day	mid Holocene	early Holocence	BA/ACR	H1	LGM	H2	early MIS 2	H3	MIS 3
AML	28.8	27.8	29.1	28.2	27	24.8	24.5	25.2	24.3	25.8
MLD	27.1	25.3	26.9	26.1	24.5	22.5	24	23.1	22.9	23.7
uThm	24.1	24.1	22.4	23.8	24.5	20.6	22.6	22.2	21.6	21.8
lThm	20.4	18.8	21.7	19.1	20.5	18.6	18	19.3	19.8	19.7

Table B3: Difference of the average of paleotemperature records from the present-day mean value.

Difference of paleotemperature (°C) with respect to present									
Ocean depth (m)	mid Holocene	early Holocence	BA/ACR	H1	LGM	H2	early MIS2	H3	MIS 3
AML	-1	0.3	-0.6	-1.8	-4	-4.3	-3.6	-4.5	-3
MLD	-1.8	-0.2	-1	-2.6	-4.6	-3.1	-4	-4.2	-3.4
uThm	0	-1.7	-0.3	0.4	-3.5	-1.5	-1.9	-2.5	-2.3
lThm	-1.6	1.3	-1.3	0.1	-1.8	-2.4	-1.1	-0.6	-0.7

Appendix C: Dataset Relevant to Chapter 5

Table C1: Paleosalinity reconstruction dataset for *G. ruber (s.s.).*

***G. ruber (s.s.)* (AML)**						
Age (ka)	**$\delta^{18}O_{G.rub}$ (VPDB)**	**T (°C)**	**$\delta^{18}Osw$ (VSMOW)**	**$\delta^{18}O_{GIV}$**	**$\delta^{18}Osw$ (GIV corrected)**	**Salinity**
6.0	-1.44	27.3	0.81	0.03	0.78	35.80
6.2	-1.63	28.4	0.85	0.04	0.81	35.92
7.1	-2.03	28.7	0.52	0.06	0.47	34.66
8.6	-2.17	28.9	0.41	0.14	0.27	33.94
9.3	-2.31	29.2	0.35	0.21	0.14	33.44
10.3	-1.67	27.9	0.70	0.32	0.38	34.34
11.4	-1.51	27.6	0.82	0.43	0.38	34.35
13.2	-0.63	28.2	1.80	0.65	1.15	37.18
14.7	-1.00	28.0	1.39	0.81	0.57	35.05
17.1	-0.68	26.0	1.28	0.97	0.31	34.07
18.3	-0.71	25.0	1.05	1.01	0.04	33.07
19.8	-0.67	24.8	1.05	1.04	0.01	32.95
21.2	-0.62	24.6	1.04	1.03	0.02	32.99
22.7	-0.57	25.2	1.23	1.00	0.22	33.76
23.9	-0.55	24.5	1.09	0.97	0.11	33.34
24.1	-0.59	26.1	1.40	0.97	0.43	34.52
24.2	-0.63	24.9	1.10	0.97	0.13	33.42
25.0	-0.20	24.4	1.41	0.94	0.47	34.67
26.0	-0.62	24.9	1.10	0.90	0.20	33.68
27.1	-0.89	25.2	0.90	0.85	0.05	33.11
28.6	-1.07	25.7	0.83	0.77	0.06	33.15
30.1	-0.98	25.9	0.96	0.71	0.25	33.85
30.8	-0.72	26.4	1.32	0.69	0.64	35.28
31.1	-0.74	24.4	0.88	0.68	0.20	33.66
31.5	-0.87	24.3	0.72	0.68	0.04	33.08

31.7	-0.82	27.1	1.39	0.67	0.72	35.58

*The dark orange colour represents the unavailability of the actual data from the specific age which has been replaced by the linear Gaussian mean value.

Table C2: Paleosalinity reconstruction dataset for *T. sacculifer (w/s).*

T. sacculifer (w/s) **(MLD)**						
(Age (ka)	**$\delta^{18}O_{T.sacculifer}$ (VPDB)**	**T (°C)**	**δ^{18}Osw (VSMOW)**	**$\delta^{18}O_{GIV}$**	**δ^{18}Osw (GIV corrected)**	**Salinity**
6.0	-1.69	25.3	0.12	0.03	0.09	33.25
6.2	-1.94	25.3	-0.12	0.04	-0.15	32.35
7.1	-1.63	25.9	0.32	0.06	0.26	33.89
8.6	-1.21	26.6	0.89	0.14	0.75	35.72
9.3	-1.22	27.1	0.98	0.21	0.77	35.77
10.3	-0.68	26.5	1.40	0.32	1.08	36.94
11.4	-0.96	26.0	1.01	0.43	0.57	35.05
13.2	-0.10	26.1	1.89	0.65	1.24	37.51
14.7	-0.67	25.9	1.27	0.81	0.45	34.60
17.1	0.22	23.2	1.58	0.97	0.61	35.18
18.3	0.17	23.5	1.60	1.01	0.59	35.12
19.8	0.19	23.4	1.59	1.04	0.55	34.97
21.2	0.33	22.5	1.52	1.03	0.50	34.77
22.7	-0.26	24.1	1.31	1.00	0.30	34.05

23.9	0.03	24.0	1.56	0.97	0.59	35.10
24.1	0.06	23.7	1.53	0.97	0.56	35.01
24.2	-0.21	23.0	1.10	0.97	0.14	33.43
25.0	-0.39	22.7	0.85	0.94	-0.09	32.61
26.0	-0.53	22.4	0.65	0.90	-0.25	32.01
27.1	-0.45	22.0	0.64	0.85	-0.21	32.14
28.6	-0.56	23.7	0.92	0.77	0.15	33.48
30.1	-0.46	24.4	1.17	0.71	0.46	34.63
30.8	-0.57	24.3	1.03	0.69	0.34	34.18
31.1	-0.50	22.9	0.81	0.68	0.12	33.39
31.5	-0.28	24.6	1.37	0.68	0.70	35.51
31.7	-0.32	23.8	1.16	0.67	0.49	34.73
32.3	-0.56	23.4	0.85	0.67	0.18	33.59
33.7	-0.54	23.7	0.94	0.67	0.27	33.91
38.8	-0.63	24.7	1.06	0.55	0.52	34.83
43.9	-0.78	22.7	0.48	0.64	-0.16	32.34

*The dark orange colour represents the unavailability of the actual data from the specific age which has been replaced by the linear Gaussian mean value.

Table C3: Paleosalinity reconstruction dataset for *G. siphonifera*.

G. siphonifera **(uThm)**						
(Age (ka)	**$\delta^{18}O_{G.siphonifera}$ (VPDB)**	**T (°C)**	**$\delta^{18}Osw$ (VSMOW)**	**$\delta^{18}O_{GIV}$**	**$\delta^{18}Osw$ (GIV corrected)**	**Salinity**
6.0	-1.13	24.8	0.59	0.03	0.55	34.97
6.2	-0.83	23.4	0.58	0.04	0.54	34.93
7.1	-0.90	22.1	0.21	0.06	0.16	33.51
8.6	-0.77	22.8	0.51	0.14	0.37	34.29
9.3	-0.80	22.3	0.36	0.21	0.15	33.47
10.3	-0.54	23.9	0.97	0.32	0.66	35.36
11.4	-0.98	24.3	0.62	0.43	0.19	33.62
13.2	-0.77	23.8	0.71	0.65	0.06	33.14
14.7	-0.54	24.6	1.12	0.81	0.31	34.07
17.1	-0.31	24.4	1.32	0.97	0.35	34.21
18.3	0.33	21.3	1.27	1.01	0.26	33.90
19.8	0.34	19.8	0.96	1.04	-0.08	32.63
21.2	-0.04	20.8	0.81	1.03	-0.22	32.12
22.7	0.18	20.3	0.90	1.00	-0.10	32.55
23.9	0.23	22.6	1.46	0.97	0.49	34.74
24.1	0.04	22.0	1.14	0.97	0.17	33.57
24.2	-1.26	21.5	-0.28	0.97	-1.25	28.30
25.0	-0.20	21.7	0.84	0.94	-0.10	32.57
26.0	-0.45	22.0	0.65	0.90	-0.25	31.98
27.1	0.05	22.1	1.17	0.85	0.32	34.10
28.6	0.08	22.2	1.23	0.77	0.46	34.62
30.1	-0.17	22.7	1.09	0.71	0.38	34.35
30.8	-0.07	21.6	0.93	0.69	0.25	33.83
31.1	-0.37	21.7	0.67	0.68	-0.01	32.90
31.7	-0.37	22.2	0.76	0.67	0.09	33.26
32.3	-0.70	22.6	0.53	0.67	-0.14	32.42

33.7	-0.37	22.1	0.74	0.67	0.07	33.19
38.8	-0.06	21.7	0.97	0.55	0.43	34.50
43.9	-0.43	21.6	0.58	0.64	-0.05	32.72

Table C4: Paleosalinity reconstruction dataset for *G. menardii*.

G. menardii_(lThm)						
(Age (ka)	**$\delta^{18}O_{G.menardii}$ (VPDB)**	**T (°C)**	**δ^{18}Osw (VSMOW)**	**$\delta^{18}O_{GIV}$**	**δ^{18}Osw (GIV corrected)**	**Salinity**
6.0	-0.89	16.4	-1.03	0.03	-1.07	28.97
6.2	0.48	17.5	0.58	0.04	0.54	34.93
7.1	0.00	20.7	0.82	0.06	0.76	35.74
8.6	-0.06	20.7	0.75	0.14	0.61	35.18
9.3	-0.04	21.8	1.03	0.21	0.82	35.95
10.3	-0.46	22.8	0.81	0.32	0.49	34.74
11.4	1.08	20.7	1.90	0.43	1.46	38.35
13.2	1.11	17.5	1.22	0.65	0.56	35.02
14.7	0.94	19.7	1.54	0.81	0.73	35.61
17.1	1.18	19.2	1.66	0.97	0.69	35.49
18.3	1.44	16.4	1.32	1.01	0.31	34.06
19.8	2.06	15.8	1.80	1.04	0.76	35.73
21.2	1.10	17.8	1.28	1.03	0.25	33.86
22.7	0.45	16.0	0.23	1.00	-0.77	30.08
23.9	0.00	15.8	-0.27	0.97	-1.24	28.34
24.1	0.40	18.8	0.81	0.97	-0.16	32.33
24.2	1.33	17.1	1.36	0.97	0.39	34.38
25.0	0.23	17.4	0.33	0.94	-0.61	30.67
26.0	0.76	17.6	0.90	0.90	0.00	32.91
27.1	0.01	17.8	0.19	0.85	-0.66	30.47
28.6	0.26	17.8	0.43	0.77	-0.34	31.66
30.1	0.24	20.6	1.03	0.71	0.32	34.11
30.8	0.85	18.4	1.17	0.69	0.48	34.70

31.1	0.21	20.2	0.92	0.68	0.24	33.80
31.5	0.20	19.2	0.69	0.68	0.02	32.98
31.7	0.44	19.2	0.92	0.67	0.24	33.83
32.3	0.38	19.2	0.86	0.67	0.20	33.65
33.7	0.68	18.5	1.01	0.67	0.34	34.19
38.8	0.12	17.3	0.18	0.55	-0.36	31.59
43.9	0.75	19.2	1.24	0.64	0.60	35.16

*The dark orange colour represents the unavailability of the actual data from the specific age which has been replaced by the linear Gaussian mean value.

Bibliography

AD, D., 1839. Foraminifères. In: de la Sagra R (ed) Histoire Physique, Politique et Naturelle de I'Ile de Cuba. Arthus Bertrand, Paris 1–51.

Adkins, Jess F., Boyle, E.A., 1997. Changing atmospheric $\Delta^{14}C$ and the record of deep water paleoventilation ages. Paleoceanography 12, 337–344. https://doi.org/10.1029/97PA00379

Adkins, Jess F, Boyle, E.A., 1997. Changing atmospheric $\Delta^{14}C$ and the record of deep water paleoventilation ages. Paleoceanography 12, 337–344. https://doi.org/10.1029/97PA00379

American Meteorological Society., 2018. Ocean studies : introduction to oceanography. American Meteorological Society.

Anand, P., Elderfield, H., Conte, M.H., 2003. Calibration of Mg/Ca thermometry in planktonic foraminifera from a sediment trap time series. Paleoceanography 18. https://doi.org/10.1029/2002pa000846

Bouvier-Soumagnac, Y. and Duplessy, J.C., 1985. Carbon and oxygen isotopic composition of planktonic foraminifera from laboratory culture, plankton tows and recent sediment; implications for the reconstruction of paleoclimatic conditions and of the global carbon cycle. The Journal of Foraminiferal Research, 15(4), pp.302-320.

Annamalai, H., Liu, P., Xie, S.P., 2005. Southwest Indian Ocean SST variability: Its local effect and remote influence on Asian monsoons. J. Clim. 18, 4150–4167. https://doi.org/10.1175/JCLI3533.1

Banakar, V.K., Mahesh, B.S., Burr, G., Chodankar, A.R., 2010a. Climatology of the Eastern Arabian Sea during the last glacial Cycle reconstructed from paired measurement of foraminiferal $\delta^{18}O$ and Mg/Ca. Quat. Res. 73, 535–540. https://doi.org/10.1016/j.yqres.2010.02.002

Banakar, V.K., Mahesh, B.S., Burr, G., Chodankar, A.R., 2010b. Climatology of the Eastern Arabian Sea during the last glacial Cycle reconstructed from paired measurement of foraminiferal $\delta\ ^{8}O$ and Mg/Ca. Quat. Res. 73, 535–540. https://doi.org/10.1016/j.yqres.2010.02.002

Barker, S., Greaves, M., Elderfield, H., 2003. A study of cleaning procedures used for foraminiferal Mg/Ca paleothermometry. Geochem. Geophys. Geosyst 4, 8407. https://doi.org/10.1029/2003GC000559

Be, A.W., 1977. An ecological, zoogeographic and taxonomic review of recent planktonic foraminifera. Ocean. Micropaleontol. 1–100.

Bender, M.L., 2013. Paleoclimate. Princeton University Press. https://doi.org/10.1515/9781400846375

Benson, L. V., Burdett, J.W., Kashgarian, M., Lund, S.P., Phillips, F.M., Rye, R.O., 1996. Climatic and Hydrologic Oscillations in the Owens Lake Basin and Adjacent Sierra Nevada, California. Science, 274, 746–749. https://doi.org/10.1126/science.274.5288.746

Benway, H.M., Mix, A.C., 2004. Oxygen isotopes, upper-ocean salinity, and precipitation sources in the eastern tropical Pacific. Earth Planet. Sci. Lett. 224, 493–507. https://doi.org/10.1016/j.epsl.2004.05.014

Benway, H.M., Mix, A.C., Haley, B.A., Klinkhammer, G.P., 2006. Eastern Pacific Warm Pool paleosalinity and climate variability: 0-30 kyr. Paleoceanography 21, 1–11. https://doi.org/10.1029/2005PA001208

Berger, W.H., 1969. Ecologic patterns of living planktonic Foraminifera. Deep Sea Res. Oceanogr. Abstr. 16, 1–24. https://doi.org/10.1016/0011-7471(69)90047-3

Berndt, M.E., Seyfried, W.E., Beck, J.W., 1988. Hydrothermal alteration processes at midocean ridges: experimental and theoretical constraints from Ca and Sr exchange reactions and Sr isotopic ratios. J. Geophys. Res. 93, 4573–4583. https://doi.org/10.1029/JB093iB05p04573

Bharti, N., 2021. Quaternary Ventilation of the Indian Ocean Deep Basins , Foraminiferal Isotopic and Abundance Approach (Ph.D Thesis).

Bharti, N., Bhushan, R., Skinner, L., Muruganantham, M., Jena, P.S., Dabhi, A., Shivam, A., 2022. Evidence of poorly ventilated deep Central Indian Ocean during the last glaciation. Earth Planet. Sci. Lett. 582, 117438. https://doi.org/10.1016/J.EPSL.2022.117438

Bhushan, R., Yadava, M., Shah, M.S., Banerji, U.S., Raj, H., Shah, C., Dabhi, A.J., 2019a. First results from the PRL accelerator mass spectrometer. Curr. Sci. 116(3), 361–363.

Bhushan, R., Yadava, M., Shah, M.S., Raj, H., 2019b. Performance of a new 1MV AMS facility (AURiS) at PRL, Ahmedabad, India. Nucl. Instruments Methods Phys. Res. Sect. B Beam Interact. with Mater. Atoms 439, 76--79. https://doi.org/https://doi.org/10.1016/j.nimb.2018.12.003

Bijma, J., Hemleben, C., Huber, B.T., Erlenkeuser, H., Kroon, D., 1998. Experimental determination of the ontogenetic stable isotope variability in two morphotypes of Globigerinella siphonifera (d'Orbigny). Mar. Micropaleontol. 35, 141–160. https://doi.org/10.1016/S0377-8398(98)00017-6

Blaauw, M., Christeny, J.A., 2011. Flexible paleoclimate age-depth models using an autoregressive gamma process. Bayesian Anal. 6, 457–474. https://doi.org/10.1214/11-BA618

Boaretto, E., Bryant, C., Carmi, I., Cook, G., Gulliksen, S., Harkness, D., Heinemeier, J., McClure, J., McGee, E., Naysmith, P., Possnert, G., Scott, M., van der Plicht, H., van Strydonck, M., 2002. Summary findings of the fourth international radiocarbon intercomparison (FIRI)(1998-2001). J. Quat. Sci. 17, 633–637. https://doi.org/10.1002/jqs.702

Boccaletti, G., 2005. Timescales and dynamics of the formation of a thermocline. Dyn. Atmos. Ocean. 39, 21–40. https://doi.org/10.1016/j.dynatmoce.2004.10.010

Boccaletti, G., Pacanowski, R.C., George, S., Philander, H. and Fedorov, A.V., 2004. The thermal structure of the upper ocean. Journal of physical oceanography, 34(4), pp.888-902.

Bond, G., Broecker, W., Johnsen, S., McManus, J., Labeyrie, L., Jouzel, J., Bonani, G., 1993. Correlations between climate records from North Atlantic sediments and Greenland ice. Nature 365, 143–147. https://doi.org/10.1038/365143a0

Bonnefille, R., Chalie, F., 2000. Pollen-inferred precipitation time-series from equatorial mountains, Africa, the last 40 kyr BP. Glob. Planet. Change 26, 25–50. https://doi.org/10.1016/S0921-8181(00)00032-1

Bradley, R.S., 2015. Paleoclimatic Reconstruction, in: Paleoclimatology. Elsevier, pp. 1–11. https://doi.org/10.1016/B978-0-12-386913-5.00001-6

Broecker, W., Barker, S., 2007. A 190‰ drop in atmosphere's $\Delta^{14}C$ during the "Mystery

Interval" (17.5 to 14.5 kyr). Earth Planet. Sci. Lett. 256, 90–99. https://doi.org/10.1016/j.epsl.2007.01.015

Broecker, W., Bond, G., Klas, M., Clark, E., McManus, J., 1992. Origin of the northern Atlantic's Heinrich events. Clim. Dyn. 6, 265–273. https://doi.org/10.1007/BF00193540

Broecker, W., Matsumoto, K., Clark, E., Hajdas, I., Bonani, G., 1999. Radiocarbon age differences between coexisting foraminiferal species. Paleoceanography 14, 431–436. https://doi.org/10.1029/1999PA900019

Broecker, W.S., Andree, M., Bonani, G., Wolfli, W., Oeschger, H., Klas, M., Mix, A., Curry, W., 1988. Preliminary estimates for the radiocarbon age of deep water in the glacial ocean. Paleoceanography 3, 659–669. https://doi.org/10.1029/PA003i006p00659

Broecker, W.S., Peng, T.-H., Trumbore, S., Bonani, G., Wolfli, W., 1990. The distribution of radiocarbon in the glacial ocean. Global Biogeochem. Cycles 4, 103–117. https://doi.org/10.1029/GB004i001p00103

Bryan, S.P., Marchitto, T.M., Lehman, S.J., 2010. The release of ^{14}C-depleted carbon from the deep ocean during the last deglaciation: Evidence from the Arabian Sea. Earth Planet. Sci. Lett. 298, 244–254. https://doi.org/10.1016/J.EPSL.2010.08.025

Carvallo, C., Camps, P., Ruffet, G., Henry, B., Poidras, T., 2003. Mono Lake or Laschamp geomagnetic event recorded from lava flows in Amsterdam Island (southeastern Indian Ocean), Geophys. J. Int.

Chandana, K.R., Banerji, U.S., Bhushan, R., 2018. Review on Indian Summer Monsoon (ISM) Reconstruction since LGM from Northern Indian Ocean. Earth Sci. India 11, 71–84.

Chinni, V., Singh, S.K., 2022. Dissolved iron cycling in the Arabian Sea and sub-tropical gyre region of the Indian Ocean. Geochim. Cosmochim. Acta 317, 325–348. https://doi.org/10.1016/j.gca.2021.10.026

Chu, P.C., Fan, C., 2019. Global ocean synoptic thermocline gradient, isothermal-layer depth, and other upper ocean parameters. Sci. Data 6, 119. https://doi.org/10.1038/s41597-019-0125-3

Clark, P.U., Dyke, A.S., Shakun, J.D., Carlson, A.E., Clark, J., Wohlfarth, B., Mitrovica, J.X., Hostetler, S.W. and McCabe, A.M., 2009. The last glacial maximum. science, 325(5941), pp.710-714.

Craig, H., Gordon, L.I., 2013. University-Nanjing University of Information Technology Center for Atmospheric Environment Yale-NUIST Center on Atmospheric Environment Deuterium and oxygen 18 variations in the ocean and the marine atmosphere.

Crosta, X., Koç, N., 2007. Proxies in Late Cenozoic Paleoceanography, Developments in Marine Geology.

De Pol-Holz, R., Keigwin, L., Southon, J., Hebbeln, D., Mohtadi, M., 2010. No signature of abyssal carbon in intermediate waters off Chile during deglaciation. Nat. Geosci. 3, 192–195. https://doi.org/10.1038/ngeo745

Dekens, P.S., Lea, D.W., Pak, D.K., Spero, H.J., 2002. Core top calibration of Mg/Ca in tropical foraminifera: Refining paleotemperature estimation. Geochemistry, Geophys. Geosystems 3, 1–29. https://doi.org/10.1029/2001GC000200

Divakar Naidu, P., Malmgren, B.A., 1999. Quaternary carbonate record from the equatorial Indian Ocean and its relationship with productivity changes. Mar. Geol. 161, 49–62. https://doi.org/10.1016/S0025-3227(99)00055-9

Du, Y., Zhang, Y., Zhang, L., Tozuka, T., Ng, B., Cai, W., 2020. Thermocline Warming Induced Extreme Indian Ocean Dipole in 2019. Geophys. Res. Lett. 47. https://doi.org/10.1029/2020GL090079

Duplessy, J.C., Bé, A.W.H., Blanc, P.L., 1981. Oxygen and carbon isotopic composition and biogeographic distribution of planktonic foraminifera in the Indian Ocean. Palaeogeogr. Palaeoclimatol. Palaeoecol. 33, 9–46. https://doi.org/10.1016/0031-0182(81)90031-6

Dutta, K., Bhushan, R., B.L.K., S., 2001. ΔR correction values for the Northern Indian Ocean. Radiocarbon 483–488.

Elderfield, H., Ganssen, G., 2000a. Past temperature and $\delta^{18}O$ of surface ocean waters inferred from foraminiferal Mg/Ca ratios. Nature. https://doi.org/10.1038/35013033

Elderfield, H., Ganssen, G., 2000b. Past temperature and $\delta^{18}O$ of surface ocean waters inferred from foraminiferal Mg/Ca ratios. Nature 405, 442–445. https://doi.org/10.1038/35013033

Erez, J., Luz, B., 1983. Experimental paleotemperature equation for planktonic foraminifera. Geochim. Cosmochim. Acta 47, 1025–1031. https://doi.org/10.1016/0016-7037(83)90232-6

Fairbanks, R.G., 1989. A 17,000-year glacio-eustatic sea level record: influence of glacial melting rates on the Younger Dryas event and deep-ocean circulation. Nature 342, 637–642. https://doi.org/10.1038/342637a0

Fairbanks, R.G., Sverdlove, M., Free, R., Wiebe, P.H., Bé, A.W.H., 1982. Vertical distribution and isotopic fractionation of living planktonic foraminifera from the Panama Basin. Nature 298, 841–844. https://doi.org/10.1038/298841a0

Fiedler, P.C., 2010. Comparison of objective descriptions of the thermocline. Limnol. Oceanogr. Methods 8, 313–325. https://doi.org/10.4319/LOM.2010.8.313

Ford, H.L., McChesney, C.L., Hertzberg, J.E., McManus, J.F., 2018. A Deep Eastern Equatorial Pacific Thermocline During the Last Glacial Maximum. Geophys. Res. Lett. 45, 11,806-11,816. https://doi.org/10.1029/2018GL079710

Gillot, P.-Y., Nativel, P., 1982. K□Ar chronology of the ultimate activity of piton des neiges volcano, reunion island, Indian ocean. J. Volcanol. Geotherm. Res. 13, 131–146. https://doi.org/10.1016/0377-0273(82)90024-5

Godad, S.P., Panmei, C., Naidu, P.D., 2022a. Remote forcing of winter cooling in the Arabian Sea: Implications for the NE monsoon. Palaeogeogr. Palaeoclimatol. Palaeoecol. 586, 110755. https://doi.org/10.1016/J.PALAEO.2021.110755

Godad, S.P., Panmei, C., Naidu, P.D., 2022b. Remote forcing of winter cooling in the Arabian Sea: Implications for the NE monsoon. Palaeogeogr. Palaeoclimatol. Palaeoecol. 586, 110755. https://doi.org/10.1016/j.palaeo.2021.110755

Gordon, A., 2005. the Indonesian Seas. Oceanography 18, 14–27.

Gornitz, V. (Ed. ., 2009. Encyclopedia of paleoclimatology and ancient environments, Encyclopedia of earth sciences series. Springer, Dordrecht.

Gray, W.R., Weldeab, S., Lea, D.W., Rosenthal, Y., Gruber, N., Donner, B., Fischer, G., 2018. The effects of temperature, salinity, and the carbonate system on Mg/Ca in Globigerinoides ruber (white): A global sediment trap calibration. Earth Planet. Sci. Lett. 482, 607–620. https://doi.org/10.1016/j.epsl.2017.11.026

Greaves, M., Barker, S., Daunt, C., Elderfield, H., 2005. Accuracy, standardization, and interlaboratory calibration standards for foraminiferal Mg/Ca thermometry. Geochemistry, Geophys. Geosystems 6. https://doi.org/10.1029/2004GC000790

Groeneveld, J., Hathorne, E.C., Steinke, S., DeBey, H., Mackensen, A. and Tiedemann, R., 2014. Glacial induced closure of the Panamanian gateway during Marine Isotope Stages (MIS) 95–100 (~ 2.5 Ma). Earth and Planetary Science Letters, 404, pp.296-306.

Han, W., McCreary, J.P., 2001. Modeling salinity distributions in the Indian Ocean. J. Geophys. Res. Ocean. 106, 859–877. https://doi.org/10.1029/2000JC000316

Haridas, N. V., Banerji, U.S., Maya, K., Padmalal, D., 2022. Paleoclimatic and paleoceanographic records from the Bay of Bengal sediments during the last 30 ka. J. Asian Earth Sci. 229. https://doi.org/10.1016/j.jseaes.2022.105169

Hastings, D.W., Russell, A.D., Emerson, S.R., 1998. Foraminiferal magnesium in Globeriginoides sacculifer as a paleotemperature proxy. Paleoceanography 13, 161–169. https://doi.org/10.1029/97PA03147

Heaton, T., Köhler, P., Butzin, M., Bard, E., Reimer, R., Austin, W., Bronk Ramsey, C., Grootes, P., # Hughen KA, Kromer B, Reimer PJ, Adkins J, Burke A, Cook MS, Olsen J, S.L., 2020. Marine20-the marine radiocarbon age calibration curve (0-55,000 cal BP). https://doi.org/10.1017/RDC.2020.68

Held, I.M., Soden, B.J., 2006. Robust Responses of the Hydrological Cycle to Global Warming. J. Clim. 19, 5686–5699. https://doi.org/10.1175/JCLI3990.1

Hemleben, C., Be, A.W.H., Anderson, O.R., Tuntivate, S., 1977. Test morphology, organic layers and chamber formation of the planktonic foraminifer Globorotalia menardii (d'Orbigny). J. Foraminifer. Res. 7, 1–25. https://doi.org/10.2113/gsjfr.7.1.1

Holland, K., Branson, O., Haynes, L.L., Hönisch, B., Allen, K.A., Russell, A.D., Fehrenbacher, J.S., Spero, H.J., Eggins, S.M., 2020. Constraining multiple controls on planktic foraminifera Mg/Ca. Geochim. Cosmochim. Acta 273, 116–136. https://doi.org/10.1016/j.gca.2020.01.015

Hollstein, M., Mohtadi, M., Rosenthal, Y., Moffa Sanchez, P., Oppo, D., Martínez Méndez, G., Steinke, S., Hebbeln, D., 2017a. Stable Oxygen Isotopes and Mg/Ca in Planktic Foraminifera From Modern Surface Sediments of the Western Pacific Warm Pool: Implications for Thermocline Reconstructions. Paleoceanography 32, 1174–1194. https://doi.org/10.1002/2017PA003122

Hollstein, M., Mohtadi, M., Rosenthal, Y., Moffa Sanchez, P., Oppo, D., Martínez Méndez,

G., Steinke, S., Hebbeln, D., 2017b. Stable Oxygen Isotopes and Mg/Ca in Planktic Foraminifera From Modern Surface Sediments of the Western Pacific Warm Pool: Implications for Thermocline Reconstructions. Paleoceanography 32, 1174–1194. https://doi.org/10.1002/2017PA003122

Hollstein, M., Mohtadi, M., Rosenthal, Y., Moffa Sanchez, P., Oppo, D., Martínez Méndez, G., Steinke, S., Hebbeln, D., 2017c. Stable Oxygen Isotopes and Mg/Ca in Planktic Foraminifera From Modern Surface Sediments of the Western Pacific Warm Pool: Implications for Thermocline Reconstructions. Paleoceanography. https://doi.org/10.1002/2017PA003122

Hughen, K.A., 2007. Chapter Five Radiocarbon Dating of Deep-Sea Sediments. pp. 185–210. https://doi.org/10.1016/S1572-5480(07)01010-X

Jensen, T.G., 2003. Cross-equatorial pathways of salt and tracers from the northern Indian Ocean: Modelling results. Deep Sea Res. Part II Top. Stud. Oceanogr. 50, 2111–2127. https://doi.org/10.1016/S0967-0645(03)00048-1

Jung, S.J.A., Kroon, D., Ganssen, G., Peeters, F., Ganeshram, R., 2009. Enhanced Arabian Sea intermediate water flow during glacial North Atlantic cold phases. Earth Planet. Sci. Lett. 280, 220–228. https://doi.org/10.1016/j.epsl.2009.01.037

Kadko, D., Baross, J., Alt, J., 1995. The magnitude and global implications of hydrothermal flux. Geophys. Monogr. Ser. 91, 446–466. https://doi.org/10.1029/GM091p0446

Kara, A.B., Rochford, P.A., Hurlburt, H.E., 2000. An optimal definition for ocean mixed layer depth. J. Geophys. Res. Ocean. 105, 16803–16821. https://doi.org/10.1029/2000JC900072

Kawagata, S., Hayward, B.W., Gupta, A.K., 2006. Benthic foraminiferal extinctions linked to late Pliocene–Pleistocene deep-sea circulation changes in the northern Indian Ocean (ODP Sites 722 and 758). Mar. Micropaleontol. 58, 219–242. https://doi.org/10.1016/j.marmicro.2005.11.003

Kessler, W.S., 1990. Observations of long Rossby waves in the northern tropical Pacific. J. Geophys. Res. 95, 5183. https://doi.org/10.1029/JC095iC04p05183

Kessler, W.S., McPhaden, M.J., Weickmann, K.M., 1995. Forcing of intraseasonal Kelvin waves in the equatorial Pacific. J. Geophys. Res. 100, 10613.

https://doi.org/10.1029/95JC00382

Kiefer, T., McCave, I.N., Elderfield, H., 2006a. Antarctic control on tropical Indian Ocean sea surface temperature and hydrography. Geophys. Res. Lett. 33. https://doi.org/10.1029/2006GL027097

Kiefer, T., McCave, I.N., Elderfield, H., 2006b. Antarctic control on tropical Indian Ocean sea surface temperature and hydrography. Geophys. Res. Lett. 33, L24612. https://doi.org/10.1029/2006GL027097

Kim, S.-T., O'neil, J.R., 1997. Equilibrium and nonequilibrium oxygen isotope effects in synthetic carbonates, Geochimica et Cosmochimica Acta.

Klein, M., Mous, D.J.W., Gottdang, A., 2004. Fast and Accurate Sequential Injection AMS with Gated Faraday Cup Current Measurement. Radiocarbon 46, 77–82. https://doi.org/10.1017/S0033822200039370

Klein, M.G., Mous, D.J.W., Gottdang, A., 2006. A compact 1MV multi-element AMS system. Nucl. Instruments Methods Phys. Res. Sect. B Beam Interact. with Mater. Atoms 249, 764–767. https://doi.org/10.1016/j.nimb.2006.03.135

Kuhnt, W., Holbourn, A., Hall, R., Zuvela, M., Käse, R., 2004. Neogene history of the indonesian throughflow, in: Geophysical Monograph Series. Blackwell Publishing Ltd, pp. 299–320. https://doi.org/10.1029/149GM16

Kumar, S.P., Prasad, T.G., 1999. Formation and spreading of Arabian Sea high-salinity water mass. J. Geophys. Res. Ocean. 104, 1455–1464. https://doi.org/10.1029/1998JC900022

Kwiatkowski, C., Prange, M., Varma, V., Steinke, S., Hebbeln, D., Mohtadi, M., 2015. Holocene variations of thermocline conditions in the eastern tropical Indian Ocean. Quat. Sci. Rev. 114, 33–42. https://doi.org/10.1016/J.QUASCIREV.2015.01.028

Lalou, C., Münch, U., Halbach, P., Reyss, J.L., 1998. Radiochronological investigation of hydrothermal deposits from the MESO zone, Central Indian Ridge. Mar. Geol. 149, 243–254. https://doi.org/10.1016/S0025-3227(98)00042-5

Lebrato, M., Garbe-Schönberg, D., Müller, M.N., Blanco-Ameijeiras, S., Feely, R.A., Lorenzoni, L., Molinero, J.-C., Bremer, K., Jones, D.O.B., Iglesias-Rodriguez, D., Greeley, D., Lamare, M.D., Paulmier, A., Graco, M., Cartes, J., Barcelos e Ramos, J., de Lara, A., Sanchez-Leal, R., Jimenez, P., Paparazzo, F.E., Hartman, S.E., Westernströer,

U., Küter, M., Benavides, R., da Silva, A.F., Bell, S., Payne, C., Olafsdottir, S., Robinson, K., Jantunen, L.M., Korablev, A., Webster, R.J., Jones, E.M., Gilg, O., Bailly du Bois, P., Beldowski, J., Ashjian, C., Yahia, N.D., Twining, B., Chen, X.-G., Tseng, L.-C., Hwang, J.-S., Dahms, H.-U., Oschlies, A., 2020. Global variability in seawater Mg:Ca and Sr:Ca ratios in the modern ocean. Proc. Natl. Acad. Sci. 117, 22281–22292. https://doi.org/10.1073/pnas.1918943117

Levi, C., Labeyrie, L., Bassinot, F., Guichard, F., Cortijo, E., Waelbroeck, C., Caillon, N., Duprat, J., de Garidel-Thoron, T., Elderfield, H., 2007. Low-latitude hydrological cycle and rapid climate changes during the last deglaciation. Geochemistry, Geophys. Geosystems 8, n/a-n/a. https://doi.org/10.1029/2006GC001514

Lim, D., Kim, H., Kim, J., Jeong, D., Kim, D., 2020. Mercury proxy for hydrothermal and submarine volcanic activities in the sediment cores of Central Indian Ridge. Mar. Pollut. Bull. 159, 111513. https://doi.org/10.1016/j.marpolbul.2020.111513

Lim, D., Kim, Jihun, Kim, Jonguk, Kim, D., Jeong, D., Kim, H., Xu, Z., 2021. Enhancement of volcanic eruption in mid-ocean ridge during the last deglaciation: New sedimentary evidence in the middle part of Central Indian Ridge. Mar. Geol.

Lisiecki, L.E., Raymo, M.E., 2005. A Pliocene-Pleistocene stack of 57 globally distributed benthic $\delta^{18}O$ records. Paleoceanography 20, n/a-n/a. https://doi.org/10.1029/2004PA001071

Liu, S., Ye, W., Cao, P., Zhang, H., Chen, M. Te, Li, X., Li, J., Pan, H.J., Khokiattiwong, S., Kornkanitnan, N., Shi, X., 2021. Paleoclimatic responses in the tropical Indian Ocean to regional monsoon and global climate change over the last 42 kyr. Mar. Geol. 438, 106542. https://doi.org/10.1016/J.MARGEO.2021.106542

Liu, S., Yuan, C., Luo, J., Ma, X., Zhou, X., Yamagata, T., 2023. Weakening of the Indian Ocean Dipole in the mid-Holocene due to the mean oceanic climatology change. J. Clim. 1–35. https://doi.org/10.1175/JCLI-D-22-0878.1

Liu, Z., Yang, H., 2003. Extratropical control of tropical climate, the atmospheric bridge and oceanic tunnel. https://doi.org/10.1029/2002GL016492

Longhurst, A., Sathyendranath, S., Platt, T., Caverhill, C., 1995. An estimate of global primary production in the ocean from satellite radiometer data. J. Plankton Res. 17, 1245–1271.

https://doi.org/10.1093/plankt/17.6.1245

Luyten, J.R., Pedlosky, J. and Stommel, H., 1983. The ventilated thermocline. Journal of Physical Oceanography, 13(2), pp.292-309.

Lynch-Stieglitz, J., Marchitto, T.M., 2013. Tracers of Past Ocean Circulation. Treatise Geochemistry Second Ed. 8, 435–452. https://doi.org/10.1016/B978-0-08-095975-7.00616-1

Mahesh, B.S., Banakar, V.K., 2014. Change in the intensity of low-salinity water inflow from the Bay of Bengal into the Eastern Arabian Sea from the Last Glacial Maximum to the Holocene: Implications for monsoon variations. Palaeogeogr. Palaeoclimatol. Palaeoecol. 397, 31–37. https://doi.org/10.1016/j.palaeo.2013.05.024

Mangini, A., Godoy, J.M., Godoy, M.L., Kowsmann, R., Santos, G.M., Ruckelshausen, M., Schroeder-Ritzrau, A., Wacker, L., 2010. Deep sea corals off Brazil verify a poorly ventilated Southern Pacific Ocean during H2, H1 and the Younger Dryas. Earth Planet. Sci. Lett. 293, 269–276. https://doi.org/10.1016/j.epsl.2010.02.041

Marchitto, T.M., Lehman, S.J., Ortiz, J.D., Flückiger, J. and van Geen, A., 2007. Marine radiocarbon evidence for the mechanism of deglacial atmospheric CO2 rise. science, 316(5830), pp.1456-1459.

Marty, B., Meynier, V., Nicolini, E., Griesshaber, E., Toutain, J.P., 1993. Geochemistry of gas emanations: A case study of the Réunion Hot Spot, Indian Ocean. Appl. Geochemistry 8, 141–152. https://doi.org/10.1016/0883-2927(93)90030-K

Massoth, G.J., 1994. Temporal and spatial variability of hydrothermal manganese and iron at Cleft segment, Juan de Fuca Ridge. J. Geophys. Res. 99, 4905–4923. https://doi.org/10.1029/93JB02799

McCreary, J.P., Miyama, T., Furue, R., Jensen, T., Kang, H.-W., Bang, B., Qu, T., 2007. Interactions between the Indonesian Throughflow and circulations in the Indian and Pacific Oceans. Prog. Oceanogr. 75, 70–114. https://doi.org/10.1016/j.pocean.2007.05.004

Merino-Campos, V., De Pol-Holz, R., Southon, J., Latorre, C., Collado-Fabbri, S., 2019. Marine Radiocarbon Reservoir Age Along the Chilean Continental Margin. Radiocarbon 61, 195–210. https://doi.org/10.1017/RDC.2018.81

Meyers, G., 1987., 1987. Observed and modeled topography of the 20-degrees-C isotherm in the Tropical Pacific. Oceanol. acta 10, 41–48.

Mix, A., 2001. Environmental processes of the ice age: land, oceans, glaciers (EPILOG). Quat. Sci. Rev. 20, 627–657. https://doi.org/10.1016/S0277-3791(00)00145-1

Mochizuki, T., Kimoto, M., Watanabe, M., Chikamoto, Y., Ishii, M., 2016. Interbasin effects of the Indian Ocean on Pacific decadal climate change. Geophys. Res. Lett. 43, 7168–7175. https://doi.org/10.1002/2016GL069940

Mohtadi, M., 2009. Low‐latitude control on seasonal and interannual changes in planktonic foraminiferal flux and shell geochemistry off south Java: A sediment trap study. https://doi.org/10.1029/2008PA001636

Mohtadi, M., Lückge, A., Steinke, S., Groeneveld, J., Hebbeln, D., Westphal, N., 2010a. Late Pleistocene surface and thermocline conditions of the eastern tropical Indian Ocean. Quat. Sci. Rev. 29, 887–896. https://doi.org/10.1016/j.quascirev.2009.12.006

Mohtadi, M., Prange, M., Oppo, D.W., De Pol-Holz, R., Merkel, U., Zhang, X., Steinke, S., Lückge, A., 2014. North Atlantic forcing of tropical Indian Ocean climate. https://doi.org/10.1038/nature13196

Mohtadi, M., Steinke, S., Groeneveld, J., Fink, H.G., Rixen, T., Hebbeln, D., Donner, B., Herunadi, B., 2009. Low-latitude control on seasonal and interannual changes in planktonic foraminiferal flux and shell geochemistry off south Java: A sediment trap study. Paleoceanography 24, n/a-n/a. https://doi.org/10.1029/2008PA001636

Mohtadi, M., Steinke, S., Lückge, A., Groeneveld, J., Hathorne, E.C., 2010b. Glacial to Holocene surface hydrography of the tropical eastern Indian Ocean. Earth Planet. Sci. Lett. 292, 89–97. https://doi.org/10.1016/J.EPSL.2010.01.024

Monterey, Grigory Isayev, 1954-1999 ; Levitus, S., 1997. Seasonal variability of mixed layer depth for the world ocean. NOAA atlas NESDIS 14.

Mulitza, S., Boltovskoy, D., Donner, B., Meggers, H., Paul, A., Wefer, G., 2003. Temperature: $\delta^{18}O$ relationships of planktonic foraminifera collected from surface waters. Palaeogeogr. Palaeoclimatol. Palaeoecol. 202, 143–152. https://doi.org/10.1016/S0031-0182(03)00633-3

Naidu, P.D., Govil, P., 2010. New evidence on the sequence of deglacial warming in the

tropical Indian Ocean. J. Quat. Sci. 25, 1138–1143. https://doi.org/10.1002/jqs.1392

Naidu, P.D., Malmgren, B.A., 1996. A High-resolution record of Late Quaternary upwelling along the Oman Margin, Arabian Sea based on planktonic foraminifera. Paleoceanography 11, 129–140. https://doi.org/10.1029/95PA03198

Němec, M., Wacker, L., Gäggeler, H., 2010. Optimization of the Graphitization Process at Age-1. Radiocarbon 52, 1380–1393. https://doi.org/10.1017/S0033822200046464

Nilsson-Kerr, K., Anand, P., Sexton, P.F., Leng, M.J., Misra, S., Clemens, S.C., Hammond, S.J., 2019. Role of Asian summer monsoon subsystems in the inter-hemispheric progression of deglaciation. Nat. Geosci. 12, 290–295. https://doi.org/10.1038/s41561-019-0319-5

Nürnberg, D., Bijma, J., Hemleben, C., 1996. Assessing the reliability of magnesium in foraminiferal calcite as a proxy for water mass temperatures. Geochim. Cosmochim. Acta 60, 803–814. https://doi.org/10.1016/0016-7037(95)00446-7

Pagani, M., Liu, Z., LaRiviere, J., Ravelo, A.C., 2010. High Earth-system climate sensitivity determined from Pliocene carbon dioxide concentrations. Nat. Geosci. 3, 27–30. https://doi.org/10.1038/ngeo724

Pahnke, K., Goldstein, S.L., Hemming, S.R., 2008. Abrupt changes in Antarctic Intermediate Water circulation over the past 25,000 years. Nat. Geosci. 1, 870–874. https://doi.org/10.1038/ngeo360

Panchang, R., Nigam, R., Riedel, F., Janssen, A.W., Hla, U.K.Y., 2007. A review of the studies on pteropods from the northern Indian Ocean region with a report on the pteropods of Irrawaddy continental shelf off Myanmar (Burma). Indian J. Mar. Sci. 36, 384–398.

Pang, X., Bassinot, F., Sepulcre, S., 2021. Indonesian Throughflow variability over the last two glacial-interglacial cycles: Evidence from the eastern Indian Ocean. Quat. Sci. Rev. 256, 106839. https://doi.org/10.1016/J.QUASCIREV.2021.106839

Pang, X., Bassinot, F., Sepulcre, S., 2020. Cleaning method impact on the Mg/Ca of three planktonic foraminifer species: A downcore study along a depth transect. Chem. Geol. 549, 119690. https://doi.org/10.1016/j.chemgeo.2020.119690

Parker, W.K., Rupert Jones, T., Brady, H.B., 1865. IV.— On the nomenclature of the Foraminifera. Ann. Mag. Nat. Hist. 16, 15–41.

https://doi.org/10.1080/00222936508679369

Pattan, J.N., Parthiban, G., Garg, A., Moraes, N.R.C., 2017. Intense reducing conditions during the last deglaciation and Heinrich events (H1, H2, H3) in sediments from the oxygen minimum zone off Goa, eastern Arabian Sea. Mar. Pet. Geol. 84, 243–256. https://doi.org/10.1016/j.marpetgeo.2017.03.034

Pena, L.D., Goldstein, S.L., Hemming, S.R., Jones, K.M., Calvo, E., Pelejero, C., Cacho, I., 2013. Rapid changes in meridional advection of Southern Ocean intermediate waters to the tropical Pacific during the last 30 kyr. Earth Planet. Sci. Lett. 368, 20–32. https://doi.org/10.1016/J.EPSL.2013.02.028

Pizarro, O., 2004. Interdecadal variability of the thermocline along the west coast of South America. Geophys. Res. Lett. 31, L20307. https://doi.org/10.1029/2004GL020998

Punyu, V.R., Banakar, V.K., Garg, A., 2014. Equatorial Indian Ocean productivity during the last 33kyr and possible linkage to Westerly Jet variability. Mar. Geol. 348, 44–51. https://doi.org/10.1016/J.MARGEO.2013.11.010

Qiu, Z., Han, X., Li, M., Wang, Y., Chen, X., Fan, W., Zhou, Y., Cui, R., Wang, L., 2021. The temporal variability of hydrothermal activity of Wocan hydrothermal field, Carlsberg Ridge, northwest Indian Ocean. Ore Geol. Rev.

Raj, H., 2020. High resolution paleoclimatic study using corals. Indian Institute of Technology Gandhinagar.

Rancon, J., 1985. Hydrothermal history of Piton des Neiges volcano (Reunion Island, Indian Ocean). J. Volcanol. Geotherm. Res.

Rashid, H., Flower, B.P., Poore, R.Z., Quinn, T.M., 2007. A ~25ka Indian Ocean monsoon variability record from the Andaman Sea. Quat. Sci. Rev. 26, 2586–2597. https://doi.org/10.1016/j.quascirev.2007.07.002

Regenberg, M., Steph, S., Nürnberg, D., Tiedemann, R., Garbe-Schönberg, D., 2009. Calibrating Mg/Ca ratios of multiple planktonic foraminiferal species with δ^{18}O-calcification temperatures: Paleothermometry for the upper water column. Earth Planet. Sci. Lett. 278, 324–336. https://doi.org/10.1016/J.EPSL.2008.12.019

Reimer, P.J., Austin, W.E.N., Bard, E., Bayliss, A., Blackwell, P.G., Bronk Ramsey, C., Butzin, M., Cheng, H., Edwards, R.L., Friedrich, M., Grootes, P.M., Guilderson, T.P.,

Hajdas, I., Heaton, T.J., Hogg, A.G., Hughen, K.A., Kromer, B., Manning, S.W., Muscheler, R., Palmer, J.G., Pearson, C., van der Plicht, J., Reimer, R.W., Richards, D.A., Scott, E.M., Southon, J.R., Turney, C.S.M., Wacker, L., Adolphi, F., Büntgen, U., Capano, M., Fahrni, S.M., Fogtmann-Schulz, A., Friedrich, R., Köhler, P., Kudsk, S., Miyake, F., Olsen, J., Reinig, F., Sakamoto, M., Sookdeo, A., Talamo, S., 2020. The IntCal20 Northern Hemisphere Radiocarbon Age Calibration Curve (0–55 cal kBP). Radiocarbon 62, 725–757. https://doi.org/10.1017/RDC.2020.41

Rein, B., Lückge, A., Reinhardt, L., Sirocko, F., Wolf, A., Dullo, W.-C., 2005. El Niño variability off Peru during the last 20,000 years. Paleoceanography 20, n/a-n/a. https://doi.org/10.1029/2004PA001099

Rippert, N., Baumann, K.H., Pätzold, J., 2015. Thermocline fluctuations in the western tropical Indian Ocean during the past 35 ka. J. Quat. Sci. 30, 201–210. https://doi.org/10.1002/jqs.2767

Rohling, E.J., Bigg, G.R., 1998. Paleosalinity and $\delta^{18}O$: A critical assessment. J. Geophys. Res. Ocean. 103, 1307–1318. https://doi.org/10.1029/97JC01047

Romahn, S., MacKensen, A., Groeneveld, J., Pätzold, J., 2014. Deglacial intermediate water reorganization: New evidence from the Indian Ocean. Clim. Past 10, 293–303. https://doi.org/10.5194/cp-10-293-2014

Ronge, T.A., Tiedemann, R., Lamy, F., Köhler, P., Alloway, B. V, De Pol-Holz, R., Pahnke, K., Southon, J., Wacker, L., 2016. Radiocarbon constraints on the extent and evolution of the South Pacific glacial carbon pool. Nat. Commun. 7. https://doi.org/10.1038/ncomms11487

Rongstad, B.L., Marchitto, T.M., Serrato Marks, G., Koutavas, A., Mekik, F., Ravelo, A.C., 2020. Investigating ENSO-Related Temperature Variability in Equatorial Pacific Core-Tops Using Mg/Ca in Individual Planktic Foraminifera. Paleoceanogr. Paleoclimatology 35. https://doi.org/10.1029/2019PA003774

Roth, R. and Joos, F., 2013. A reconstruction of radiocarbon production and total solar irradiance from the Holocene ^{14}C and CO_2 records: implications of data and model uncertainties. Climate of the Past, 9(4), pp.1879-1909. https://doi.org/10.5194/cp-9-1879-2013

Rozanski, K., Stichler, W., Gonfiantini, R., Scott, E.M., Beukens, R.P., Kromer, B., Van Der Plicht, J., 1992. The IAEA ^{14}C Intercomparison Exercise 1990. Radiocarbon 34, 506–519. https://doi.org/10.1017/S0033822200063761

Sagawa, T., Yokoyama, Y., Ikehara, M., Kuwae, M., 2012. Shoaling of the western equatorial Pacific thermocline during the last glacial maximum inferred from multispecies temperature reconstruction of planktonic foraminifera. Palaeogeogr. Palaeoclimatol. Palaeoecol. 346–347, 120–129. https://doi.org/10.1016/j.palaeo.2012.06.002

Saint-Ange, F., Bachèlery, P., Babonneau, N., Michon, L., Jorry, S.J., 2013. Volcaniclastic sedimentation on the submarine slopes of a basaltic hotspot volcano: Piton de la fournaise volcano (la réunion island, indian ocean). Mar. Geol. 337, 35–52. https://doi.org/10.1016/j.margeo.2013.01.004

Saji, N., Yamagata, T., 2003. Possible impacts of Indian Ocean Dipole mode events on global climate. Clim. Res. 25, 151–169. https://doi.org/10.3354/cr025151

Saji, N.H., Goswami, B.N., Vinayachandran, P.N., Yamagata, T., 1999. A dipole mode in the tropical Indian Ocean. Nature 401, 360–363. https://doi.org/10.1038/43854

Sanchez-Franks, A., Webber, B.G.M., King, B.A., Vinayachandran, P.N., Matthews, A.J., Sheehan, P.M., Behara, A., Neema, C.P., 2019. The railroad switch effect of seasonally reversing currents on the Bay of Bengal high-salinity core. Geophys. Res. Lett. 46(11), 6005–6014.

Saraswat, R., Nigam, R., Weldeab, S., Mackensen, A., Naidu, P.D., 2005. A first look at past sea surface temperatures in the equatorial Indian Ocean from Mg/Ca in foraminifera. Geophys. Res. Lett. 32, L24605. https://doi.org/10.1029/2005GL024093

Saraswat, R., Suokhrie, T., Naik, D.K., Singh, D.P., Saalim, S.M., Salman, M., Kumar, G., Bhadra, S.R., Mohtadi, M., Kurtarkar, S.R., Maurya, A.S., 2023. Large freshwater-influx-induced salinity gradient and diagenetic changes in the northern Indian Ocean dominate the stable oxygen isotopic variation in Globigerinoides ruber . Earth Syst. Sci. Data 15, 171–187. https://doi.org/10.5194/essd-15-171-2023

Schiebel, R., Hemleben, C., 2017. Planktic foraminifers in the modern ocean, Planktic Foraminifers in the Modern Ocean. https://doi.org/10.1007/978-3-662-50297-6

Schiebel, R., Zeltner, A., Treppke, U.F., Waniek, J.J., Bollmann, J., Rixen, T., Hemleben, C.,

2004. Distribution of diatoms, coccolithophores and planktic foraminifers along a trophic gradient during SW monsoon in the Arabian Sea. Mar. Micropaleontol. 51, 345–371. https://doi.org/10.1016/j.marmicro.2004.02.001

Schmitt, A., Elliot, M., Thirumalai, K., La, C., Bassinot, F., Petersen, J., Movellan, A., Jorry, S.J., Borgomano, J., 2019. Single foraminifera Mg/Ca analyses of past glacial-interglacial temperatures derived from G. ruber sensu stricto and sensu lato morphotypes. Chem. Geol. 511, 510–520. https://doi.org/10.1016/j.chemgeo.2018.11.007

Schmitz, K.S., 2018. Geoscience, in: Physical Chemistry. Elsevier, pp. 611–754. https://doi.org/10.1016/B978-0-12-800513-2.00003-6

Schott, F.A., Xie, S.P., McCreary, J.P., 2009. Indian ocean circulation and climate variability. Rev. Geophys. 47, 1–46. https://doi.org/10.1029/2007RG000245

Scott, E.M., Cook, G.T., Naysmith, P., 2010. The Fifth International Radiocarbon Intercomparison (VIRI): An Assessment of Laboratory Performance in Stage 3. Radiocarbon 52, 859–865. https://doi.org/10.1017/S003382220004594X

Seyfried, W.., Bischoff, J.., 1981. Experimental seawater-basalt interaction at 300°C, 500 bars, chemical exchange, secondary mineral formation and implications for the transport of heavy metals. Geochim. Cosmochim. Acta 45, 135–147. https://doi.org/10.1016/0016-7037(81)90157-5

Shackleton, N.J., 1974. Attainment of isotopic equilibrium between ocean water and the benthonic foraminifera genus Uvigerina: isotopic changes in the ocean during the last glacial.

Shackleton, N.J., Duplessy, J.-C., Arnold, M., Maurice, P., Hall, M.A., Cartlidge, J., 1988. Radiocarbon age of last glacial Pacific deep water. Nature 335, 708–711. https://doi.org/10.1038/335708a0

Shapiro, G.I., 2009. Black Sea Circulation, in: Encyclopedia of Ocean Sciences. Elsevier, pp. 401–414. https://doi.org/10.1016/B978-012374473-9.00600-7

Sikes, E.L., Samson, C.R., Guilderson, T.P., Howard, W.R., 2000. Old radiocarbon ages in the southwest Pacific Ocean during the last glacial period and deglaciation. Nature 405, 555–559. https://doi.org/10.1038/35014581

Skinner, L., McCave, I.N., Carter, L., Fallon, S., Scrivner, A.E., Primeau, F., 2015. Reduced

ventilation and enhanced magnitude of the deep Pacific carbon pool during the last glacial period. Earth Planet. Sci. Lett. 411, 45–52. https://doi.org/10.1016/J.EPSL.2014.11.024

Skinner, L.C., Fallon, S., Waelbroeck, C., Michel, E. and Barker, S., 2010. Ventilation of the deep Southern Ocean and deglacial CO_2 rise. Science, 328(5982), pp.1147-1151.

Skinner, L.C., Primeau, F., Freeman, E., De La Fuente, M., Goodwin, P.A., Gottschalk, J., Huang, E., McCave, I.N., Noble, T.L., Scrivner, A.E., 2017. Radiocarbon constraints on the glacial ocean circulation and its impact on atmospheric CO_2. Nat. Commun. 8, 1–10. https://doi.org/10.1038/ncomms16010

Southon, J., Kashgarian, M., Fontugne, M., Metivier, B., Yim, W.W.-S., 2002. Marine reservoir corrections for the Indian Ocean and Southeast Asia. Radiocarbon 167–180.

Spero, H.J. and Lea, D.W., 2002. The cause of carbon isotope minimum events on glacial terminations. Science, 296(5567), pp.522-525.

Spero, H.J., Mielke, K.M., Kalve, E.M., Lea, D.W., Pak, D.K., 2003. Multispecies approach to reconstructing eastern equatorial Pacific thermocline hydrography during the past 360 kyr. Paleoceanography 18. https://doi.org/10.1029/2002PA000814

Srivastava, R., Ramesh, R., Prakash, S., Anikumar, N., Sudhakar, M., 2007a. Oxygen isotope and salinity variations in the Indian sector of the Southern Ocean. Geophys. Res. Lett. 34. https://doi.org/10.1029/2007GL031790

Srivastava, R., Ramesh, R., Prakash, S., Anikumar, N., Sudhakar, M., 2007b. Oxygen isotope and salinity variations in the Indian sector of the Southern Ocean. Geophys. Res. Lett. 34. https://doi.org/10.1029/2007GL031790

Stainbank, S., Kroon, D., Rüggeberg, A., Raddatz, J., De Leau, E.S., Zhang, M., Spezzaferri, S., 2019. Controls on planktonic foraminifera apparent calcification depths for the northern equatorial Indian Ocean. PLoS One 14. https://doi.org/10.1371/journal.pone.0222299

Stephens, B.B., Keeling, R.F., 2000. The influence of antarctic sea ice on glacial-interglacial CO_2 variations. Nature 404, 171–174. https://doi.org/10.1038/35004556

Stott, L., Southon, J., Timmermann, A., Koutavas, A., 2009. Radiocarbon age anomaly at intermediate water depth in the Pacific Ocean during the last deglaciation. https://doi.org/10.1029/2008PA001690

Stott, L., Timmermann, A., 2011. Hypothesized Link Between Glacial/Interglacial Atmospheric CO_2 Cycles and Storage/Release of CO_2-Rich Fluids From Deep-Sea Sediments, in: Abrupt Climate Change: Mechanisms, Patterns, and Impacts. pp. 123–138. https://doi.org/10.1029/2010GM001052

Stott, L.D., Harazin, K.M., Quintana Krupinski, N.B., 2019. Hydrothermal carbon release to the ocean and atmosphere from the eastern equatorial Pacific during the last glacial termination. Environ. Res. Lett. 14. https://doi.org/10.1088/1748-9326/aafe28

Stuiver, M., Polach, H.A., 1977. Discussion Reporting of ^{14}C Data. Radiocarbon 19, 355–363. https://doi.org/10.1017/S0033822200003672

Stuiver, M., Reimer, P.J., Bard, E., Beck, J.W., Burr, G.S., Hughen, K.A., Kromer, B., McCormac, G., Van Der Plicht, J., Spurk, M., 1998a. INTCAL98 Radiocarbon Age Calibration, 24,000–0 cal BP. Radiocarbon 40, 1041–1083. https://doi.org/10.1017/S0033822200019123

Stuiver, M., Reimer, P.J., Braziunas, T.F., 1998b. High-Precision Radiocarbon Age Calibration for Terrestrial and Marine Samples. Radiocarbon 40, 1127–1151. https://doi.org/10.1017/S0033822200019172

Stuiver, M., Reimer, P.J., Reimer, R.W., 2021. CALIB 8.2 [WWW program].

Sverdrup, H.U., Johnson, M.W., Fleming, R.H., 1942. The Oceans, Their Physics, Chemistry, and General Biology. New York Prentice-Hall, c1942.

Tao, W., Huang, G., Hu, K., Qu, X., Wen, G., Gong, Y., 2014. Different influences of two types of El Niños on the Indian Ocean SST variations. Theor. Appl. Climatol. 117, 475–484. https://doi.org/10.1007/s00704-013-1022-x

Thandlam, V., T.V.S, U.B., Hasibur, R., Luca, P. De, Sahlée, E., Rutgersson, A., M, R., S.S.V.S, R., 2020a. A sea-level monopole in the equatorial Indian Ocean. npj Clim. Atmos. Sci. 3, 25. https://doi.org/10.1038/s41612-020-0127-z

Thandlam, V., Udaya, U.B., Hasibur, R., Luca, P. De, Sahlée, E., Rutgersson, A., M, R., S.S.V.S, R., 2020b. A sea-level monopole in the equatorial Indian Ocean. npj Clim. Atmos. Sci. 3, 1–12. https://doi.org/10.1038/s41612-020-0127-z

Thirumalai, K., Richey, J., 2016. Potential for paleosalinity reconstructions to provide information about AMOC variability. US Clivar Var. 14, 8–12.

Thornalley, D.J., Barker, S., Broecker, W.S., Elderfield, H. and McCave, I.N., 2011. The deglacial evolution of North Atlantic deep convection. science, 331(6014), pp.202-205.

Tiwari, M., Ramesh, R., Bhushan, R., Sheshshayee, M.S., Somayajulu, B.L.K., Jull, A.J.T., Burr, G.S., 2010. Did the Indo-Asian summer monsoon decrease during the Holocene following insolation? J. Quat. Sci. 25, 1179–1188. https://doi.org/10.1002/jqs.1398

Tiwari, M., Ramesh, R., Somayajulu, B.L.K., Jull, A.J.T., Burr, G.S., 2005. Early deglacial (~19-17 ka) strengthening of the northeast monsoon. Geophys. Res. Lett. 32, n/a-n/a. https://doi.org/10.1029/2005GL024070

Tomzak, M., Godfrey, J.S., 1994. Water mass formation, subduction, and the oceanic heat budget. Reg. Oceanogr. 0, 53–65. https://doi.org/10.1016/b978-0-08-041021-0.50009-6

Ummenhofer, C.C., Biastoch, A., Böning, C.W., 2017. Multidecadal indian ocean variability linked to the pacific and implications for preconditioning indian ocean dipole events. J. Clim. 30, 1739–1751. https://doi.org/10.1175/JCLI-D-16-0200.1

Valsangkar, A.B., Borole, D. V., Shejwalkar, A.S., Kalangutkar, N.G., Fernandes, N.O., Dias, C.C., 2009. Potential diagenetic and detrital sources for calcareous sediments from the Carlsberg Ridge, Indian Ocean. Curr. Sci. 96, 1090–1099.

Van Andel, T.H., 1975. Mesozoic/cenozoic calcite compensation depth and the global distribution of calcareous sediments. Earth Planet. Sci. Lett. 26, 187–194. https://doi.org/10.1016/0012-821X(75)90086-2

van Sebille, E., Sprintall, J., Schwarzkopf, F.U., Sen Gupta, A., Santoso, A., England, M.H., Biastoch, A., Böning, C.W., 2014. Pacific-to-Indian Ocean connectivity: Tasman leakage, Indonesian Throughflow, and the role of ENSO. J. Geophys. Res. Ocean. 119, 1365–1382. https://doi.org/10.1002/2013JC009525

Vecchi, G.A., Soden, B.J., 2007. Global Warming and the Weakening of the Tropical Circulation. J. Clim. 20, 4316–4340. https://doi.org/10.1175/JCLI4258.1

Vecchi, G.A., Soden, B.J., Wittenberg, A.T., Held, I.M., Leetmaa, A., Harrison, M.J., 2006. Weakening of tropical Pacific atmospheric circulation due to anthropogenic forcing. Nature 441, 73–76. https://doi.org/10.1038/nature04744

Visser, K., Thunell, R., Stott, L., 2003. Magnitude and timing of temperature change in the Indo-Pacific warm pool during deglaciation. Nature 421, 152–155.

https://doi.org/10.1038/nature01297

Wacker, L., Fülöp, R.-H., Hajdas, I., Molnár, M., Rethemeyer, J., 2013. A novel approach to process carbonate samples for radiocarbon measurements with helium carrier gas. Nucl. Instruments Methods Phys. Res. Sect. B Beam Interact. with Mater. Atoms 294, 214–217. https://doi.org/10.1016/j.nimb.2012.08.030

Wacker, L., Němec, M., Bourquin, J., 2010. A revolutionary graphitisation system: Fully automated, compact and simple. Nucl. Instruments Methods Phys. Res. Sect. B Beam Interact. with Mater. Atoms 268, 931–934. https://doi.org/10.1016/j.nimb.2009.10.067

Waelbroeck, C., Labeyrie, L., Michel, E., Duplessy, J.C., McManus, J.F., Lambeck, K., Balbon, E., Labracherie, M., 2002. Sea-level and deep water temperature changes derived from benthic foraminifera isotopic records. Quat. Sci. Rev. 21, 295–305. https://doi.org/10.1016/S0277-3791(01)00101-9

Wang, B., 2006. The asian monsoon. Springer Sci. Bus. Media.

Webster, P.J., Moore, A.M., Loschnigg, J.P., Leben, R.R., 1999. Coupled ocean–atmosphere dynamics in the Indian Ocean during 1997–98. Nature 401, 356–360. https://doi.org/10.1038/43848

Weiss, R.F., 1983. GEOSECS Indian Ocean Expedition: Hydrographic data 1977-1978.

Weldeab, S., Schneider, R.R., Kölling, M., 2006. Deglacial sea surface temperature and salinity increase in the western tropical Atlantic in synchrony with high latitude climate instabilities. Earth Planet. Sci. Lett. 241, 699–706. https://doi.org/10.1016/J.EPSL.2005.11.012

Winfree, A.T., Agladze, K. 1, Krinsky, V.I., Pertsov, A.M., Zykov, V., Muller, S.C., Markus, M., Kloss, G., Kusch, I., Horsthemke, W., Mccormick, . D, Swinney, H.L., Tam, W.Y., 1970. LETTERS TO NATURE Pathways of water between the Pacific and Indian oceans in the Indonesian seas, 15. Ouyang, Q. & Swinney, H. L. Chaos.

WOA18. World Ocean Atlas 2018. https://www.ncei.noaa.gov/access/world-ocean-atlas-2018/

Yadav, R., Naik, S.S., Narvekar, J., 2021. The equatorial Indian Ocean upper water-column structure influenced by cross-basinal water exchange over the last ~40000 years. Quat. Int. https://doi.org/10.1016/j.quaint.2021.04.002

Yang, J., Liu, Q., Xie, S.P., Liu, Z., Wu, L., 2007. Impact of the Indian Ocean SST basin mode on the Asian summer monsoon. Geophys. Res. Lett. 34, L02708. https://doi.org/10.1029/2006GL028571

You, Y., 1998. Intermediate water circulation and ventilation of the Indian Ocean derived from water-mass contributions. J. Mar. Res. 56, 1029–1067. https://doi.org/10.1357/002224098765173455

Yu, W., Xiang, B., Liu, L., Liu, N., 2005. Understanding the origins of interannual thermocline variations in the tropical Indian Ocean. https://doi.org/10.1029/2005GL024327

Yu, Z., Li, H., Li, M., Zhai, S., 2018. Hydrothermal signature in the axial-sediments from the Carlsberg Ridge in the northwest Indian Ocean. J. Mar. Syst.

Zhang, P., Zuraida, R., Rosenthal, Y., Holbourn, A., Kuhnt, W., Xu, J., 2019. Geochemical characteristics from tests of four modern planktonic foraminiferal species in the Indonesian Throughflow region and their implications. Geosci. Front. 10, 505–516. https://doi.org/10.1016/j.gsf.2018.01.011

Zheng, X.T., Xie, S.P., Vecchi, G.A., Liu, Q., Hafner, J., 2010. Indian ocean dipole response to global warming: Analysis of ocean-atmospheric feedbacks in a coupled model. J. Clim. 23, 1240–1253. https://doi.org/10.1175/2009JCLI3326.1

Ziegler, M., Diz, P., Hall, I.R., Zahn, R., 2013. Millennial-scale changes in atmospheric CO_2 levels linked to the Southern Ocean carbon isotope gradient and dust flux. https://doi.org/10.1038/NGEO1782

List of Publications

I. Included in Thesis

1. **Jena, S.K.**, Bhushan, R., Bharti, N., Jena, P.S., Dhabi, A.J., Shivam, A., 2023. Anomalous Seawater Radiocarbon Depletion in the Equatorial Indian Ocean Thermocline during the MIS3-MIS2 Transition. Palaeogeogr. Palaeoclimatol. Palaeoecol. (Under Review – 2nd submission).

2. **Jena, S.K.,** Bhushan, R., Jena, P.S., Bharti, N., Sudheer, A.K., Sanyal, P., A.J., Shivam, A., Dhabi, A.J., 2024. The Indian Monsoon and North Atlantic Tele-climatic Controls upon the Arabian Sea High Salinity Water Variability into the Equatorial Indian Ocean during the Last Glacial-Interglacial Period. Paleoceanography and Paleoclimatology. (Submitted).

3. **Jena, S.K.**, Bhushan, R., Bharti, N., Jena, P.S., Shivam, A., Dhabi, A.J.. Quantitative Reconstruction of Equatorial Indian Ocean Paleothermocline with Evidence of High-Latitude Climatic Controls. (Under preparation).

II. Other Publications

1. Jena, P.S., Bhushan, R., **Jena, S.K.**, Ajay, S., Sudheer, A.K., 2024. Spatial Variability in Residence Time of Beryllium in the Indian Ocean. Applied Geochemistry. (submitted).